Department of Applied Physics

Improved Spatial Resolution of Bushfire Detection with MODIS

Florian Goessmann

This thesis is presented for the Degree of
Master of Science
of
Curtin University of Technology

February 2007

Declaration

This thesis contains no material which has been accepted for the award of any other degree or diploma in any university.

To the best of my knowledge and belief this thesis contains no material previously published by any other person except where due acknowledgment has been made.

Signature: .....

Date: .....

Contents

List of Figures

List of Tables

Abstract

The capability to monitor bushfires on a large scale from space has long been identified as an important contribution to climate and atmospheric research as well as a tool an aid in natural hazard response. Since the work by Dozier (1981), fire monitoring from space has relied on the principles he described. His method of identifying fires within a pixel significantly larger than the fire by utilizing the different responses of the 3 μm and 11 μm channels has been applied to a number of sensors. Over the last decade a lot of work has been invested to refine and validate fire detections based on this approach. So far, the application of the method proposed by Dozier (1981) reached its peak with the launch of the MODIS instrument on board the Terra satellite. In contrast to earlier sensors, MODIS was equipped with spectral channels specifically designed for the detection of fires with algorithms based on the work by Dozier (1981). These channels were designed to overcome problems experienced with other platforms, the biggest of which is the saturation of the 3 μm channel caused by big, hot fires. Since its launch, MODIS has proven itself to be a capable platform to provide worldwide fire detection at a moderate resolution of 1 km on a daily basis.

It is the intention of this work to open up new opportunities in remote sensing of fires from satellites by showing capabilities and limitations in the application of other spectral channels, in particular the 2.1 μm channel of MODIS, than the ones currently used. This channel is chosen for investigation as fires are expected to emit a significant amount of energy in this bandwidth and as it is available at a native resolution of 500 m on MODIS; double the resolution of the 3 μm and 11 μm channels.

The modelling of blackbodies of typical bushfire temperatures shows that a fire detection method based on the 2.1 μm channel will not be able to replace the current methods. Blackbodies of temperatures around 600 to 700 K, that are common for smoldering fires, do not emit a great amount of energy at 2.1 μm. It would be hardly possible to detect those fires by utilizing the 2.1 μm channel. The established methods based on the 3 μm and 11 μm channels are expected to work better in these cases. Blackbodies of typically flaming fires (above 800 K) however show a very high

emission around 2.1 μm that should make their detection using the 2.1 μm channel possible.

In order to develop a fire detection method based on the 2.1 μm channel, it is necessary to differentiate between the radiance caused by a fire of sub pixel size and the radiance of a pixel caused by the reflection of sunlight. This is attempted by using time series of past observations to model a reflectance value for a given pixel expected in absence of a fire. A fire detection algorithm exploiting the difference between the expected and observed reflectance is implemented and its detection results are compared to high resolution ASTER fire maps, the standard MODIS fire detection algorithm (MOD14) and burnt area maps. The detections of the method based on the 2.1 μm channel are found to correspond very well with the other three datasets. However, the comparison showed detections that do not align with MOD14 active fire detections but are generally alinged with burn areas. This phenomena has to be investigated in the future.

Chapter 1

Introduction

Burning biomass plays an important environmental role over large areas of the Earth. Tansey et al. (2004) concluded from data collected by the Global Burnt Area 2000 project (Gregoire et al., 2003), that in the year 2000 3.5 million km^2 of the Earth's surface was affected by vegetation fires. These fires can have a strong influence on ecosystem's productivity (Potter et al., 2003) and can drastically change the vegetation pattern of large areas within a short period of time (Bachelet et al., 2001). This is especially the case in savannas, boreal forests, tundra and tropical and subtropical ecosystems (Kaufman et al., 1998; Justice et al., 2002) in which fires regularly occur.

Furthermore, vegetation fires are a major source of aerosols and trace gases (Langenfelds et al., 2002) and are, in combination with industrial activities, believed to be the largest uncertainty in identifying a potential climate change caused by human impact (Houghton et al., 1995). The aerosols and gases released by fires affect atmospheric chemistry, cloud properties and radiation budget (Crutzen and Andreae, 1990; Kaufman and Fraser, 1997; Langenfelds et al., 2002).

In addition to the effects of fires on the climate, atmosphere and biomes,

fires are also a major natural hazard. With the spread of urban areas in former wildland areas, the threat from bushfires to damage or destroy important infrastructure increases.

In order to investigate the above mentioned effects of fires on the climate and atmosphere on a global or regional scale and to provide disaster management authorities with helpful information, it is important to develop capabilities to monitor the location and extent of active fires. Satellite remote sensing can provide this information on a range of spatial, temporal and spectral scales (Justice et al., 1993).

1.1 Fire Detection from Satellites

The first numerical modlling to identify sub-pixel fields of high temperature was introduced by Dozier (1981) for the Advanced Very High Resolution Radiometer (AVHRR). He divided a hypothetical pixel into two temperature fields: a background temperature and a target temperature that occupied some fraction of the pixel. He showed that it was possible to detect pixels that contain a small, but hot target due to the different responses of the 3.7 μm and 11 μm channels of AVHRR. Based on this model, Dozier (1981) introduced a set of simultaneous, non-linear equations that could be solved for the temperature and pixel fraction of the hot target. Dozier's model will be discussed in more detail in chapter 3.

The first demonstration of this concept with real data was given by Matson and Dozier (1981). They were able to manually detect very hot industrial sources in Detroit and waste gas flares in the Persian Gulf using nighttime data from AVHRR-6. In a similar fashion, but using AVHRR daytime instead of nighttime data, Muirhead and Cracknell (1984) were able to detect gas flares of oil rigs in the North Sea. Muirhead and Cracknell (1984) were among the first to detect vegetation fires. They applied their technique to daytime data of AVHRR to detect straw burnings in

Great Britain. Matson et al. (1984) were able to detect fires in Brazil and the USA with daytime data of AVHRR. The fires they detected in the USA were mostly verified by ground based observations.

These first efforts showed that it was possible to identify pixels that contain a small hot target. They however relied on manual inspection and were therefore not well suited for fire detection on a large scale. The first automated approach to detect fires with AVHRR data was published by Flannigan (1985) and later again Flannigan and Von der Haar (1986). By inspecting a subset of the data and then applying the results of manual inspection to the full dataset in an automated way, they were able to monitor a severe forest fire outbreak in Alberta, Canada. As they had access to daily information on fire size and location gathered by the Alberta Forest Service, they were able to verify their detections. They found that they were able to detect 80% of the fires that were not covered by smoke or cloud. The fire sizes they estimated from the AVHRR data using the method proposed by Dozier (1981) were 70% too large for small fires and 50% too small for large fires.

Following these initial works, several case studies (Matson and Robinson, 1987; Matson and Holben, 1987; Langaas and Muirhead, 1989; Stephens and Matson, 1989) were published. These studies did not concentrate on the actual detection of fires, but more on the limitations of active fire detection with AVHRR. Some of which are obstruction of the fire by smoke plumes (Matson and Holben, 1987; Matson and Robinson, 1987), the problems associated with surface reflectance and emissivity and extension of the two-temperature field model developed by Dozier (1981) to include warm, recently burnt areas (Langaas and Muirhead, 1989).

A different approach to automated fire detection with AVHRR was proposed by Lee and Tag (1990) after analyzing data from the Persian Gulf and the San Francisco area. In contrast to the Dozier approach which tries to identify the fire temperature from observation, Lee and Tag (1990) intuitively choose a temperature that a fire should have. They then used

the Dozier model to create a lookup table consisting of satellite measurements that represent valid fire detections.

The first application of an AVHRR fire detection scheme to an operational fire detection system on a regional scale was undertaken by Setzer and Pereira (1991). They monitored the fire seasons in Brazil since 1989. For the fire season of 1989, 96% of the fires they detected were verified by ground crews. The fire detection technique used by Setzer and Pereira (1991) was based on (i) a fixed temperature threshold in the 3.7 μm channel to identify pixels that possibly contain an active fire and (ii) visual inspection of the 0.64 μm channel to detect corresponding smoke plumes. If a potential fire pixel did not correspond with a smoke plume, it was rejected. Pereira et al. (1991) used data from Landsat/Thematic Mapper (TM) to validate fire detections and burnt area estimates from AVHRR data over a period of five consecutive days. Every positive AVHRR fire detection corresponded with a burn scar detected with the TM data.

Giglio et al. (1999) undertook a major theoretical comparison of three fire detection algorithms (Arino et al., 1993; Flasse and Ceccato, 1996; Justice et al., 1996) that attempt to provide fire detection capabilities on a global scale. In order to compare the detection performance, Giglio et al. (1999) developed a sophisticated model to simulate AVHRR data for a wide range of biomes and viewing conditions that contained fires of varying temperatures and size. They found that in general, the lower limit for fire detection with AVHRR are smoldering fires (600 K) of 1000 m^2 or flaming fires (900 K) of 100 m^2. They also found, that AVHRR fire detection has an upper limit for temperature and size. According to Giglio et al. (1999) fire detection with AVHRR is problematic for hot fires bigger than 10,000 m^2 due to sensor saturation. They further conclude that simple, fixed threshold algorithms are not well suited for global fire detection as they require fine tuning for different regions. They further proposed an enhanced version of the algorithm developed by Justice et al. (1996).

The algorithm proposed by Giglio et al. (1999) was part of an assess-

ment of five fire detection algorithms (Malingreau, J.P. and Justice, C.O., (editors), 1997; Kaufman and Justice, 1998; Giglio et al., 1999; Arino and Rosaz, 1999; Li et al., 2000b) by Li et al. (2000a) using AVHRR data from the Canadian fire season of 2000. They concluded that the performance of the five tested algorithms differs drastically and that the potential capabilities of current satellite sensors for monitoring fires are not yet fully exhausted. They also provided recommendations for future fire detection techniques such as the use of multiple sensors, time series and algorithms tailored to specific environments or specific user groups.

Although AVHRR has been and is one of the most commonly used sensors for monitoring of fires, techniques similar to those developed for AVHRR have been applied to other platforms. The Visible Spin Scan Radiometer and Atmospheric Sounder (VAS) on board the goestationary, meteorological satellite GOES, has shown potential to detect burning biomass in North and South America (Kaufman and Justice, 1998). Compared to AVHRR, VAS has the advantage of providing coverage of the Americas at least every three hours but this comes at the price of an spatial resolution lower than the one provided by AVHRR (Kaufman et al., 1998). Based on the Dozier (1981) model, Prins and Menzel (1992) developed an algorithm for VAS to detect fires as well as to estimate the fire's size and average temperature.

The possible application to fires of the Visible and Infrared Scanner (VIRS) instrument on board the Tropical Rainfall Measuring Mission (TRMM) satellite to detect vegetation fires was first proposed by Giglio et al. (2000). They pointed out that VIRS has channels very similar to those of AVHRR and thus it should be possible to utilize VIRS data to detect fires using algorithms based on the Dozier (1981) model. Ji and Stocker (2002) describe such an algorithm for VIRS. They compared the detection results of VIRS with those of AVHRR and were able to find the same spatial distribution patterns in both fire detection datasets. Giglio et al. (2003b) provided a performance overview of fire detection with VIRS from January 1998 to January 2002. They used two methods to examine the algorithm

performance: (i) running the algorithm on simulated data based on the model by Giglio et al. (1999) and, (ii) manually identifying fire pixels and comparing those to fire pixels detected by the algorithm. From the simulation, they concluded that the smallest, actively burning fire of temperatures about 1000 K with a reasonable detection probability is between 100 and 200 m^2. Purely smoldering fires at about 600 K would be required to have ten times that size in order to have the same detection probability. Their manual inspection showed that grassland fires are more likely to be detected than fires in wood and forest ecosystems.

Following the Kyoto conference on climate change, the European Space Agency (ESA) started the World Fire Atlas (WFA) showing active fires detected with the Along Track Scanning Radiometer onboard the Second European Remote Sensing Satellite (ERS-2). Fire detection is based on a single channel algorithm and only nighttime data are utilized (Mota et al., 2005). Although designed to observe vegetation fires, Mota et al. (2005) found that about one quarter of the detections are due to hot surfaces, volcanoes, gas flares and image acquisition/processing problems.

Although the scientific community identified global fire detection from remote sensing platforms as an important tool for several research areas, a satellite based sensor that was designed with fire detection in mind did not exist until the launch of the Moderate Resolution Imaging Spectroradiometer (MODIS) on board the Terra satellite in 1999 (Justice et al., 2002). MODIS has spectral channels located in the middle infrared (MIR) that are designed not to saturate, even if a pixels contains a large, hot fire (Kaufman et al., 1998). The first MODIS fire detection algorithms have been based on the experience gained with the fire detection products of AVHRR and TRMM VIRS (Kaufman and Justice, 1998; Justice et al., 2002). Justice et al. (2002) undertook some initial validation studies for MODIS fire detection capabilities by comparing it with high resolution fire detections of the Advanced Thermal Emission and Reflection Radiometer (ASTER) (Yamaguchi et al., 1998). They found that the MODIS fire detection generally worked as expected but did not judge its general perfor-

mance as they only used four ASTER scenes falling within two MODIS granules.

Giglio et al. (2003a) proposed an improved contextual fire detection algorithm for MODIS. It was based on the algorithm by Justice et al. (2002), but incorporated enhancements to overcome the problems that have shown earlier. These problems were false detections in desert and other sparsely vegetated regions and frequent non-detections of small but obvious fires. Based on the method developed by Giglio et al. (1999), Giglio et al. (2003a) tested the performance of their proposed algorithm with simulated MODIS data. They found that their algorithm had, under ideal conditions, a 50% chance to detect fires of about 100 m^2. This was less than half the fire size required by the Justice et al. (2002) algorithm to achieve the same detection probability (Giglio et al., 2003a). Morisette et al. (2005) compared both the algorithms described by Justice et al. (2002) and Giglio et al. (2003a) with fire maps derived from 18 ASTER scenes over southern Africa. They found that the minimum fire size required by the Giglio et al. (2003a) algorithm to achieve 50% detection probability was 30 ASTER pixels (an area of 27,000 m^2, 30 m pixel size). The Justice et al. (2002) algorithm required a fire size of 48 ASTER pixels (43,100 m^2) to accomplish the same detection performance.

1.2 Possible Improvements

Detection and monitoring of bushfires from space has been and probably will always be a trade off between temporal and spatial resolution. Goestationary satellites such as GOES are able to provide a high temporal spatial resolution (every 30 minutes or less) but that comes at the price of a large pixel footprint (4 km or above) and a limited observation region (in case of GOES North and South America). Sensors with a high spatial resolution like ASTER can provide detailed information on the spatial extent of fires but are ineffective for remote sensing of bush-

fires for anything else but case studies as their temporal resolution (scene revisit frequency) is days or even weeks.

In order to study fires effectively from space, given their relatively short life span and rapid temporal and spatial variability, a suitable observation platform has to provide at least daily coverage at the highest spatial resolution possible. Today, the best compromise seems to be provided by the AVHRR and MODIS sensors that have thermal channels at moderate resolution of about 1 km and provide a reasonable temporal resolution as they both are carried onboard more than one satellite.

Although a lot of studies have dealt with fire detection based on these two sensors, as pointed out by Li et al. (2000b), there is still room for improvement. One possibility to improve MODIS-based fire detection will be presented in this work. It is the aim to provide the possibility of a higher spatial resolution of the fire detection with MODIS without compromising temporal resolution and coverage. This is intended to be achieved by utilizing spectral channels of MODIS that have a higher spatial resolution than the thermal channels used by algorithms based on the work by Dozier (1981) and are currently not being used for the detection of active fires. Due to the physics of this new approach, it is intended to be an addition, not a replacement, to current fire detection techniques. It is planned that the product that is to be developed will provide more insight on the spatial distribution of the flaming areas within a fire than is currently possible.

Chapter 2

Principles of Satellite Measured Radiances

In order to understand how active bushfires can be detected from space borne sensors, it is important to understand some basic principles. These include how objects emit and reflect radiation and what influences the atmosphere can have on the radiation as it travels through it to the on-orbit sensors. This chapter will briefly cover these basics.

2.1 Blackbody Radiation

All matter at temperatures above absolute zero (0 K or -273 °C) (Lillesand et al., 2004) emits electromagnetic energy at all times. In case of a hypothetical, ideal energy source that absorbs and reemits all incident energy, a so called blackbody (Lillesand et al., 2004), the properties of the emitted energy can be described by several physical laws. The total amount of energy emitted by a blackbody of a given temperature is expressed by the Stefan-Boltzmann-Law which proclaims that

$$M = \sigma T^4, \tag{2.1}$$

with

M = total emitted energy in watt (W m^{-2})
σ = Stefan-Boltzmann constant, 5.667×10^{-8} W m^{-2} K^{-4}
T = absolute temperature (K) of emitting material.

It is important to note that M is dependent on T^4 and therefore rapidly increases with rising temperatures. Furthermore, as M is the total emitted energy, it covers the whole electromagnetic spectrum and does not include information on any particular wavelength a given material emits. The wavelength at which the radiation of an object of a given temperature reaches its maximum is described by Wien's Displacement Law

$$\lambda_{max} = \frac{2.898 \times 10^{-3} K \cdot m}{T}, \tag{2.2}$$

where

λ_{max} = wavelength of maximum radiation, m
T = temperature, K.

2.1.1 The Different Regions of the Electromagnetic Spectrum

Blackbodies emit radiation not only at a discrete wavelength but over a whole spectrum. Different regions of this spectrum have common names assigned to them, some of which will be used in this thesis.

The visible region of the electromagnetic spectrum, the region which the human eye is sensitive to, ranges from 0.4 μm to 0.7 μm (Lillesand et al.,

2004). The visible range is divided into three sub-spectral regions associated with the colors blue, green and red. The blue spectrum ranges from 0.4 μm to 0.5 μm, the green one from 0.5 μm to μm 0.6 μm and the red one from 0.6 μm to 0.7 μm (Lillesand et al., 2004). Adjacent to the red end of the visible region is the infrared (IR) spectrum ranging from 0.7 μm to 14 μm, on its blue end, it is adjoined by the ultraviolet spectrum (UV) (Lillesand et al., 2004). The IR spectrum is made up from three sub-spectral regions to which this work frequently refers. These are the near infrared (NIR) covering the wavelengths from 0.7 μm to 1.3 μm, the middle infrared (MIR) ranging from 1.3 μm to 3μm and the thermal infrared (TIR) from 3 μm to 14 μm (Lillesand et al., 2004).

2.1.2 Emissivity

As stated above, a blackbody is a hypothetical. That means, real materials only emit a fraction of the energy that a blackbody of the same temperature would emit. This fraction, that describes the emitting ability of an object, is called the object's emissivity ε (Lillesand et al., 2004). ε is a spectrally dependent quantity, denoted as $\varepsilon(\lambda)$ and is defined as

$$\varepsilon(\lambda) = \frac{\text{radiant exitance of an object at a given temperature}}{\text{radiant exitance of a blackbody at the same temperature}}, \quad (2.3)$$

and can have values between 0 and 1 (an emissivity of one would be a 'true' blackbody). The emissivity of an object can vary with wavelength, viewing angle and depending on the material to a certain extent temperature (Lillesand et al., 2004). An object whose emissivity does not vary with wavelength is called a graybody whereas an object whose emissivity does vary with wavelength is called a selective reflector (Lillesand et al., 2004). Salisbury and D'Aria (1992) and Salisbury and D'Aria (1994) have published the emissivities of a wide range of different materials.

Emissivity can be used to extend the Stefan-Boltzmann law (equation 2.1) to better match real materials by reducing the total emitted energy M by the emissivity factor ε (Lillesand et al., 2004) which transforms equation 2.1 to

$$M = \varepsilon \sigma T^4. \tag{2.4}$$

2.1.3 Reflectance

When electromagnetic energy interacts with a given object, it can do so in three different ways (Lillesand et al., 2004). Fractions of the energy can be reflected, absorbed or transmitted. As the principle of conservation of energy applies, the relation between the three interactions can be described as

$$E_I(\lambda) = E_R(\lambda) + E_A(\lambda) + E_T(\lambda) \tag{2.5}$$

where

$$\begin{aligned} E_I(\lambda) &= \text{incident energy} \\ E_R(\lambda) &= \text{reflected energy} \\ E_A(\lambda) &= \text{absorbed energy} \\ E_T(\lambda) &= \text{transmitted energy} \end{aligned}$$

All energy components are dependend on wavelength which means that the same object might have very different proportions of the three energies at different wavelengths (Lillesand et al., 2004).

Apart from the reflected energy, the geometric manner in which an object reflects energy is important in order to characterize an object's reflectance properties. This manner is mostly dependent on the objects

surface roughness (Lillesand et al., 2004). The two extremes of reflectors are specular and diffuse (or Lambertian) reflectors. Specular reflectors are flat surfaces that produce mirror-like reflections with equal angles of reflection and incidence. Lambertian reflectors are rough surfaces that reflect incoming energy equally to all directions (Lillesand et al., 2004). Most surfaces are neither of the two but show characteristics that are somewhat in between. Specular reflection, however, does occur frequently and can, depending on the angular Sun-object-sensor relationship, be the cause of sunglint. Areas of sunglint show a very high increase in reflection compared to their surroundings and have only very little information on the true nature of the involved objects (Lillesand et al., 2004). The way the same object reflects energy is not uniform over the electromagnetic spectrum but depends on the wavelength of incident energy. That means that an object's roughness is defined by the proportion of wavelength of the electromagnetic energy incident upon the object and the height variations of the object's surface (Lillesand et al., 2004). The reflectance of an object defined as

$$\rho(\lambda) = \frac{E_R(\lambda)}{E_I(\lambda)} \tag{2.6}$$

and is called the spectral reflectance (Lillesand et al., 2004). It is sometimes multiplied by 100 and expressed as a percentage value.

2.1.4 The Relation of Emissivity and Reflectance

If equation 2.5 is divided by the quantity of E_I,

$$\frac{E_I(\lambda)}{E_I(\lambda)} = \frac{E_R(\lambda)}{E_I(\lambda)} + \frac{E_A(\lambda)}{E_I(\lambda)} + \frac{E_T(\lambda)}{E_I(\lambda)} \tag{2.7}$$

is obtained. The ratios on the right side of this equation can be used to

describe the characteristics of energy interactions (Lillesand et al., 2004) and are defined as

$$\alpha(\lambda) = \frac{E_A(\lambda)}{E_I(\lambda)} \tag{2.8}$$

$$\rho(\lambda) = \frac{E_R(\lambda)}{E_I(\lambda)} \tag{2.9}$$

$$\tau(\lambda) = \frac{E_T(\lambda)}{E_I(\lambda)} \tag{2.10}$$

where

$$\begin{aligned} \alpha(\lambda) &= \text{absorptance of the object} \\ \rho(\lambda) &= \text{reflectance of the object} \\ \tau(\lambda) &= \text{transmittance of the object.} \end{aligned}$$

These ratios allow equation 2.5 to be expressed in the form

$$\alpha(\lambda) + \rho(\lambda) + \tau(\lambda) = 1. \tag{2.11}$$

Kirhchoff's radiation law

$$\varepsilon(\lambda) = \alpha(\lambda) \tag{2.12}$$

states that the spectral emissivity of an objects equals its spectral absorptance(Lillesand et al., 2004)

According to Lillesand et al. (2004) the relationship in 2.12 holds true for most remote sensing conditions although it is based on conditions of thermal equilibrium. If equation 2.12 is applied to equation 2.11 it results in

$$\varepsilon(\lambda) + \rho(\lambda) + \tau(\lambda) = 1. \tag{2.13}$$

Further simplification is possible for wavelengths in the TIR as most objects that are dealt with in remote sensing are opaque to thermal radiation Lillesand et al. (2004). That means that $\tau(\lambda) = 0$ and is dropped from equation 2.13 which then is

$$\varepsilon(\lambda) + \rho(\lambda) = 1. \tag{2.14}$$

This equation (2.14) describes the direct relation of emissivity and reflectance in the TIR. It shows that the higher an objects emissivity, the lower its reflectance. Hence, a blackbody has a reflectance of 0.

2.1.5 Equivalent Blackbody Temperature

In TIR and MIR remote sensing, it is very common to express radiation as equivalent blackbody temperatures (BBT) (Giglio et al., 2003a; Justice et al., 2002; Kaufman and Justice, 1998; Li et al., 2000a; Maier, 2002; Flasse and Ceccato, 1996; Giglio et al., 1999). Equation 2.4 clearly shows that it is possible to determine an object's surface temperature by measuring its radiation if its emissivity is known. As this is usually not the case, the observed object is assumed to be a blackbody (ε = 1) and its radiation converted into the corresponding temperature. The equivalent blackbody temperature of an object, hence, is the temperature of a blackbody that shows the same radiation properties as the observed object.

2.2 Atmospheric Influence in the Visible and Infrared Range

All radiation detected by a remote sensor has to travel through some distance or path in the atmosphere. In the case of satellite based sensors, radiation emitted has to pass once through the whole thickness of the earth's atmosphere. Radiation that is caused by reflected sun light has to pass through the atmosphere twice before it reaches the sensor. How strong the net effect of the atmosphere is, depends on the length of the path, the magnitude of the sensed signal, the atmospheric conditions and the observed wavelength (Lillesand et al., 2004).

Atmospheric influence to remotely sensed radiation is mainly caused by scattering and absorption (Lillesand et al., 2004; Rees, 2001). Scattering and absorption is the result of the interaction of electromagnetic radiation with atmospheric molecules and particles of different sizes (Lillesand et al., 2004; Rees, 2001).

2.2.1 Scattering

According to Lillesand et al. (2004), scattering is the unforeseeable diffusion of radiation in the atmosphere. Scattering of radiation on particles much smaller than the wavelength of the radiation is called Rayleigh scatter (Lillesand et al., 2004; Rees, 2001). Rayleigh scatter by individual molecules can be crudely described as

$$\sigma_S = \frac{128\pi^5 a^6}{3\lambda^4} \tag{2.15}$$

where

a = diameter of molecule
λ = wavelength of radiation.

As Rayleigh scattering depends on λ^{-4}, it rapidly decreases with increasing λ (Lillesand et al., 2004; Rees, 2001). The significance of Rayleigh scattering is most pronounced in the ultraviolet region (the region of shorter wavelength than visible light) of the electromagnetic spectrum (Lillesand et al., 2004; Rees, 2001) but its effect is still noticeable in the visible region of the spectrum. In fact, Rayleigh scatter is the reason for the sky being blue. As blue is the shortest of the visible wavelength, it is much more affected by Rayleigh scattering than the longer visible wavelengths due to the Rayleigh scatter's λ^{-4} dependence (Lillesand et al., 2004; Rees, 2001). It also is the reason for the red skies at sunrise and sunset. At these times, the sun's radiation has to travel a much longer distance through the atmosphere than at midday. This longer path causes most of the blue part of the electromagnetic spectrum to be scattered away from the forward direction and only the longer, less scattered parts of the spectrum that correspond to orange and red reach the observer on the earth's surface (Lillesand et al., 2004; Rees, 2001). The strong Rayleigh scattering of the ultraviolet and blue spectra is the reason why these regions are usually less important in remote sensing (especially in satellite remote sensing, due to the long path distances) than the less scattered, longer wavelengths (Rees, 2001).

The relation of the intensity of scattered radiation and the scattering angle (angle between the direction of the incoming radiation and the scattered radiation) is described by the phase function. The phase function for Rayleigh scattering is defined as (American Meteorological Society, 2000):

$$p(\theta) = \frac{3}{4}(1 + cos^2\theta) \tag{2.16}$$

where

θ = scattering angle.

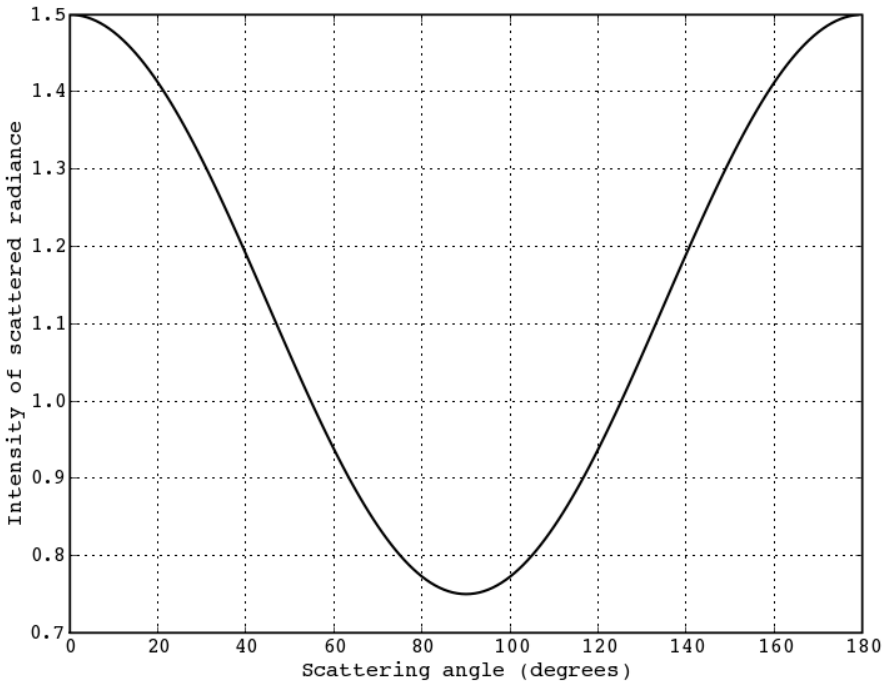

Figure 2.1: Phase function of Rayleigh scattering (equation 2.16, p 17) for scattering angles from 0° to 180°

Figure 2.1 (p 18) shows that Rayleigh scattering is a maximum in the forward and backward directions.

Apart from scattering off molecules, scattering also happens on larger particles. Aerosols are small solid particles or liquid droplets suspended in the atmosphere with radii typically ranging from 10 nm to 10 μm (Rees, 2001). Most aerosols originate from the Earth's surface and thus their type and size distribution is strongly dependent on local meteorological and geographical conditions (Rees, 2001). The attenuation coefficient describes the fractional depletion of radiation per unit path length (American Meteorological Society, 2000) as defined by Bouguer's law as:

$$\frac{dL}{L} = -\gamma \, ds \tag{2.17}$$

where

L = monochromatic radiance at a given wavelength
γ = attenuation coefficient
ds = differential increment of path length.

The predominant contributor to the attenuation coefficient at visible and infrared wavelength is scattering (Rees, 2001). Its dependence on wavelength is approximately described by the Ångström relation (Rees, 2001):

$$\gamma = \gamma_0 \lambda^{-n} \tag{2.18}$$

where

γ_0 = a constant
λ = wavelength
n = Ångström exponent.

From the formula describing Rayleigh scattering (equation 2.15, p 16), n is equalto 4 in case of particles much smaller than the wavelength. For most aerosols, n is between 0.2 and 2 (Rees, 2001).

Scattering can further be caused by atmospheric water vapour forming fog, low altitude (up to about 3000 m) clouds and the ice crystals contained in clouds of higher altitudes (Rees, 2001). These water droplets are bigger than those of aerosols. They range from about 10 μm to 100 μm (Lillesand et al., 2004; Rees, 2001) and as with aerosols, the main contributor to their attenuation coefficient at visible and infrared wavelength is scattering (Rees, 2001). All visible to MIR wavelength are scattered about

equally by these droplets, thus clouds and fog appear white as equal quantities of radiation of blue, green and red wavelength are scattered (Lillesand et al., 2004).

2.2.2 Absorption

Atmospheric absorption, in contrast to scattering, results in loss of radiation to atmospheric elements (Lillesand et al., 2004). In the visible and infrared range, molecules are the predominant cause of absorption (Lillesand et al., 2004; Rees, 2001). The energy of the radiation lost to absorption is used by the molecules interacting with the radiation to either change their energy level, vibrate, rotate or a combination of those three (Rees, 2001). The most important absorbers are water vapor (H_2O), carbon dioxide (CO_2), ozone (O_3), oxygen (O_2), nitrous oxide (N_2O) and methane (CH_4) (Lillesand et al., 2004; Rees, 2001).

As these gases absorb electromagnetic energy at specific wavelength regions, the so called absorption lines, they play an important role in the decision on which spectral bands are best to be observed by a remote sensor (Lillesand et al., 2004). Table 2.1 (p 21) shows the absorption lines of the most important absorbing gases. The spectral regions, where none of the gases has a high absorption and the atmosphere is particularly transmissive for electromagnetic energy are called atmospheric windows (Lillesand et al., 2004; Rees, 2001). These atmospheric windows are the wavelength ranges at which remote sensors commonly operate.

Figure 2.2 (p 22) shows the atmospheric transmission for the US 1976 Standard Atmosphere (U.S. Government, 1976). The atmospheric windows are indicated by the the grey area. The atmospheric windows commonly used in remote sensing are the windows from 0.3 μm to 2.3 μm for observations in the visible range and the NIR, the window between 3 μm and 5 μm for observations in the MIR and the window from 8 μm and 14 μm for observations in the TIR (Lillesand et al., 2004).

Table 2.1: Absorption lines in the Earth's atmosphere of the most important absorbing molecules in the visible and infrared regions. Source: Rees (2001)

Wavelength (μm)	**Molecule**	**Wavelength (μm)**	**Molecule**
0.26	O_3	3.9	N_2O
0.60	O_3	4.3	CO_2
0.69	O_2	4.5	N_2O
0.72	H_2O	4.8	O_3
0.76	O_2	4.9	CO_2
0.82	H_2O	6.0	H_2O
0.93	H_2O	6.6	H_2O
1.12	H_2O	7.7	N_2O
1.25	O_2	7.7	CH_4
1.37	H_2O	9.4	CO_2
1.85	H_2O	9.6	O_3
1.95	CO_2	10.4	CO_2
2.00	CO_2	13.7	O_3
2.10	CO_2	14.3	O_3
2.60	H_2O	15	CO_2
2.70	CO_2		

It is interesting to note that according the Wien's Displacement law (equation 2.2, p 10), the maximum radiation of the sun as well as the sensitivity of the human eye fall within the atmospheric window from 0.3 μm and 0.7 μm and the maximum radiation emitted by the Earth, the second commonly used natural source of radiation, falls within the atmospheric window ranging from 8 μm and 14 μm.

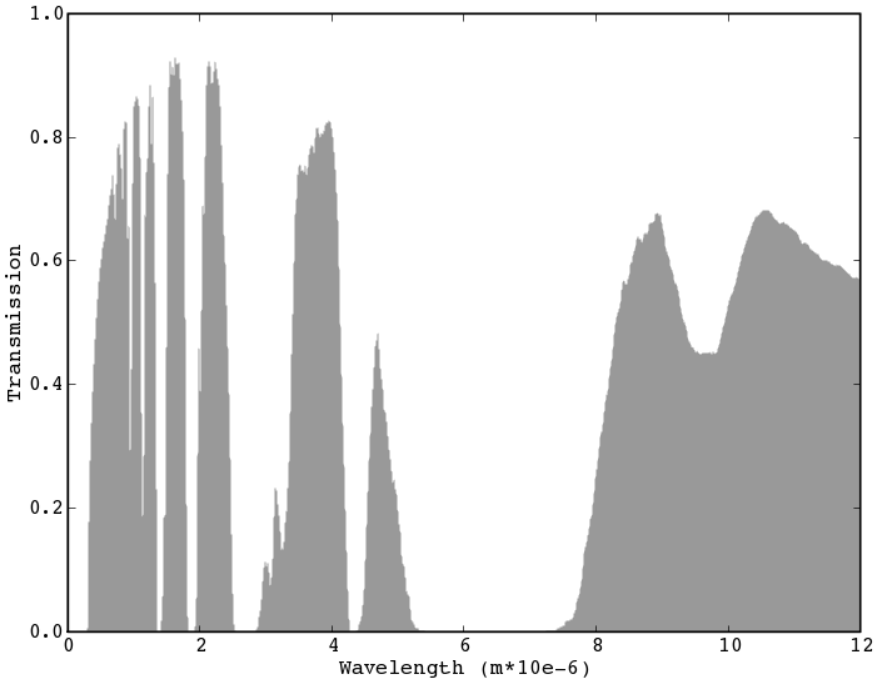

Figure 2.2: Transmission of the Earth's atmosphere. Values calculated by MODTRAN for the US 1976 Standard Atmosphere (U.S. Government, 1976).

Chapter 3

Remote Sensing of Bushfires

Chapter one gave a non-technical overview of remote sensing of active bushfires and chapter two briefly explained physical principles required to understand how fire detection from satellites is possible. This chapter will bring these two aspects together. It will begin by giving a more detailed overview of the MODIS instrument, followed by a description of the spectral properties of blackbodies of temperatures expected from active bushfires. The next part is made up of an account of the fundamental work by Dozier (1981), which is more technical and detailed than the brief description given in chapter one. Finally, a brief technical description of some of the sensors mentioned in chapter one (MODIS, AVHRR, TRMM VIRS and ATSR) are followed by a more detailed overview of some of the fire detection algorithms developed for these sensors.

3.1 The MODIS Instrument

The MODIS instrument is installed aboard Terra and Aqua, two satellites that orbit Earth at a distance of 705 km as part of NASA's Earth Observing System (EOS). Terra was launched December 18, 1999, carrying the

Protoflight Model. The Flight Model 1 followed on May 4, 2002 aboard Aqua. With swath dimensions of 2330 km (cross track) by 10 km (along track at nadir), these two MODIS instruments together provide global coverage every one or two days (NASA, 2005).

MODIS pixels have a triangular response in the along track direction (Kaufman et al., 1998). This means that the pixel's real foot print is not a square with a side length the nominal channel resolution, but a rectangle with the dimensions of the nominal channel resolution across track and 2 times the nominal resolution along track. Although the response is weighted to emphasize the signal retrieved form the center of the observed area, each pixel contains spectral information belonging to the two neighboring pixels in along track direction. Figure 3.1 (p 24) shows how, due to this design, one object can contribute to the radiance of two pixels.

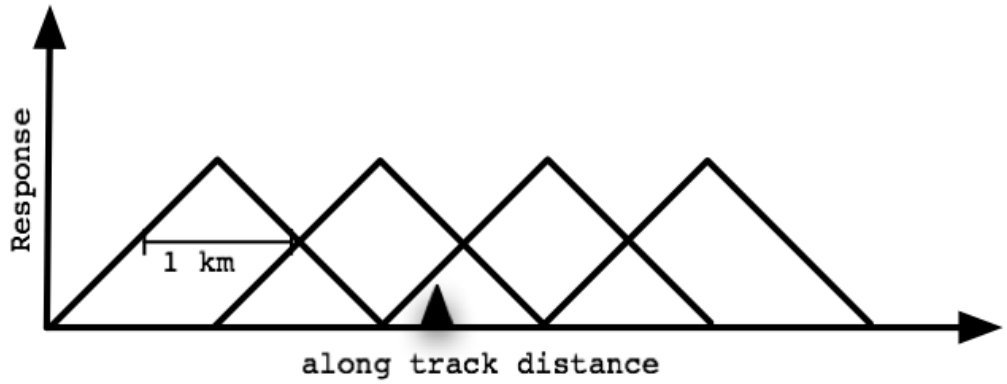

Figure 3.1: MODIS triangular response in along track direction. The triangle depicts an object that falls within two pixels. After Kaufman et al. (1998).

Wolfe et al. (2002) studied the geolocation precision of the operational MODIS data. They conclude that the geolocation accuracy has a mean error of 18 m across-track and 4 m along track with standard deviations of 38 m and 40 m.

MODIS has a total of 36 spectral bands covering the range from 0.4 μm

to 14 μm of the electromagnetic spectrum at varying nadir resolutions of 250, 500 and 1000 meters. Table 3.1 (p 26) gives an overview of all channels of MODIS. Three of these channels are commonly used for the detection o active fires: the two 4 μm channels 21 and 22 and the 11 μm channel 31 (Flasse and Ceccato, 1996; Li et al., 2000a; Justice et al., 2002). The channels 21 and 22 both cover the same spectral range which was chosen because it is not affected by water vapor absorption (Kaufman and Justice, 1998). The two 4 μm bands are different in their saturation and Signal-to-Noise ratio (SNR). Channel 22 saturates at about 331 K whereas channel 21 saturates at approximately 500 K. The higher saturation temperature of channel 21 makes it possible to obtain information on hot and big fires, that saturate channel 22. Channel 21 however has a higher SNR than channel 22, hence channel 22 is the preferred channel until it saturates. Channel 31 saturates at around 340 K on MODIS Aqua and 400 K on MODIS Terra (Giglio et al., 2003a). The 2.1 μm channel 7 saturates at roughly 570 K (Kaufman and Justice, 1998).

The channels 21, 22 and 31 have 10 sensors of 1000 m resolution at nadir and channel 7 has 20 sensors of 500 m resolution at nadir. The figures 3.2 to 3.5 show the spectral response functions (SRF) for the channels 7, 21, 22 and 31. The spectral response function defines the sensor's sensitivity to incoming electromagnetic energy. The figures show that each sensor of each channel has slightly different spectral properties and that the spectral characteristics of the two MODIS sensors differ significantly apart from channel 7 which shows the same spectral response for both sensors.

The MODIS unique combination of temporal and spatial resolution and spectral characteristics make it a highly useful platform for global fire monitoring (Li et al., 2000a).

Table 3.1: Specifications and main applications of all MODIS channels. Source: NASA (2005)

Primary Use	**Band**	**Bandwidth (nm)**	**Spectral Radiance (W m^{-2} μm^{-1} sr^{-1})**	**Required SNR**
Land/Cloud/Aerosols Boundaries	1	620 - 670	21.8	128
	2	841 - 876	24.7	201
Land/Cloud/Aerosols Properties	3	459 - 479	35.3	243
	4	545 - 565	29.0	228
	5	1230 - 1250	5.4	74
	6	1628 - 1652	7.3	275
	7	2105 - 2155	1.0	110
Ocean Color/ Phytoplankton/ Biogeochemistry	8	405 - 420	44.9	880
	9	438 - 448	41.9	838
	10	483 - 493	31.1	802
	11	526 - 563	27.9	754
	12	546 - 556	21.0	750
	13	662 - 672	9.5	910
	14	673 - 683	8.7	1087
	15	743 - 753	10.2	586
	16	862 - 877	6.2	516
Atmospheric Water Vapor	17	890 -920	10.0	167
	18	931 - 941	3.6	57
	19	915 - 965	15	250
Primary Use	**Band**	**Bandwidth (μm)**	**Spectral Radiance (W m^{-2} μm^{-1} sr^{-1})**	**Required NETD**
Surface/Cloud Temperature	20	3.660 - 3.840	0.45(300K)	0.05
	21	3.929 - 3.989	2.38(335K)	2.00
	22	3.929 - 3.989	0.67(300K)	0.07
	23	4.020 - 4.080	0.79(300K)	0.07
Atmospheric Temperature	24	4.433 - 4.498	0.17(250K)	0.25
	25	4.482 - 4.549	0.59(275K)	0.25
Cirrus Clouds Water Vapor	26	1.360 - 1.390	6.00	150(SNR)
	27	6.535 - 6.895	1.16(240K)	0.25
	28	7.175 - 7.475	2.18(250K)	0.25
Cloud Properties	29	8.400 - 8.700	9.58(300K)	0.05
Ozone	30	9.580 - 9.880	3.69(250K)	0.25
Surface/Cloud Temperature	31	10.780 - 11.280	9.55(300K)	0.05
	32	11.770 - 12.270	8.94(300K)	0.05
Cloud Top Altitude	33	13.185 - 13.485	4.52(260K)	0.25
	34	13.485 - 13.785	3.76(250K)	0.25
	35	13.785 - 14.085	3.11(240K)	0.25
	36	14.085 - 14.385	2.08(220K)	0.35

3.2 Spectral Properties of Blackbodies of typical bushfire Temperatures

Assuming that fires are blackbodies, they emit radiation over a wide range of the electromagnetic spectrum. Their radiance $L(\lambda, T)$ for a given

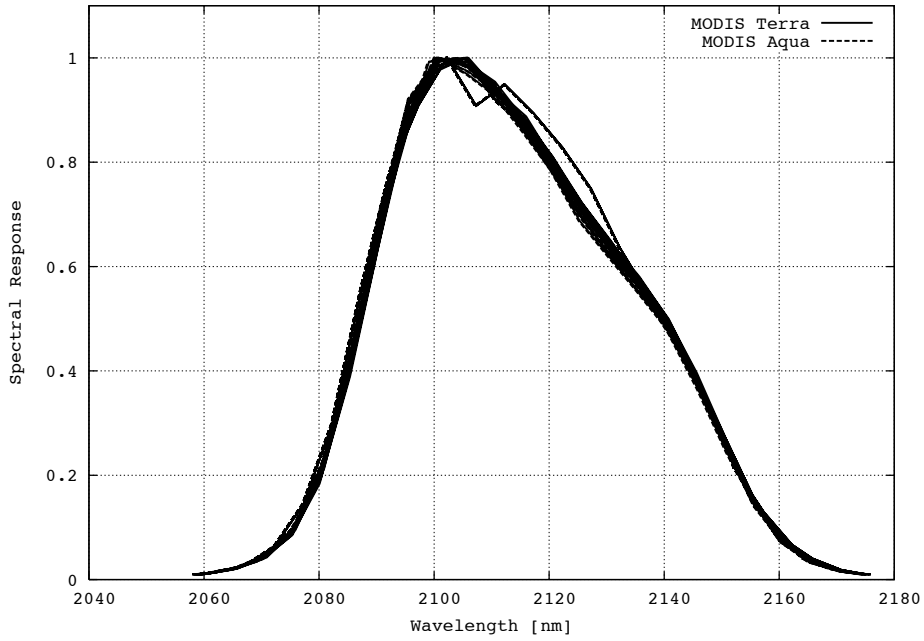

Figure 3.2: SRF of channel 7 of MODIS Terra and MODIS Aqua. Each of the 20 lines represents one detector. The lines can be so close to each other that it is not always possible to differentiate between them.

wavelength (λ) and a temperature (T) can be described using Planck's Law:

$$L(\lambda, T) = \frac{2\,hc^2}{\lambda^5} \times \frac{1}{e^{\frac{hc}{k\lambda T}} - 1} \tag{3.1}$$

where

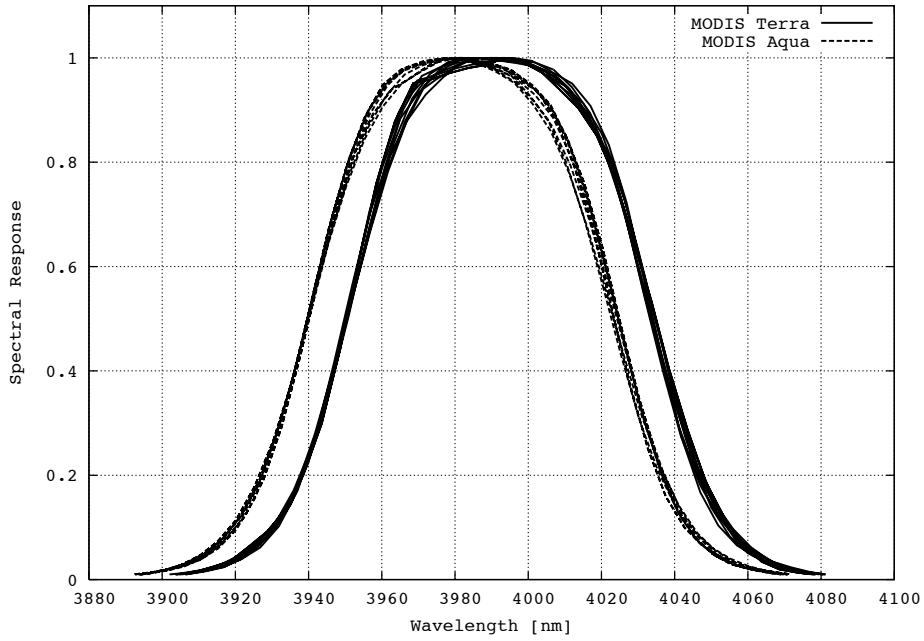

Figure 3.3: SRF of channel 21 of MODIS Terra and MODIS Aqua. Each of the 10 lines represents one detector. The lines can be so close to each other that it is not always possible to differentiate between them.

$L =$ radiance in W m^{-}2 μm^{-}1 sr^{-}1
$k = 1.381 \times 10^{-23}\, JK^{-}1,$
$c = 2.998 \times 10^{8}\, ms^{-}1,$
$h = 6.626 \times 10^{-34}\, Js^{-}10,$
$T =$ Temperature(K).

Figure 3.6 (p 31) shows the Planck function of several blackbodies depending on wavelength and the spectral position of the MODIS bands 7, 21/ 22 and 32. The graphs of 600, 750 and 900 K represent blackbodies of typical bushfire temperatures (Wooster et al., 2003; Kaufman and Justice, 1998) whereas the 300 K graph illustrates the blackbody radiation of a typical non-fire background. The figure 3.6 (p 31) shows that the thermal

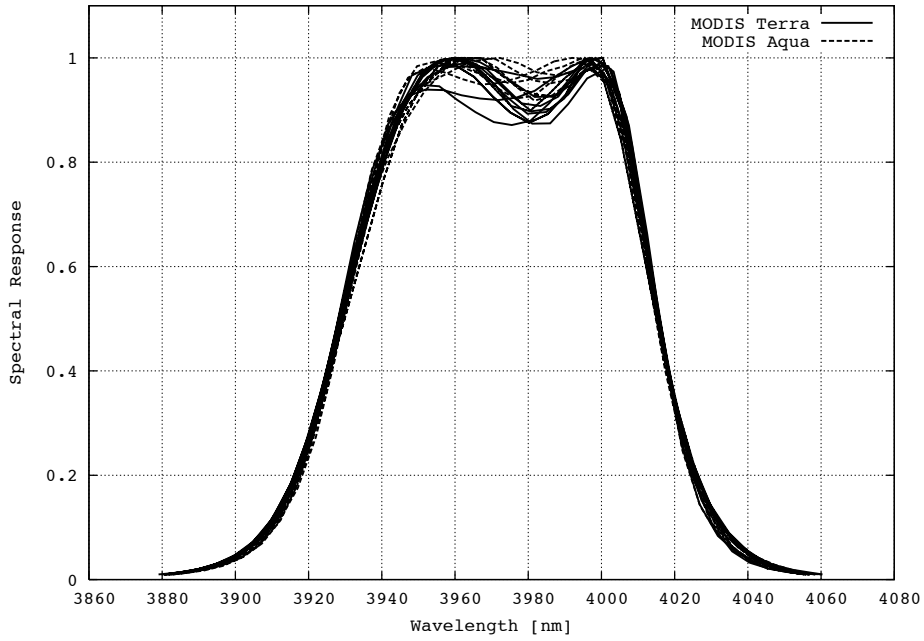

Figure 3.4: SRF of channel 22 of MODIS Terra and MODIS Aqua. Each of the 10 lines represents one detector. The lines can be so close to each other that it is not always possible to differentiate between them.

radiation emitted by bushfires is significantly greater in the MIR range than in the TIR range (Li et al., 2000a). It further shows a strong emission in the NIR range (Barducci et al., 2003).

Figure 3.6 (p 31) also indicates that the MODIS channels 7, 21/22 are very well positioned to detect fires with channel 31 being a background channel for channels 21/22 as fires show much less radiation in the 11 μm region than in the 4 μm range while a typical non-fire surface reveals a similar radiance in both regions of the spectrum.

This assumption is supported by figure 3.7 (p 32). This figure shows the wavelength of maximum emitted energy according to Wien's Displace-

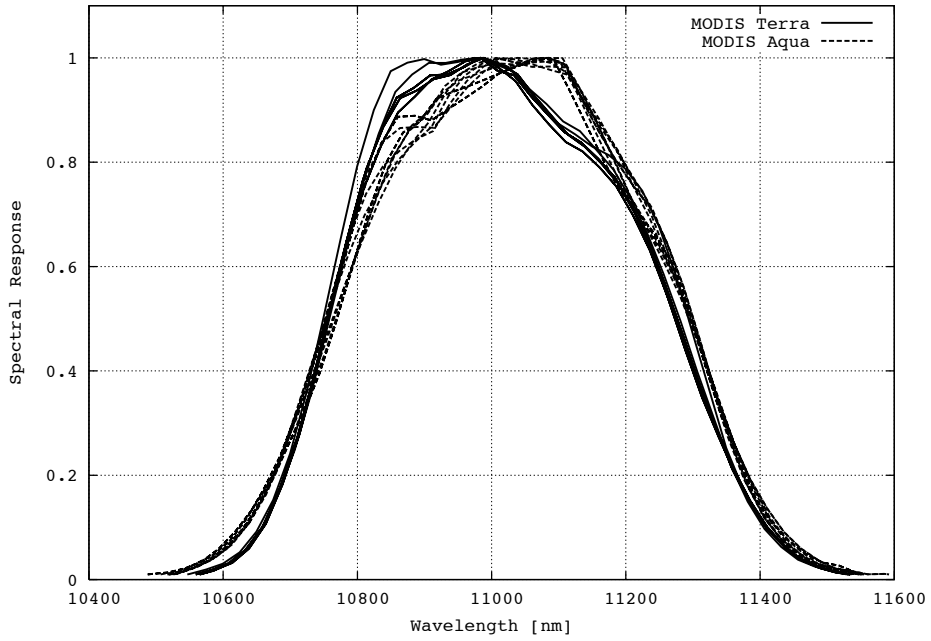

Figure 3.5: SRF of channel 31 of MODIS Terra and MODIS Aqua. Each of the 10 lines represents one detector. The lines can be so close to each other that it is not always possible to differentiate between them.

ment law. Figure 3.7 shows that channel 31 of MODIS is positioned at the region of the electromagnetic spectrum where a blackbody of about 300 K has it's radiation maximum. Channels 21/22 are located between the maxima of a smoldering fire (around 600 K) and a flaming fire (roughly 900 K) (Wooster et al., 2003; Kaufman and Justice, 1998). Channel 7 is spectrally located at the range of the spectrum where blackbodies of temperatures in the region of 1400 K have their maximum thermal emission.

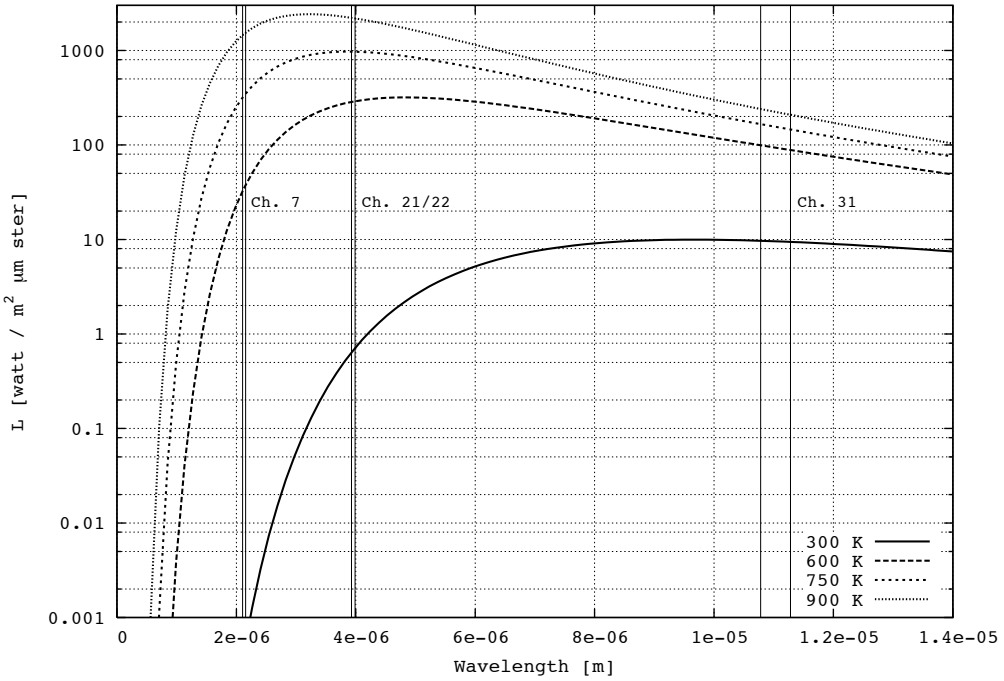

Figure 3.6: Planck function for Blackbodies of different temperatures and the locations of channels 7, 21/22 and 31 of MODIS

3.3 Concepts of current MODIS Fire Detection Algorithms

Most of the fire detection algorithms that have so far been developed have their origins in algorithms developed for the NOAA/AVHRR platform (Justice et al., 2002). The exception is an algorithm proposed by Petitcolin and Vermote (2001) which uses a different approach. These algorithms will be reviewed in the following subsections.

Although the 2.1 μm channel of MODIS, channel 7, is currently not being used by any operational fire detection algorithm, figures 3.6 and 3.7 on pages 31 and 32 in section 3.2 show its theoretical capacity for this application. This potential of channel 7 was also mentioned by Kaufman

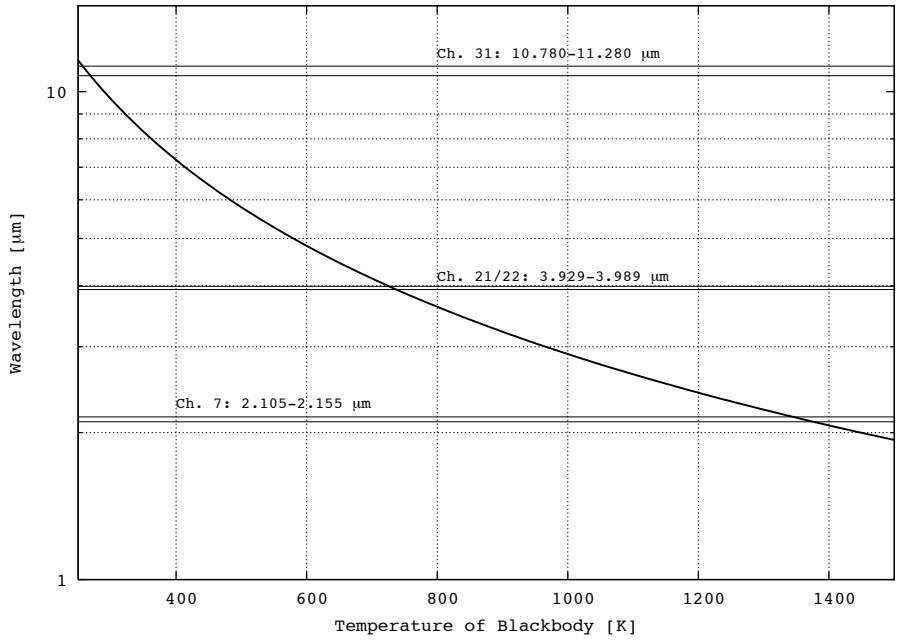

Figure 3.7: Wavelength of maximal radiation of Blackbodies ranging from 300 to 1500 K and the bandwidths of channels 7, 21/22 and 31 of MODIS

and Justice (1998) and Chuvieco (1999). Kaufman and Justice (1998) attest channel 7 to be highly sensitive to a flaming fire of temperatures around 1000 K and somewhat sensitive to smoldering fires around 600 K.

The aim of all fire detection algorithms is to classify pixels according to wether they can be characterized as containing a fire or not, possibly containing a cloud, are background pixels that do not contain fires or are invalid due to missing data. These classifications will be denoted as 'fire', 'non-fire', 'cloud', 'background' and 'invalid'.

An overview of the notations that will be used in the discussion of the different algorithms is shown in table 3.2 (p 33). All notations might be subscripted with a number indicating the center wavelength of the given

channel in μm. In the case where a notation is required to describe a product calculated from two channels, two comma separated numbers can be given indicating the two channels.

Table 3.2: Notations used in the discussion of the different fire detections algorithms

Notation	Meaning
T	equivalent blackbody brightness temperature
ΔT	difference between T of two channels
σT	standard deviation of T
$\sigma \Delta T$	standard deviation of differences of T
T_b	equivalent blackbody brightness temperature of background pixel
ΔT_b	difference between T_b of two channels
σT_b	standard deviation of T_b
$\sigma \Delta T_b$	standard deviation of differences of T_b
$mean \Delta T_b$	mean of the background differences
$\delta \Delta T_b$	mean absolute deviations of background differences
ρ	Reflectance

3.3.1 Algorithm using Blackbody Temperatures

Algorithms based on methods developed for NOAA/AVHRR use blackbody brightness temperatures derived from channels 21/22 and 31. These temperatures are denoted T_4 and T_{11} respectively (Kaufman and Justice, 1998; Giglio et al., 2003a; Justice et al., 2002). They utilize the significantly different spectral responses to a hot target between of the MIR and the TIR channels (Dozier, 1981). These algorithms search for a significant increase of radiance in channel 21/22 as an indicator of the presence of a fire. This increase can either be absolute with reference to a background level or relative to the radiance detected in channel 31 (Giglio et al., 2003a). This amplification of radiance with an increase in temperature in channel 7 and channels 21/22 is shown in figure 3.6 (p 31).

Assuming that, for the moment, the atmosphere has no influence to the signal detected by a satellite, the upwelling radiance measured by the sensor pointing downward can be calculated by integrating the Planck function and the SRF of the sensor (Dozier, 1981):

$$L(T) = \frac{\frac{1}{\pi}\int_0^\infty \varepsilon_\lambda \beta(\lambda, T) SRF(\lambda) d\lambda}{\int_0^\infty SRF(\lambda) d\lambda} \tag{3.2}$$

where

$L(T)$	upwelling thermal radiance (W m^{-2} μm^{-1} sr^{-1}),
T	Temperature (K),
$\beta(\lambda, T)$	Planck function (W m^{-3}),
ε	Emissivity,
λ	wavelength (m),
$SRF(\lambda)$	spectral response function.

Although ε_λ can vary within the bandwidth of one channel, it is commonly assumed to be constant (Dozier, 1981). Hence, the subscript is dropped and ε can be moved outside the integral. Figure 3.8 (p 35) shows L(T) as a function of temperature for the channels 7, 21/22 and 31 for MODIS Terra. The values have been calculated according to equation 3.2 with the assumption that the observed pixel is a blackbody (ε=1). This figure again shows the effect of Wien's displacement law. The rate of increase of L(T) with increasing temperature is such that

$$\text{channel7} > \text{channel21/22} > \text{channel31}$$

because the peak of the Planck function shifts to shorter wavelengths with increasing temperatures (Dozier, 1981).

The calculation of L(T), as shown in figure 3.8, furthermore assumes that the pixel is a blackbody of uniform temperature. Considering the size of

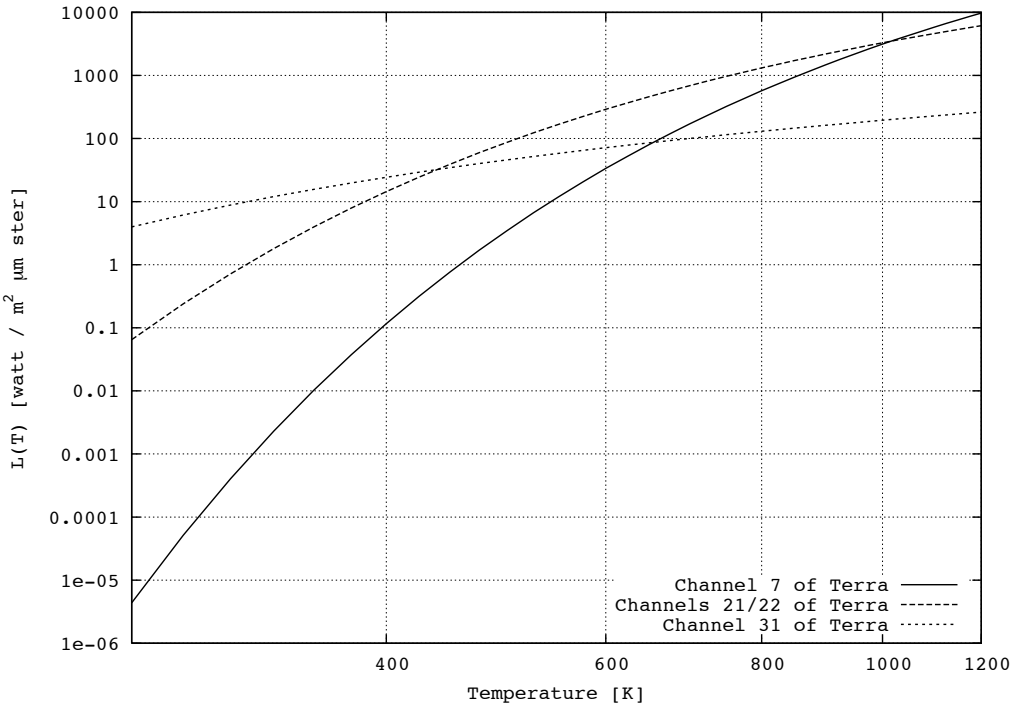

Figure 3.8: L(T) for channels 7, 21/22, 31 of MODIS Terra in the temperature range from 200 to 1000 K. The observed pixel is assumed to be a blackbody (ε=1).

a MODIS pixel, this is highly unlikely in the case of a fire within the pixel. A target fire pixel thus has to be assumed to be a 'mixed' pixel with a target (fire) temperature T_{fire}, a background temperature T_b and a fraction p of the pixel that is covered by the fire (p, $0 \leq p \leq 1$) (Dozier, 1981). T_{fire} and T_b are assumed to be uniform within a given pixel. L(T) measured by the sensor will then no longer be dependent on the 'real' target temperature but on a composite temperature T_{comp} comprising endmembers T_{fire} and T_b. According to Dozier (1981), T_{comp}, in absence of any atmospheric effects, is defined as

$$T_{comp} = L^{-1}[pL(T_{fire}) + (1-p)L(T_b)] \tag{3.3}$$

where

L^{-1} inverse function of L(T).

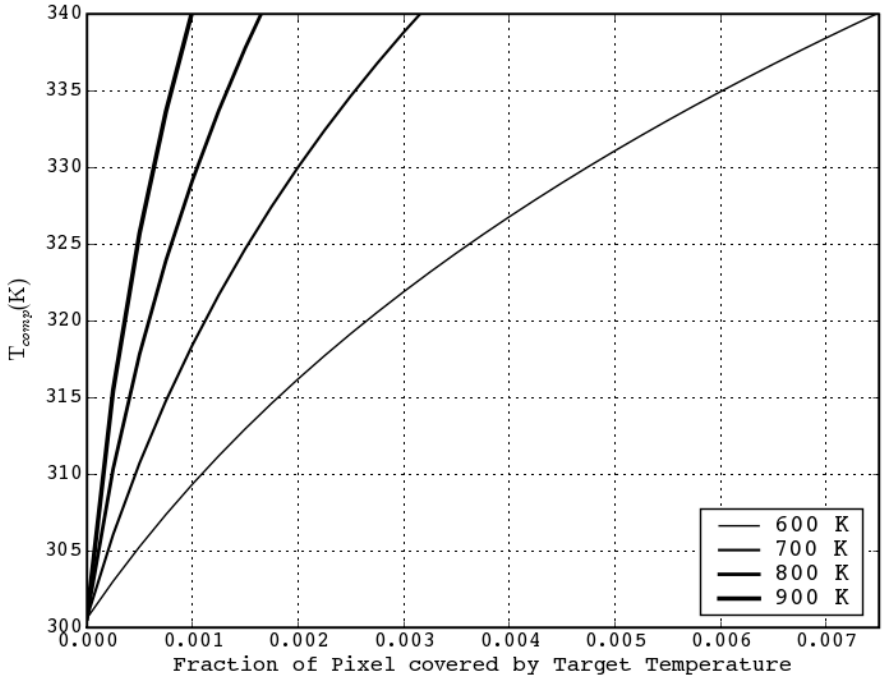

Figure 3.9: T_{comp} for MODIS channel 21 in absence of atmospheric effects for targets of 600, 700, 800 and 900K. T_b is 300 K

The method to inverse L(T) for MODIS used in this work is described in Maier (2002). Figures 3.9 (p 36) and 3.10 (p 37) show T_{comp} for channels 21 and 31 of MODIS. Figure 3.9 illustrates the effect fires have on the BBT as calculated from the measured radiances in MODIS channel 21. Algorithms using BBTs to detect fires use this effect by looking for pixels where BBT in channel 21 is above a value expected to be the maximum possible without any fire influence. They furthermore utilize the circumstance that fires have a smaller effect on the BBT in channel 31 (figure

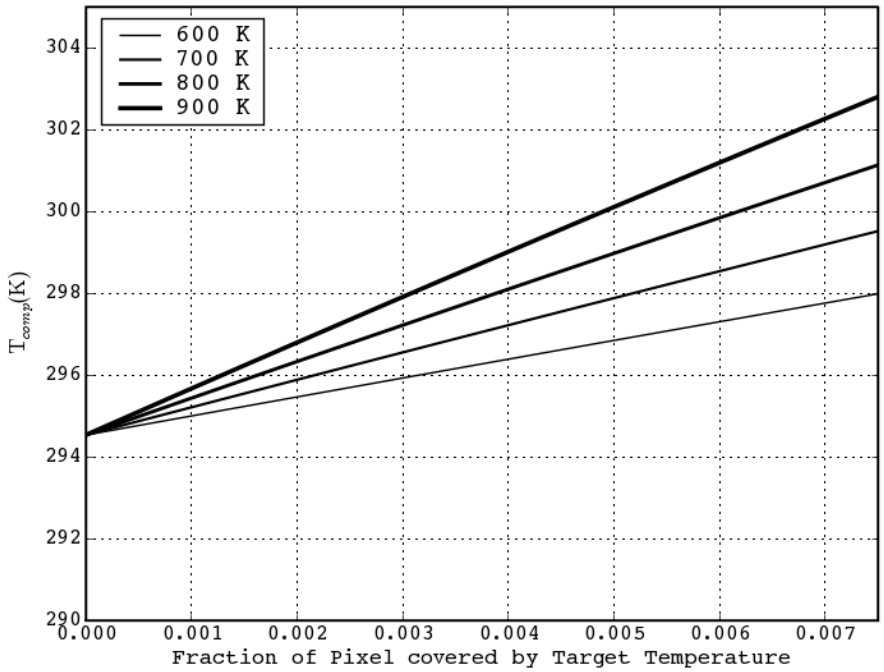

Figure 3.10: T_{comp} for MODIS channel 31 in absence of atmospheric effects for targets of 600, 700, 800 and 900K. T_b is 300 K

3.10) by thresholding the difference between T_{comp} of channels 21/22 and 21. (figure 3.11, p 38).

Kaufman and Justice (1998)

This is the original algorithm developed by the MODIS Science Team prior to the launch of Terra. It is also referred to as 'MOD14'. This algorithm does not make use of pixels with a scan angle of more than 45° as double detections of the same fire are possible due to the spatial triangular response of MODIS that emphasizes the radiometric signal of the central region of the observed pixel.

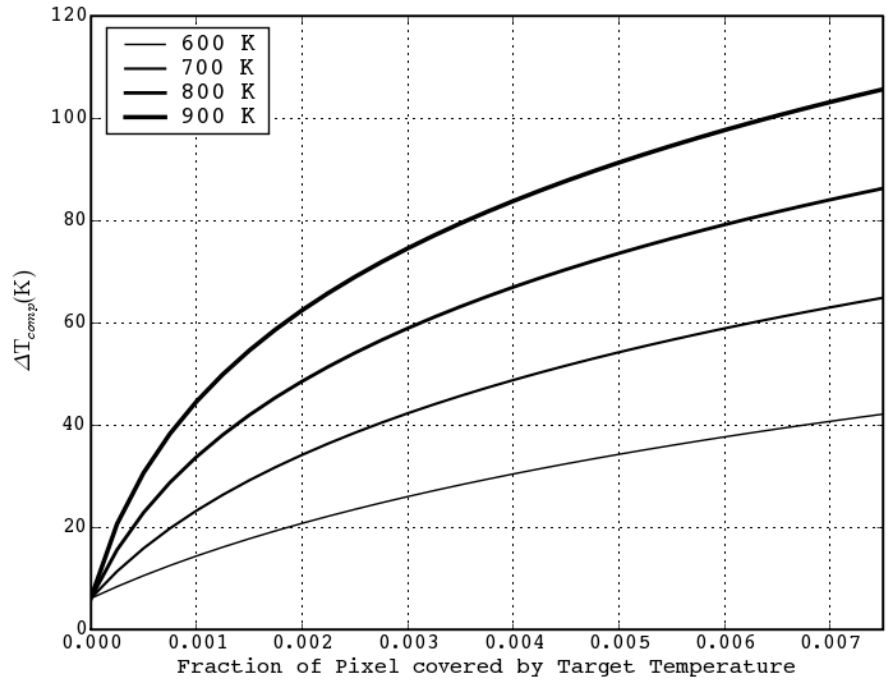

Figure 3.11: Differences of the T_{comp}s for 4 and 11 μm shown in figure 3.9 (p 36) and 3.10 (p 37)

The algorithm defines a background temperature for each observed pixel using a n by n pixel array centered on the pixel of interest. Only those pixels within this box that are not cloud or water and are free of fires are considered valid background pixels. A background pixel is considered being contaminated by a fire if:

$$
\begin{array}{ll}
T_4 - T_{11} \geq 20\ K & \text{(day)} \\
T_4 - T_{11} \geq 10\ K & \text{(night)} \\
\text{and} & \\
T_4 > 320\ K & \text{(day)} \\
T_4 > 305\ K & \text{(night).}
\end{array}
$$

The n by n pixel background window extends spatially until at least 25%

of the pixels are valid or it reaches a maximum size of 21 by 21 pixels.

All pixels that satisfy:

$$\begin{array}{ll} T_4 - T_{11} < 5\ K & \text{(day)} \\ T_4 - T_{11} < 3\ K & \text{(night)} \\ \text{or} & \\ T_4 < 315\ K & \text{(day)} \\ T_4 < 305\ K & \text{(night).} \end{array}$$

are rated as non-fire and are excluded from any further tests. For the valid background pixels, two standard deviations are calculated for the n by n pixel array: namely, $\sigma T_{b,4}$ and $\sigma T_{b,4,11}$. Pixels that fulfill

$$\begin{cases} T_4 > 360\ K & (day) \\ T_4 > 330\ K & (night) \\ or & \\ T_4 > T_{b,4} + 4\sigma T_{b,4} & \\ or & \\ T_4 > 320\ K & (day) \\ T_4 > 315\ K & (night) \end{cases}$$

$$and$$

$$\begin{cases} \sigma T_{b,4,11} > \sigma T_{b,4,11} + 4\sigma T_{b,4,11} & \\ or & \\ T_4 - T_{11} > 20\ K & (day) \\ T_4 - T_{11} > 10\ K & (night) \end{cases}$$

are flagged as pixels containing a fire. The last step rejects pixels marked as fire due to sunglint during daytime observations. If a fire pixel satisfies:

$$\rho_{0.64} > 0.3$$
and
$$\rho_{0.86} > 0.3,$$

with $\rho_{0.64}$ and $\rho_{0.86}$ being the reflectances in the 0.64 μm and the 0.86 μm channels, it is rejected due to sunglint.

Justice et al. (2002)

This algorithm follows the same principles as the algorithm proposed by Kaufman and Justice (1998) but incorporates some improvements following two years of experience with the original MODIS fire detection algorithm. The same notation is used as in Kaufman and Justice (1998) and additionally $\rho_{0.86}$, the reflectance of the 0.86 μm channel, channel 2 is incorporated.

The first test examines if a pixel potentially contains an active fire. If a pixel satisfies:

$$\begin{aligned}
&T_4 - T_{11} < 10\ K && \text{(day)}\\
&T_4 - T_{11} < 3\ K && \text{(night)}\\
&\text{or} &&\\
&T_4 < 315\ K && \text{(day)}\\
&T_4 < 305\ K && \text{(night)}\\
&\text{or} &&\\
&\rho_{0.86} > 0.3 && \text{(daytime only)},
\end{aligned}$$

it is immediately excluded from the potential fire pixel classification. The next steps test the remaining pixels if they satisfy the conditions for absolute fire detection which are:

$$
\begin{array}{ll}
T_4 > 360\ K & \text{(day)} \\
T_4 > 330\ K & \text{(night)} \\
\text{or} & \\
T_4 > 330\ K & \text{(day)} \\
T_4 > 315\ K & \text{(night)} \\
\text{and} & \\
T_4 - T_{11} > 25\ K & \text{(day)} \\
T_4 - T_{11} > 10\ K & \text{(night).}
\end{array}
$$

If a pixel that is flagged as a possibly containing a fire does not meet one of the above criteria, it is tested with respect to how it is distinguished from its background using the standard deviations $\sigma T_{b,4}$ and $\sigma T_{b,4,11}$ as well as the mean$(T_{b,4})$ and the median$(T_{b,4,11})$ of the background. If one of the standard deviation has a value below 2 K then 2 K is used instead. The background is defined in a similar way as was done by Kaufman and Justice (1998). A pixel is defined as fire-free and is thus valid for consideration as a background pixel if it meets the tests:

$$
\begin{array}{ll}
T_4 < 325\ K & \text{(day)} \\
T_4 < 315\ K & \text{(night)} \\
\text{and} & \\
T_4 - T_{11} < 20\ K & \text{(day)} \\
T_4 - T_{11} < 10\ K & \text{(night).}
\end{array}
$$

If the background n by n array reaches 21 by 21 pixels and the minimum required criterion for a valid background (that being 25% of the pixels with a minimum number if 6 pixel) is not met, the fire detection procedure cannot be used and the pixel is flagged as unkown. A pixel having a valid background is classified as containing a fire if it conforms with:

$$
\begin{array}{l}
T_4 > \text{mean}\,(T_{b,4}) + 3\sigma T_{b,4} \\
\text{and} \\
T_4 - T_{11} > \text{median}\,(T_{b,4,11}) + 3\sigma T_{b,4,11}.
\end{array}
$$

Pixels flagged as fire are rejected due to sunglint following the same condition as proposed by Kaufman and Justice (1998) and if the pixels additionally lies within 40° location of the specular reflection.

3.3.2 Algorithms utilizing MIR Reflectance

The method suggested by Petitcolin and Vermote (2001) does not make use of the radiance but of the surface reflectance in the MIR range. This approach calculates the difference between the reflectance of channel 21/22 and a guessed reflectance derived from channel 7 reflectances. If this difference is greater than 0.1 the corresponding pixel is marked as containing a fire.

3.4 Fire Detection based on other Instruments than MODIS

3.4.1 Advanced Very High Resolution Radiometer (AVHRR)

The AVHRR instrument aboard the NOAA polar orbiting satellite series provides daily coverage at a moderate resolution of $\sim$1 km at nadir (Li et al., 2000a). It has five spectral channels with central wavelengths of 0.65, 0.86, 3.8, 10.8 and 11.9 μm of which the 3.8 and 10.9 μm channels are the most useful for the detection of active fires (Giglio et al., 1999). A range of fire detection algorithms has been developed for the AVHRR series of instruments.

The most basic of those algorithms are only based on thresholds of the 3.8 μm channel (Li et al., 2000a). These algorithms suffer from the influ-

ence of reflected solar radiation from bright surfaces or partial cloud contamination of the observed pixel. Further, the low saturation brightness temperature of 320-331 K (depending on which instrument of the series is used) of the 3.8 μm channel (Li et al., 2000a) which can be exceeded by bright surfaces even if no fire is present.

More advanced algorithms utilize more than one AVHRR channel. The most often used is a three step approach for the identification of fires (Li et al., 2000a): firstly, all possible fires are identified using the 3.8 μm channel, secondly the 10.9 μm channel is used to eliminate clouds and thirdly the difference between the two channels is used to separate fires from a warm non-fire background. Some algorithms incorporate further tests to identify false detections due to highly reflective surfaces or certain types of clouds. One example for a multi-channel algorithm that relies on fixed thresholds was developed by Arino et al. (1993). It relies on five tests using the brightness temperatures of the 3.8 and 10.9 μm channels of AVHRR denoted T_4 and T_{11} as well as the reflectances in the 0.65 and 0.86 μm channels denoted $\rho_{0.65}$ and $\rho_{0.86}$. The tests are:

$$\begin{aligned} T_4 &> 320K \\ T_4 - T_{10} &> 15K \\ T_{11} &> 245K \\ \rho_{0.65} &< 0.25 \\ |\rho_{0.65} - \rho_{0.86}| &> 0.01. \end{aligned}$$

A pixel has to satisfy all these tests to be classified as containing a fire. Another multi-channel fixed-threshold algorithm was developed by Li et al. (2000b).

The most elaborate algorithms not only make use of more than one channel but also do not entirely rely on fixed thresholds. One of those is the al-

gorithm developed by Justice et al. (1996). This algorithms first identifies possible fire pixels using a fixed threshold based on the 3.8 μm channel:

$$T_4 \geq 316\ K.$$

Pixels that don't satify this condition are classified as non-fire pixels. For each pixel that has been identified as possibly containing a fire a background brightness temperature is calculated using a spatial window centered around the potential fire pixel. The window grows in size until it has either reached a size of 21 by 21 pixels or until a sufficient number (25% of the window but at least 3 pixels) of valid background pixels has been found. This method is similar to the one used by Kaufman and Justice (1998) described earlier. A valid background pixel is flagged as cloud free using an external cloud mask and must not be a potential fire pixel itself. If the algorithm cannot find a sufficient number of valid background pixels, the potential fire pixels is flagged as unknown. Otherwise, several statistics are computed for the background: the mean brightness temperature of channel 4 ($meanT_{b,11}$) and the mean and standard deviation of the difference between the brightness temperatures of channel 3 and 4 ($meanT_{b,4,11}$ and $\sigma T_{b,4,11}$). Furthermore a reference value ΔT is defined as either $2\sigma T_{b,4,11}$ or 5 K, which ever is greater. The potential fire pixels is then flagged as a fire pixel if is satisfies:

$$\begin{aligned} \Delta T_{4,11} &> meanT_{b,4,11} + \Delta T \\ T_{11} &\geq meanT_{b,11}. \end{aligned}$$

Flasse and Ceccato (1996) developed another contextual fire detection algorithm for AVHRR based on the one by Justice et al. (1996). The main difference was that it includes a test based on the reflectance in the 0.86 μm channel to rule out false detections caused by an increase of T_4 due

to reflection rather than emission.

3.4.2 Along Track Scanning Radiometer (ATSR)

The ATSR instruments is aboard the Second European Remote-Sensing Satellite (ERS2) operated by the European Space Agency (EAS). The sensor provides global coverage (at the equator) every three days at 1 km nadir resolution (Mota et al., 2005). It has seven channels with central wavelengths at 0.55, 0.67, 0.87, 1.6, 3.7, 11.0 and 12 μm. Fire monitoring for the World Fire Atlas (WFA) with ATSR is a combination of a single threshold algorithm based on brightness temperatures of the 3.7 μm channel and two land cover maps, the Global Land Cover map and the MODIS MOD12 land cover map. Pixels that satisfy:

$$T_{3.7} > 308K,$$

are considered fires. The land cover maps are used to eliminate non-vegetation fires. Furthermore, only nighttime observations are used to minimize false alarms caused by highly reflective surfaces, sun-glint and clouds (Mota et al., 2005).

3.4.3 Visible and Infrared Scanner (VIRS)

The VIRS instrument is on board the Tropical Rainfall Measuring Mission (TRMM) satellite launched in 1997. The satellite gives day and night coverage of the area within $\pm 40^{\circ}$ of the equator at a resolution of 2.11 km at nadir (Giglio et al., 2000). VIRS has five channels with 0.63, 1.61, 3.75, 10.8 and 12 μm as center wavelength, numbered channels 1 to 5.

A cloud mask is applied before pixels are tested for fires. Daytime pixels are considered contaminated by clouds if they satisfy (Giglio et al., 2003b):

$$
\begin{aligned}
&(\rho_{0.63} + \rho_{1.61}) > 1.2 \\
&\text{or} \\
&T_{12} < 265\ K \\
&\text{or} \\
&(\rho_{0.63} + \rho_{1.61}) > 0.8 \\
&\text{and} \\
&T_{12} < 285\ K,
\end{aligned}
$$

with $\rho_{0.63}$ and $\rho_{1.61}$ being the reflectances in channels 1 and 2 and T_{12} being the brightness temperature in channel 5. Nighttime pixels have to satisfy one single condition:

$$T_{12} < 265\ K$$

to be classified as cloud. Water pixels are identified using the 1 km Multi-angle Imaging Spectroradiometer's (MISR) Digital Terrain Elevation Data (DTED) Intermediate Dataset (Giglio et al., 2003b). The fire detection scheme uses an approach very similar to the earlier discussed contextual algorithm developed by Justice et al. (1996) for AVHRR. Pixels are identified as potentially containing a fire if they satisfy:

$$
\begin{aligned}
&T_{3.7} > 310\ K \quad \text{(day)} \\
&\text{and} \\
&\rho_{1.61} > 0.32 \quad \text{(day)} \\
&\text{and} \\
&\Delta T_{3.7,11} > 6\ K \quad \text{(day)}
\end{aligned}
$$

for daytime observations (Giglio et al., 2003b). At night pixels are not tested for $\rho_{1.61}$ and are classified as potential fire pixels if they fulfill (Giglio et al., 2003b):

$$
\begin{aligned}
&T_{3.7} > 306\ K \quad \text{(night)} \\
&\text{and} \\
&\Delta T_{3.7,11} > 6\ K \quad \text{(night)}
\end{aligned}
$$

Similar the algorithm developed by Justice et al. (1996) a background is defined using a window centered around the pixel potentially containing an active fire. The window starts at a size of 5 by 5 pixels and can grow to 21 by 21 pixels. A valid background window must contain 25% and at least 6 valid background pixels (Giglio et al., 2003b). Pixels are considered valid background pixels if they are valid observations, not cloud or water and do not contain a background fire. Background fire pixels are those that satisfy:

$$
\begin{aligned}
&T_{3.7} > 318\ K \quad \text{(day/night)} \\
&\text{and} \\
&\Delta T_{3.7,11} > 12\ K \quad \text{(day/night)}
\end{aligned}
$$

If a valid background temperature cannot be found, the potential fire pixel is flagged as unknown otherwise the mean ($mean\Delta T_{b,3.7,11}$) and the mean absolute deviation ($\delta\Delta T_{b,3.7,11}$) of $T_{3.7} - T_{11}$ as well as the mean ($mean\Delta T_{b,11}$) and mean absolute deviation ($\delta\Delta T_{b,11}$) of T_{11} are calculated for the valid background pixels (Giglio et al., 2003b). Potential fire pixels have to satisfy:

$$
\begin{aligned}
&\Delta T_{3.7,11} > mean\Delta T_{b,3.7,11} + 3.5\delta\Delta T_{b,3.7,11} \quad \text{(day/night)} \\
&\text{and} \\
&\Delta T_{3.7,11} > mean\Delta T_{b,3.7,11} + 6\ K \quad \text{(day/night)} \\
&\text{and for daytime pixels only:} \\
&T_{11} > mean\Delta T_{b,11} + \delta\Delta T_{b,11} - 1.5\ K \quad \text{(day)}
\end{aligned}
$$

to be regarded as valid fire detections for nighttime observations or to be subjected to further tests for daytime observations, otherwise they are

flagged as non-fire. For daytime observations pixels have to further satisfy a test for sunglint. This test uses θ_g defined by,

$$cos\theta_g = cos\theta_v cos\theta_s - sin\theta_v sin\theta_s cos\phi$$

with θ_v and θ_s are the sensor view and solar zenith angles and ϕ is difference between the sun and sensor view azimuth angles. The test also takes the number of water pixels (N_w) within a 3 by 3 window around the potential fire pixel into account (Giglio et al., 2003b). If the potential fire detection pixel satisfies any of the conditions:

$\theta_g < 5^\circ$
or
$\theta_g < 15^\circ$
and
$\rho_2 > 0.2$
or
$\theta_g < 20^\circ$
and
$N_w > 0$,

it is rejected as a valid detection due to potential sunglint contamination.

3.5 Summary

This review has shown what influences fires of different temperatures are expected to have on the MODIS channels in the atmospheric windows around 2, 4 and 10 μm. The same effects apply to other sensors observing the same atmospheric windows. It was further shown how the approach described by Dozier (1981) exploits these effects in order to detect active fire covering only a fraction of the pixel.

The fire detection algorithms introduced in this chapter all work in the atmospheric windows around 2 and 10 μm. Apart from the algorithm briefly described by Petitcolin and Vermote (2001), they all make us of equivalent blackbody brightness temperatures employing the principles described by Dozier (1981). These algorithms vary in regards to the chosen thresholds, depending on the instrument's sensitivity and the region of the Earth to which each algorithm is applied. Some of the algorithms employ techniques to adopt thresholds depending on the observed environment. However, none of the algorithms attempts to overcome significant problems, such as the saturation of the channels observing the atmospheric window around 4 μm by utilizing spectral bands that operate outside the windows used by Dozier (1981).

In the case of MODIS, there is such an opportunity. MODIS channel 7, operating in the atmospheric window around 2 μm, has been identified to be potentially useful for the detection of active fires by Kaufman and Justice (1998); Chuvieco (1999) as well as in this work. However, there has not been an attempt to utilize this channel in a fire detection scheme. The 2.1 μm channel of MODIS has the potential to improve fire detection in two ways. Firstly, as shown before, this channel is expected to be only sensitive to large, intense fires. In this case a fire saturates the channels of MODIS operating in the atmospheric window around 4 μm and the 2.1 μm offers the possibility to circumvent this difficulty. Secondly, the native resolution of the 2.1 μm channel is 500 m, double the resolution of the channels currently used in fire detection schemes, providing four times the spatial resolution. Utilizing this channel promises to increase the spatial resolution of fire detection with MODIS with sacrificing coverage or revisit rate.

Chapter 4

Implementation of a Fire Detection Algorithm based on Reflectance change in the 2.1 micron channel of MODIS

Following the physical principles that fire detection algorithms are based on and an overview on how current fire detection algorithms work, this chapter describes a new and different approach to fire detection from satellites. The chapter will show what the required properties of fires are in order to be able detect them using the 2.1 μm channel of MODIS. Based on these fire qualities, this chapter presents an example of such a fire detection algorithm.

4.1 Apparent Reflectance

Apart from the spectral reflectance defined in chapter 2, this work will also use the term 'apparent reflectance'. This is necessary because of the

way the MODIS reflectance products are calculated. This calculation does not take into account that an observed pixel might contain a fire that significantly adds to the radiation measured by the sensor. Therefore the reflectance of a pixel that contains a sub-pixel fire is not the spectral reflectance

$$\rho(\lambda) = \frac{E_R(\lambda)}{E_I(\lambda)}$$

as defined in equation 2.6, but is defined by

$$\rho(\lambda) = \frac{E_R(\lambda) + E_{fire}(\lambda)}{E_I(\lambda)} \tag{4.1}$$

where

$$E_{fire}(\lambda) \quad = \quad \text{energy emitted by the fire.}$$

In case that a pixel does not contain a fire $E_{fire}(\lambda)$ is equal to zero and the apparent reflectance is equal to the true spectral reflectance. In case this paper refers to 'reflectance' it is assumed to be the apparent reflectance.

4.2 Properties of detectable Fires

The two main contributors to the emitted energy of a fire are its temperature and size. Every algorithm to detect fires of sub-pixel size includes a specific function with these two attributes as variables that describe fires that emit more energy than the algorithm's lower detection limit. If the emission of a fire does not exceed this lower limit, the algorithm is not capable of detecting this fire within a pixel. In order to establish these limits for a fire detection scheme based on the 2.1 micron channel

of MODIS, spectral profiles of pixels that contain fires as well, as those that don't, have been simulated.

4.2.1 Spectral Simulation of Fire affected MODIS Pixels

The model data were calculated for MODIS channels 7, 21/22 and 31 using MODTRAN 4 version 3 release 1, the 1976 US Standard atmosphere (U.S. Government, 1976) and the SRFs shown in figures 3.2 to 3.5. 705 km was chosen as the sensors altitude.

The modelled surfaces were assumed to be lambertian reflectors with independent reflectances for each channel. As fires increase the apparent reflectance in all channels (Petitcolin and Vermote, 2001) increases. Each channel was assigned a separate fire and non-fire reflectance. To further increase the range of simulated scenarios, a range of different non-fire reflectances where modelled for channel 7. The reflecances are denoted $r_{7,b}$, $r_{21/22,b}$ and $r_{31,b}$ in case of no fire and $r_{7,f}$, $r_{21/22,f}$ and $r_{31,f}$ for fire situations. Table 4.1 (p 52) shows the values of the reflectances used for the simulation.

Table 4.1: Reflectance Values used in the Simulation.

Reflectance	**Value**
$r_{7,b}$	0.1 - 0.2 (in 0.01 steps)
$r_{21/22,b}$	0.02
$r_{31,b}$	0.02
$r_{7,f}$	0.5
$r_{21/22,f}$	0.17
$r_{31,f}$	0.17

The background temperatures denoted T_b were modelled from 285 K to 330 K in 5 K steps and the fire temperatures denoted T_f from 600 K to 1200 K in 25 K intervals. Further, variables that were employed in the

model where the day of the year denoted D, the sensor viewing zenith angle denoted VZ and the solar zenith angle (SZ) denoted ϕ. The day of the year was either day 4, day 94, day 184 or day 274. The VZ covered the range from 5° to 55° in 10° steps. The SZ that was used for the model ranged from 5° to 85° in again 10° intervals. All variables are considered to be uniform within each simulated pixel.

These variables have been combined in all possible combinations. A fire of a given size and temperature within a background of a given temperature can be simulated from these data using a simple, linear combination of the fire and the background radiances:

$$L = L_{fire} \times p + L_{background} \times (1 - p) \tag{4.2}$$

where

$$\begin{aligned} p &= \text{the burning fraction for a pixel} \\ L &= L_{T_f,T_s,r_{7,sx},\phi,VZ,D,p} \\ L_{fire} &= L_{T_f,\phi,VZ,D} \\ L_{background} &= L_{T_s,r_{7,sx},\phi,VZ,D} \end{aligned}$$

4.2.2 Establishment of the Parameters for the smallest detectable Fire

Fire detection based on the 2.1 μm channel faces the problem that, during daytime observations (night time observations by MODIS are currently not available for the 2.1 μm channel), the 2.1 μm region of the electromagnetic spectrum is highly affected by radiation due to reflection of sunlight. If a fire is to be detected using a channel observing this wavelength, it has to produce a high amount of radiation to stand out from the already significantly radiating and reflecting background.

As mentioned in chapter 3, the 2.1 μm channel of MODIS will not be very sensitive to smoldering fires of temperatures ranging from 600 to 800 K but more to those that are flaming at temperatures above 800 K. Kaufman and Justice (1998) based their sensitivity studies on temperatures of 1000 $\pm$ 200 K for flaming fires. It was therefor decided in this study to set the temperature of the prototype for the smallest detectable fire to 900 K, a temperature to which the the 2.1 μm channel is expected to be sensitive but which is also expected to be frequently observed in real world situations.

The attribute more difficult to determine is size. Kaufman and Justice (1998) claim that the 2.1 μm channel will saturate at an effective pixel reflectance of 0.8 which corresponds to a fire burning at a temperature of 1000 K covering a fraction of 0.007 of the 500 m pixel. Observations, however, suggest that in reality the 2.1 μm channel of MODIS saturates at reflectance values of 0.98 which is equivalent to a fire of 1000 K covering a fraction of 0.009 of the pixel within a high reflective background of 0.18 reflectance. A fire of 900 K located within the same background reflectance has to cover an area of 0.0192 of the pixel to saturate the sensor.

The size of the prototype of the smallest detectable fire has to satisfy two conditions. Firstly, it has to be smaller than the size of those fires which saturate the channel and secondly, it has to be big enough to produce enough energy to lift the total apparent reflectance of the pixel containing the fire to well above the reflectance which would be observed without the fire.

Simulations in figures 4.1 (p 55) and 4.2 (p 56) shows, that both conditions are satisfied if the amount of reflectance caused by the burning fraction equals or exceeds the part of reflectance due to the background. The fraction at which these two are equal obviously varies depending on the reflectance of the background. In the case of a higher reflectance background of 0.18, as shown in figure 4.1 (p 55), the reflectances of background and fire are equal at at burning fraction of 0.006. In case of a

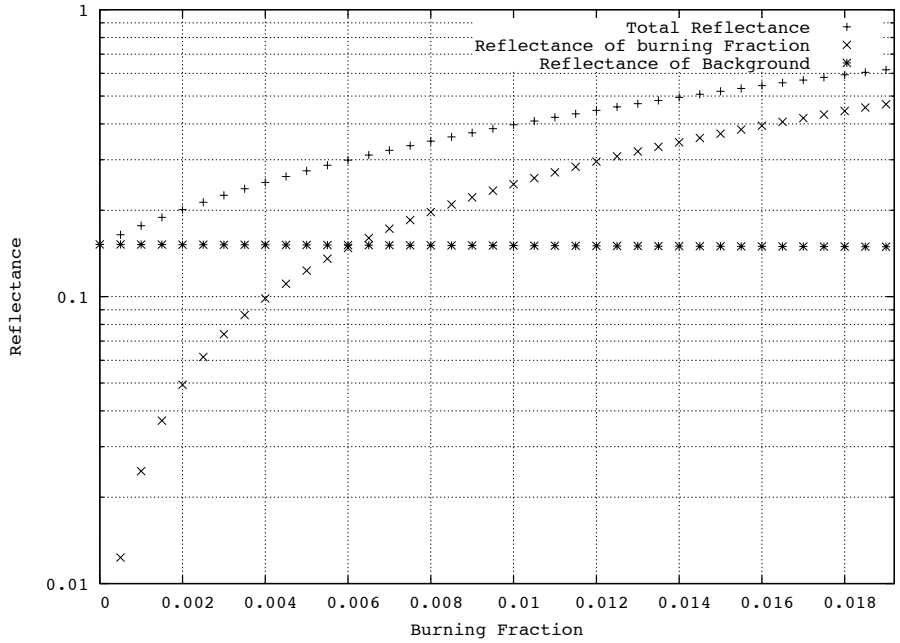

Figure 4.1: Simulated total reflectance and its components of a pixel containing a fire burning at 900 K. The background reflectance is 0.18, VZ and SZ are 25 degrees. The range of the x axis is until a fraction of 0.0192, the fraction size at which a fire of 900 K saturates the 2.1 μm channel

background with a lower reflectance of 0.13, as shown in in figure 4.2 (p 56), the required burning fraction is 0.0045. As a compromise between the burning fractions needed for the fire to match the reflectance caused by low and high reflective background, a pixel fraction value of 0.005 is selected as the required fraction of the prototype of the smallest detectable fire. In the case of the the native resolution of 500 m of the 2.1 μm channel this fraction equals 1250 m^2. In the 2.1 μm channel of MODIS, the smallest detectable fire therefore is a fire which causes reflectance of 0.25. This value is derived by combining a fire of 900 K with a fire fraction of 0.005. The signal-to-noise ratio (SNR) of 110 of channel 7 does not have signifi-

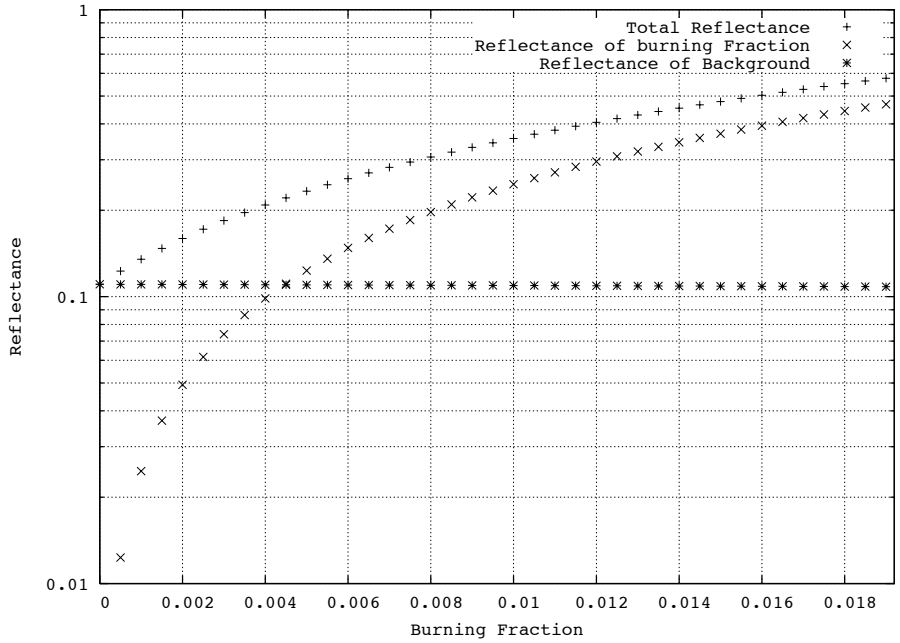

Figure 4.2: Simulated total reflectance and its components of a pixel containing a fire burning at 900 K. The background reflectance is 0.13, VZ and SZ are 25 degrees. The x axis ranges until 0.0192, the fractional fire size (about 4800 m^2) at which a fire of 900 K saturates the 2.1 μm channel.

cant implications. In case of the smallest detectable fire, it only varies the third decimal place of the fire caused reflectance change.

Hence, the smallest detectable fire is identified by each combination of temperature and burning fraction that is consistent with a reflectance of 0.25 in the 2.1 μm channel. Figure 4.3 (p 58) shows the function describing these combinations for fire temperatures between 600 and 1200 K. Sample combinations that satisfy the prerequisite conditions for a smallest detectable fire are given in table 4.2 (p 57).

The influence of the atmosphere at 2.1 μm to the signal measured by

Table 4.2: Sample combinations of fire temperature and size that satisfy the requirements of the smallest detectable fires

Fire Temperature (K)	Burning Fraction	Size (m^2, 500m pixel)
600	0.2141	53525
700	0.0424	10600
800	0.0126	3150
900	0.005	1250
1000	0.0023	575
1100	0.0012	300

the sensor is negligible compared to the radiation caused by ground reflectance or a fire itself. Figure 4.4 (p 59) shows that the radiation due to pixel reflection is one order of magnitude bigger than the radiance contributed by atmospheric scattering. The atmospheric model assumed for in MODTRAN was the US 1976 Standard Atmosphere. It was assumed to be cloud free and not obstructed by smoke.

A similar situation is displayed by figure 4.5 (p 60). Furthermore, it shows the significant rise of surface emission caused by a fire of 1000 K covering a fraction of 0.005 and its impact on the total emitted radiation. This case shows that the effect of atmospheric scattering to the total signal has been further reduced. The atmospheric conditions were assumed the same as before.

4.3 Determination of Background Reflectance and Change

As this fire detection algorithm is based on the change off reflection in the 2.1 μm channel, *a priori* knowledge of the expected reflectance for each pixel is required. This implementation derives this data from a multi temporal bidirectional reflectance distribution function (BRDF) (Roujean

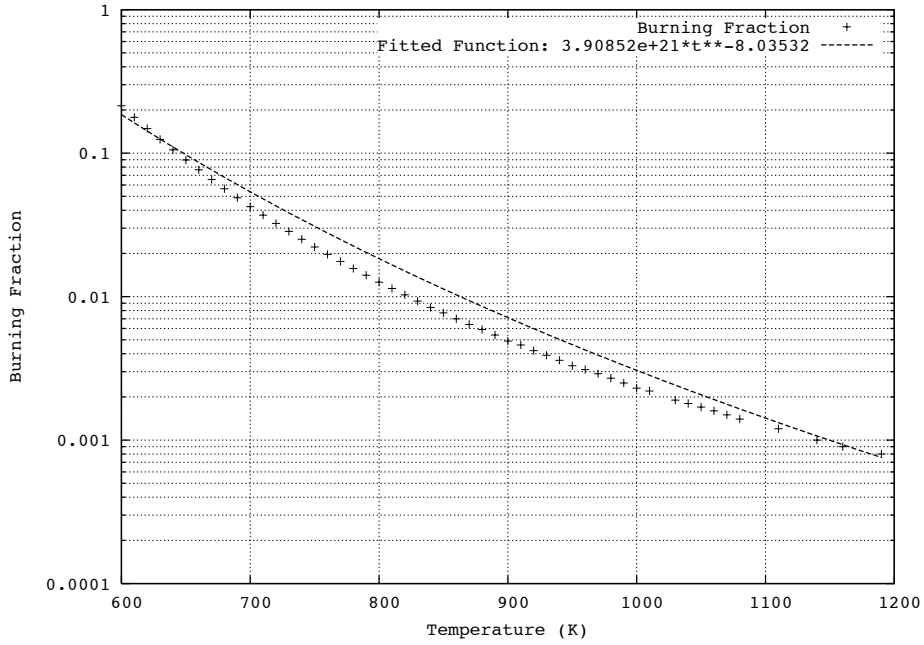

Figure 4.3: Burning fraction required to cause 0.25 reflectance in the 2.1 μm channel of MODIS for a range of fire temperatures. The graphs show the values derived from the simulation (crosses) and a fitted function(solid line).

et al., 1992) model.

The model used in this implementation was developed by Maier (2006). It calculates the expected reflectance for each pixel from previously derived BRDF and atmospherically corrected valid MODIS observations of the same pixel. Pixels are considered valid for use as a previous observation if they are not water, not cloud and contain valid data. A pixel is furthermore not considered as a valid observation if its own modelled value deviates too much from its observed value. This ensures that no undetected, sub-pixel clouds or fires are used. At least 7 valid past observations are required to calculate the expected reflectance for a spe-

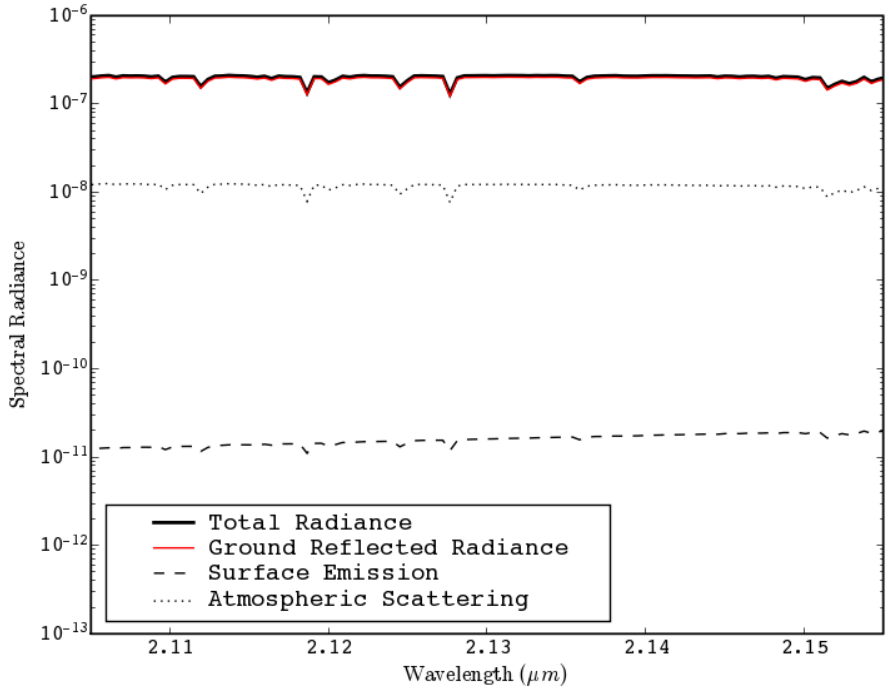

Figure 4.4: Total radiance and its main components at the bandwidth of MODIS channel 7 (2.105 - 2.155 μm). Note that the total radiance and the radiance cause by ground reflectance are almost impossible to distinguish. The simulation specified parameters are: background temperature: 300K, background reflectance: 0.18, VZ: 25° and SZ: 25°

cific pixel. These observations are taken from at least the last 8 and at most the last 21 days. If this temporal window does not give enough valid observations for a pixel, the expected reflectance cannot be determined. In this work the model is run at 250 m resolution for every pass of Terra and Aqua covering Australia. It delivers the atmospherically corrected reflectance (ρ_x), the difference between expected reflectance and observed reflectance (reflectance change, $\Delta\rho_x$). The standard deviation of the differences between the observed and modelled reflectances (σ_{ρ_x}) (as per Maier (2006) procedure) of the past observations used to predict the reflectance are calculated as a measure of the quality of the expected

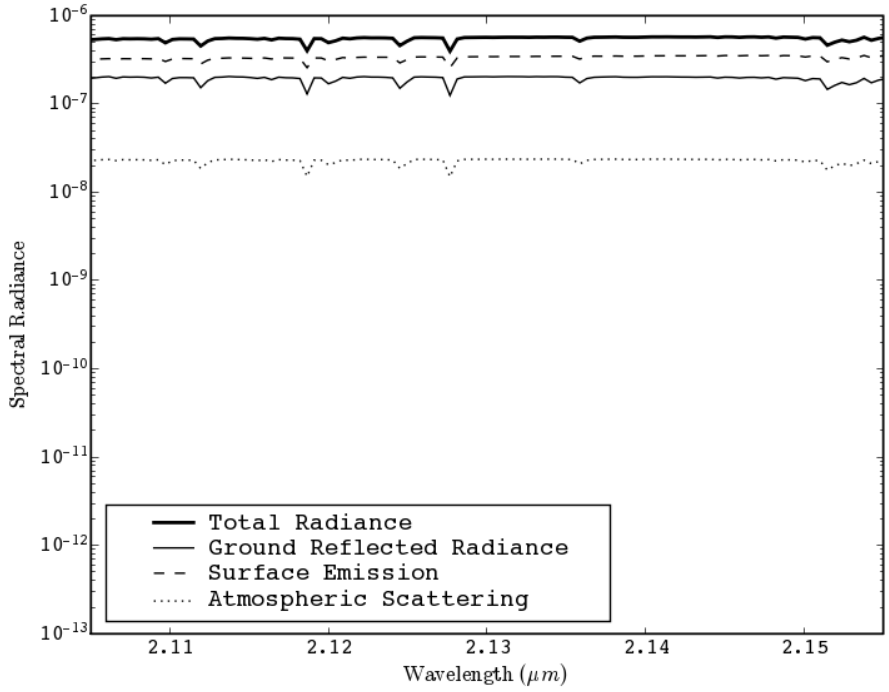

Figure 4.5: Total radiance and its main components at the bandwidth of MODIS channel 7 (2.105 - 2.155 μm). The specified simulation parameters are: fire temperature: 1000 K, burning fraction: 0.005, background temperature: 300K, background reflectance: 0.18, VZ: 25° and SZ: 25°

reflectance. For all values, x is the channel center wavelength.

4.4 Fire Detection Algorithm Components

The algorithm makes use of the strong increase in reflectance of a pixel in the 2.1 μm channel compared to the expected background reflectance (see section in 4.3 and figure 4.6 (p 61)). It looks for a change in reflectance that is at least as large as the reflectance change expected to be caused by the smallest detectable fire as defined in section 4.2. After all potential

fire pixels have been identified, several tests are applied to reject false positive classifications. Table 4.3 (p 62) shows an overview of all channels utilized by the algorithm. If any of these channels is not valid, the pixel is flagged invalid.

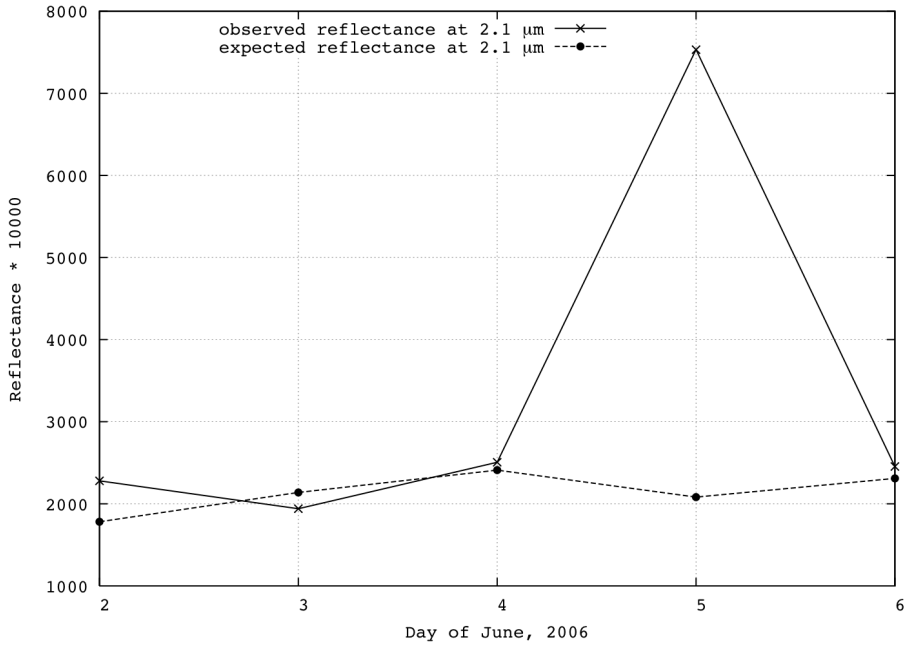

Figure 4.6: Observed reflectance before, during and after a fire and expected non-fire reflectance of the 2.1 μm channel for the pixel at 127.841 east and -20.176 north.

4.4.1 Cloud and Water Masking

Clouds commonly discriminate themselves from the underlying earth surface by their higher reflectance across a large range of the electromagnetic spectrum and lower temperatures Ackerman et al. (1997). If it is not desired to retrieve properties of the observed clouds, algorithms that

Table 4.3: MODIS channels used by the Fire Detection Algorithm

Channel No.	**Centre Wavelength (μm)**	**Objective**	**Notation**
1	0.65	Cloud masking	$\rho_{0.65}$
2	0.86	Cloud masking	$\rho_{0.86}$
3	0.46	Cloud false alarms rejection	$\rho_{0.46}, \Delta\rho_{0.46}$
5	1.24	Cloud false alarms rejection	$\rho_{1.2}$
7	2.1	Active fire detection	$\rho_{2.1}, \Delta\rho_{2.1}, \sigma_{\rho_{2.1}}$
31	11.0	Cloud masking	T_{11}

use simple thresholds in the visible and TIR region of the spectrum work considerably well Ackerman et al. (1997) to detect clouds.

The discrimination between clouds and clear sky conditions was performed using a technique based on the one proposed by Stroppiana et al. (2000) for the AVHRR instruments. Stroppiana et al. (2000) classify a daytime pixel as cloud contaminated if it satisfies:

$$\rho_{0.64} + \rho_{0.86} > 1.2 \tag{4.3}$$

or

$$T_{11} < 265K \tag{4.4}$$

or

$$\begin{cases} \rho_{0.64} + \rho_{0.86} > 0.8 \\ and \\ T_{11} < 285K \end{cases} \tag{4.5}$$

Data from MODIS channel 7 is currently only available for daytime observations. Hence no cloud masking mechanism for nighttime observations is necessary for this work. The cloud mask in this research follows the above cloud masking scheme. The thresholds, however, were adjusted to reflect a more conservative cloud mask in order minimize the number of pixel that contain clouds but are falsely flagged as cloud free. In this work, pixels are flagged as cloud-contaminated if they conform to the condition:

$$\rho_{0.64} + \rho_{0.86} > 0.55 \tag{4.6}$$

$$or$$

$$T_{11} < 275K. \tag{4.7}$$

Water masking is being done indirectly as the procedure by Maier (2006) is only run on land pixels. The values of $\Delta\rho_{2.1}$ and $\Delta\rho_{0.46}$ are only calculated for land pixels and set to an invalid value for water pixels. As the fire detection algorithm only runs on pixels with valid data in $\Delta\rho_{2.1}$ and $\Delta\rho_{0.46}$, water body pixels are ignored. Pixels that are on land but are flooded at the time of the observation are masked out due to the fact that $\Delta\rho_{2.1}$ is negative for these pixels.

4.4.2 Identification of Possible Fire Pixels

All pixels that have not been flagged as being either cloud or water pixels are tested for possibly containing a fire. If they fullfill the conditions:

$$\Delta\rho_{2.1} > 0.25 \tag{4.8}$$

and

$$\frac{\Delta\rho_{2.1}}{\sigma_{\rho_{2.1}}} > 3 \tag{4.9}$$

they are classified as possible fire detections and are subjected to further tests. Otherwise they are flagged as non-fire. The test in equation 4.8 checks if the reflectance change in the 2.1 μm channel of the observed pixel is above the reflectance change expected to be caused by the smallest detectable fire. Equation 4.9 checks if the reflectance change is bigger than three times the standard deviation of the modelled expected reflectance and ensures that the reflectance change was not likely to be caused by normal variations in reflectance.

4.4.3 False Alarm Rejections

Although a cloud mask is applied before any tests off whether a pixel contains a fire are exercised, it is still possible that pixels are contaminated with clouds or other highly reflective objects. These pixels can trigger the fire detection mechanism and cause false alarms. In order to detect pixels where this is the case, one further test is introduced:

$$\rho_{2.1} < \rho_{1.2}. \tag{4.10}$$

Pixels that satisfy this test, are flagged as cloud contaminated not considered valid fire detections.

For a cloud free fire pixel, $\rho_{1.2}$ is expected to be less than $\rho_{2.1}$ as the temperatures and sizes of those fires that the algorithm is able to detect and are expected to be encountered in real world situations are of values that

would not cause $\rho_{1.2}$ to rise due to the influence of the fire. Equation 4.10 tests for pixels for which $\Delta\rho_{2.1}$ is high enough to pass tests 4.8 and 4.9 but which have values of $\rho_{1.2}$ higher than $\rho_{2.1}$. In these cases, the high value of $\Delta\rho_{2.1}$ is more likely to be caused by a highly reflective object within the pixel, like clouds, than by an active fire.

Figure 4.7 (p 66) shows a flowchart of the complete fire detection process.

4.4.4 Detection Confidence

Based on a method suggested by Giglio et al. (2003b), the fire detection confidence determination uses a ramp function defined as:

$$S(x;\alpha,\beta) = \begin{cases} 0; & x \leq \alpha \\ (x-\alpha)/(\beta-\alpha); & \alpha < x < \beta \\ 1; & x > \beta \end{cases} \tag{4.11}$$

where

$$\begin{aligned} x &= \text{the data value} \\ \alpha &= \text{a typical low value} \\ \beta &= \text{a typical high value.} \end{aligned}$$

For each fire detection, the confidence is composed of three sub-confidences tagged C_1, C_2 and C_3. These confidences employ $\Delta\rho_{2.1}$, the number of adjacent cloud pixels (N_{ac}) and the standardized variable $z_{2.1}$ (Weisstein, 2006) defined as:

$$z_{2.1} = \frac{\Delta\rho_{2.1}}{\sigma_{\rho_{2.1}}} \tag{4.12}$$

which represents the number of standard deviations that $\rho_{2.1}$ lies above

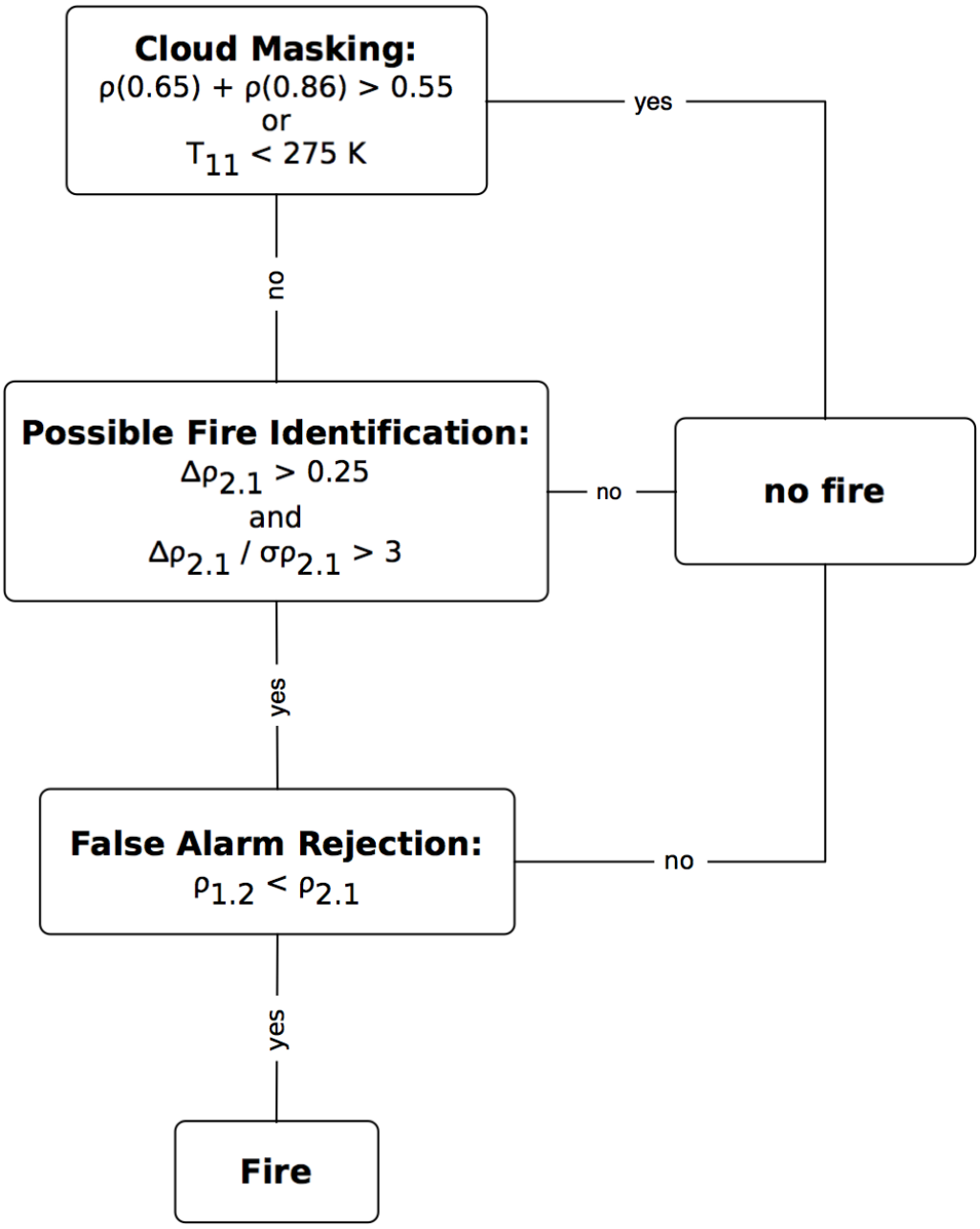

Figure 4.7: Flowchart of the fire detection process based on the 2.1 μm channel of MODIS

its mean reflectance. Each sub-confidence ranges from 0 (lowest confidence) to 1 (highest confidence). they are defined as:

$$C_1 = S(\Delta\rho_{2.1}; 0.25, 0.9) \quad (4.13)$$

$$C_2 = S(z_{2.1}; 3, 18) \quad (4.14)$$

$$C_3 = 1 - S(N_{ac}; 0, 48). \quad (4.15)$$

A value of $C_1 = 0.25$ represents the minimal reflectance change necessary for a pixel to be considered a valid but marginal fire detection. Based on experience, a $\Delta\rho_{2.1}$ value of 0.9 represents a typical value for a mature fire. The same reasoning applies to C_2. Three standard deviations above the mean is the minimum value for the pixel to be considered a fire whereas 18 standard deviations above the mean illustrates a significant fire. C_3 decreases the detection confidence with an increasing number of adjacent cloud pixels within a 7 by 7 pixel window centered around the fire pixel.

Further following the approach by Giglio et al. (2003b), the fire detection confidence C for each pixels is defined as the geometric mean of the three separate sub-confidences:

$$C = \sqrt[3]{C_1 C_2 C_3}. \quad (4.16)$$

C has a value of zero in the case where any of the sub-confidence values is zero.

4.5 Summary

This chapter discussed a fire detection scheme for MODIS based on the 2.1 μm channel and its required input datasets. The proposed algorithms consists of a series of tests which screen for possible active fire, clouds and false positive detections. It further applies a set of fire detection con-

fidence tests to provide user guidance as to the reliability of a particular fire detection.

This proposed fire detection scheme was applied to MODIS data. The following chapter describes the assessment of its performance to MODIS data collected over Western Australian fire regimes.

Chapter 5

Algorithm Performance

Due to the genrally short time that bushfires are stationary, the large area covered by each MODIS scene and very limited available ground data, a an accurate assessment of performance of fire detection algorithms is always very difficult. This chapter attempts to give a preliminary evaluation of how the algorithm based on the 2.1 μm channel of MODIS, as described in the previous chapter, performs. This is done in two different ways. The first step is to compare the fire detection by the proposed algorithm to high resolution (30 m) data from the Advanced Spaceborne Thermal Emission and Reflection Radiometer (ASTER). The second is to compare (i) fire detection by the algorithm based on the 2.1 μm channel, (ii) fire detections by the MOD14 algorithm and (iii) a remotely sensed burnt area product in a region in the northern parts Western Australia over a period of two weeks in August 2006.

5.1 Comparison with ASTER Data

5.1.1 The ASTER Instrument

The Advanced Spaceborne Thermal Emission and Reflection Radiometer (ASTER) shares its platform Terra with the Protoflight Model of MODIS. It is made up from three sub-instruments each operating in different spectral regions (Abrams and Hook, 2002). The Visible and Near-Infrared Sensor (VNIR) has four channels at 15 m resolution ranging from 0.52 to 0.86 μm, the Shortwave Infrared (SWIR) sensor covers the region from 1.6 to 2.43 μm with six channels at 30 m resolution and the Thermal Infrared (TIR) sensor has five channels at 90 m resolution ranging from 8.125 to 11.65 μm. The VNIR sensor has three and SWIR sensor has four different gain settings (Abrams and Hook, 2002). ASTER has a swath width of 63 km and repetition rate of 16 days (Jacob et al., 2004). The repeat cycle implies that it is not useful for fire monitoring but it is potentially beneficial for validation purposes.

As ASTER shares the platform with one of the MODIS instruments, the two instruments have coincidental nadir observations. This makes ASTER the ideal high resolution instrument for the validation of MODIS active fire algorithms as fires can change significantly within a very short time frame (Morisette et al., 2005).

The ASTER channel most useful for the comparison of the "true" location of active fires and those detected by a MODIS based fire detection algorithm is the 2.4 μm channel 9 ranging from 2.360-2.430 μm. The saturation radiance of this channels is either 4.02, 8.04, 10.72 or 67 $W\mu\mathrm{m}^{-1}sr^{-1}m^{-2}$, depending on the chosen gain setting. Although this channel does not cover the range of the spectrum in which cooler fires have their highest emission, even a small fire can cover a significant fraction of the pixel due to the high spatial resolution and thus will raise the pixels radiance substantially - enough to distinguish between a fire pixel and the back-

ground (Morisette et al., 2005).

5.1.2 ASTER scene selection

Although MODIS covers the same area as ASTER at nadir, there are only a few ASTER scenes available for Australia, that contain active fires. This is due to the their small footprint, long temporal repeat cycle and the fact that ASTER data is not being acquired continuously but only by request (Abrams and Hook, 2002).

For the time between January 2004 and June 2006 only two ASTER scenes, shown in figures 5.1 and 5.2 on pages 72 and 73 over Australia that contained active fires were found. Both were from the 13th of October, 2004 and were obtained at normal gain settings corresponding to a saturation radiance of 8.04 $W\mu\mathrm{m}^{-1}sr^{-1}m^{-2}$.

The radiance values of both scenes have been calculated from digital counts of the ASTER level 1b product using the conversion coefficients provided within the level 1b product. They have been corrected for the geolocation errors as described in ASTER Science Team (2005).

Both ASTER scenes fall within the same MODIS granule. Figure 5.3 (p 74) shows the location of the MODIS and the two ASTER scenes.

ASTER scene one, the more northerly area, shown in figure 5.1 (p 72), is located on the edge of the Central Arnhem region. This area is characterized by open forest and woodland with a grass understorey (Thackway and Cresswell, 1995). Apart from several smaller fire fronts, scene one contains one very intense fire complex that is accompanied by heavy smoke and a water droplet cloud. Scene two, the more southerly area, shown in figure 5.2 (p 73), is located on the Stuart Plateau that vegetation consists of woodland with spinifex understory (Thackway and Cresswell, 1995). The scene is cloud free and contains two low intensity fire

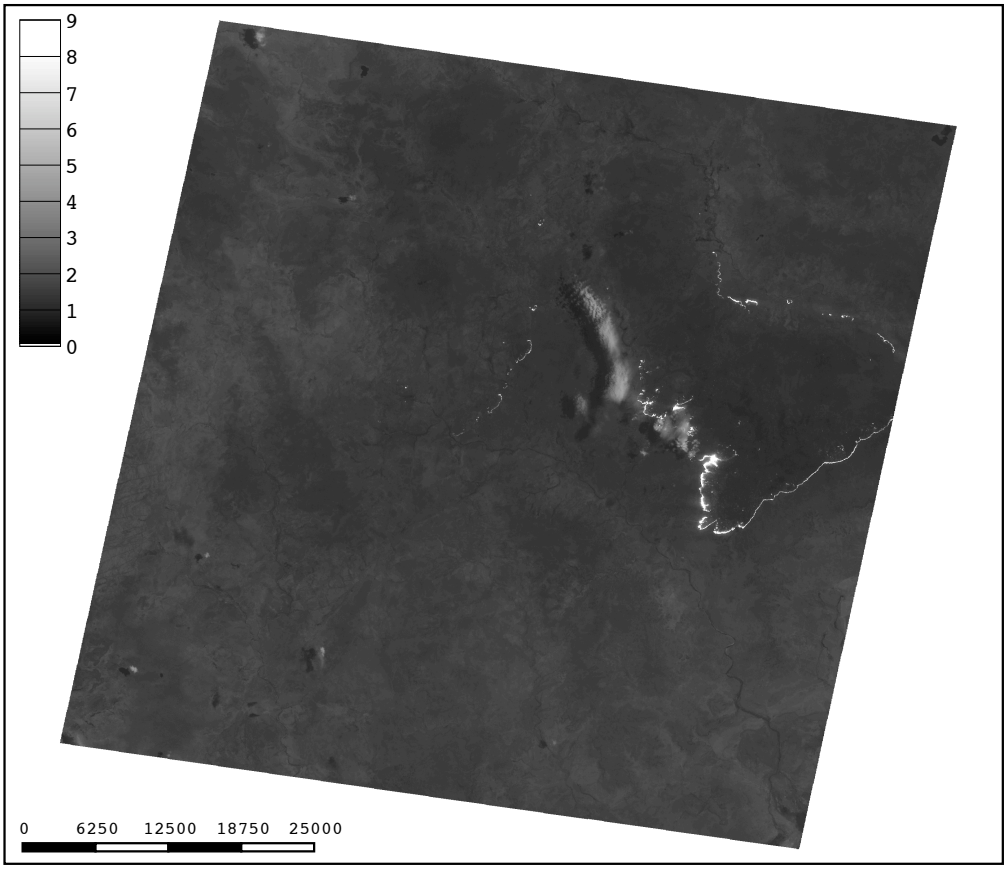

Figure 5.1: Channel 9 of the first ASTER scene from October 13th, 2004. The legend values are in $W\mu\mathrm{m}^{-1}sr^{-1}m^{-2}$. The fire fronts are shown as very bright contiguous features; clouds as light grey areas.

fronts. One front runs diagonally through the scene and a smaller front is located in its south-west corner.

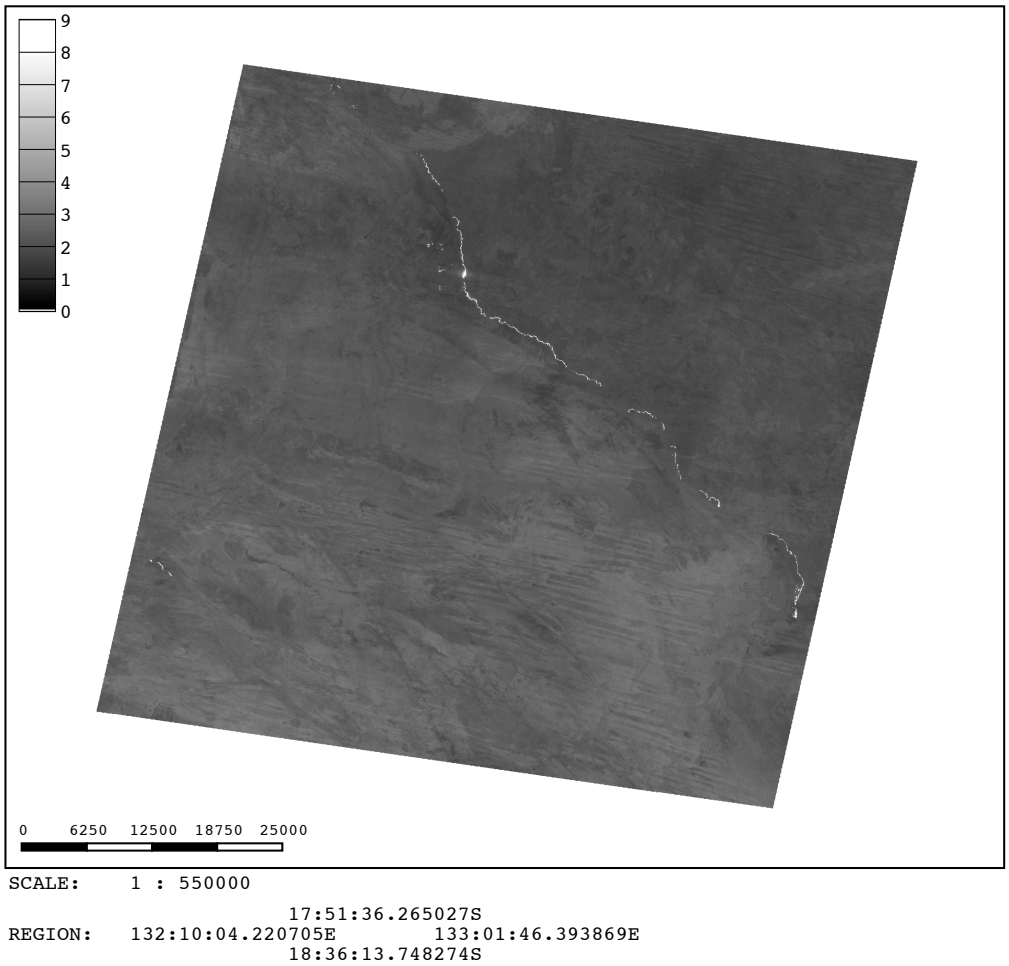

Figure 5.2: Channel 9 of the second ASTER scene from October 13th, 2004. The legend values are in $W\mu\mathrm{m}^{-1}sr^{-1}m^{-2}$. The fire fronts are shown as bright contiguous features.

5.1.3 ASTER Fire Masking

In order to compare the results of the fire detection based on MODIS' 2.1 μm channel to the "true" location of the fire as shown in the ASTER scenes, a 1-bit fire/non-fire mask was produced for each of the two ASTER scenes.

Following the approach taken by Morisette et al. (2005), ASTER pixels

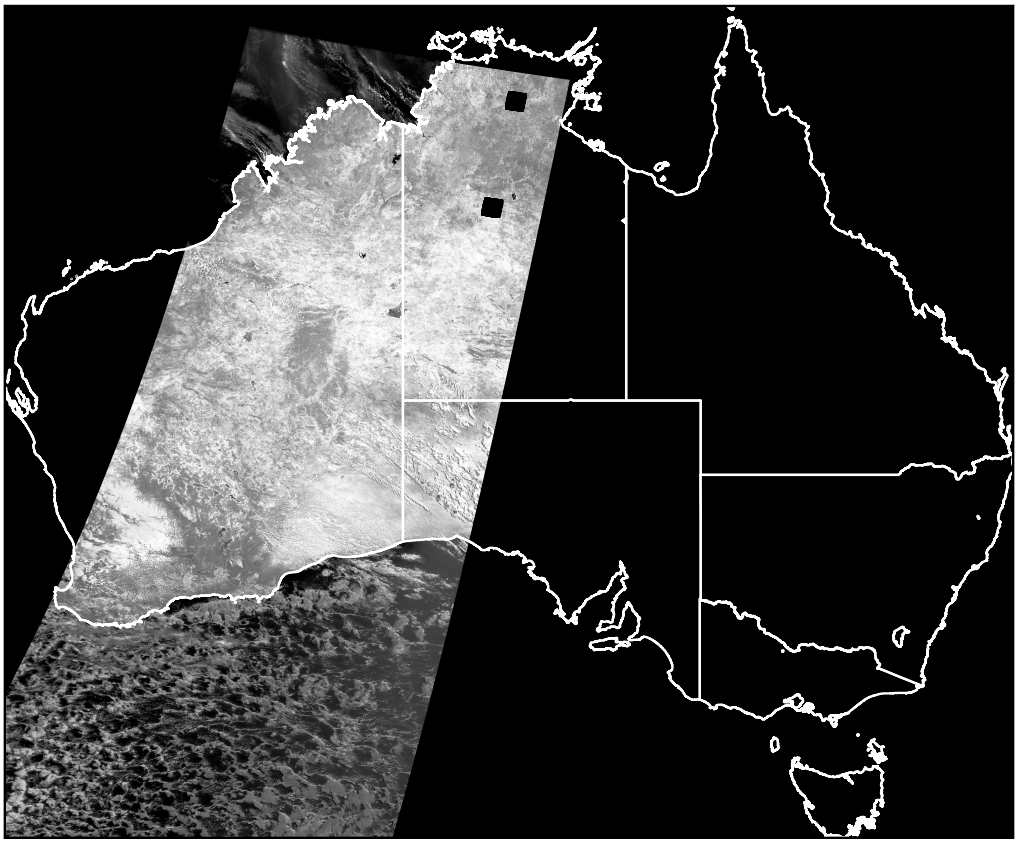

Figure 5.3: The MODIS and ASTER scenes used for the comparison and their location within Australia. The image shown is the radiance of MODIS' 2.1 μm channel, the two black areas within the MODIS scene are the coverage of the two ASTER scenes.

were classified as fire pixels if they satisfy

$$L_{2.4} > 6.33 \tag{5.1}$$

with $L_{2.4}$ being the radiance of the 2.4 μm channel. The resulting fire masks have been visually inspected to avoid falsely classifying cloud pix-

els as fires.

5.1.4 Determination of the Number of ASTER Fire Pixels within each MODIS Pixel

In order to compare the ASTER fire detections with the fire detections from the MODIS 2.1 μm channel data, both datasets have to be collocated. This was achieved with the help of the geolocation information provided with the datasets and the Geographic Resource Analyses Support System (GRASS) (GRASS Development Team, 2005) to which the author of this work used to contribute (GRASS Development Team, 2006).

Furthermore, the triangular response of MODIS and the corresponding 50% overlap to both sides in along-scan direction (Morisette et al., 2005) have to be taken into account. The consequence of this overlap is, that one ASTER fire pixel can fall into two neighboring MODIS pixels and thus be detected twice. To account for this effect when comparing the ASTER and MODIS fire detections, the MODIS fire pixels were assumed (i) to be rectangles of 1 km in along-scan and 500 m in along-track in size in case of the fire detections based on the 2.1 μm channel and (ii) rectangles of 2 km in along-scan and 1 km in along-track direction in case of the MOD14 fire detection. MODIS weights the radiance towards the edge of the pixel in along-scan direction less than the radiance in the center. Thus, a fire at the edges can be missed but not of a fault a fault in the algorithm (Morisette et al., 2005). Following the argument of Morisette et al. (2005), the ASTER fire pixels that fall within one MODIS pixel have not been weighted by their distance to compensate for those possible missing detections as the performance of a fire detection algorithm is influenced by both, the algorithm and the instrument.

The count of the number of ASTER fire detections within each MODIS pixel was based on the center coordinates of the pixels. In the case of the

ASTER pixels, GRASS was used to create a shapefile (ESRI, 1998) containing point features representing the center coordinates of the ASTER fire detections. The same was done with the MODIS fire detections using the algorithm based on the 2.1 μm channel and the MOD14 algorithm as well as those pixels that were not classified as containing a fire. These point features were afterwards transformed into rectangular polygon features of the sizes given above by software using the GDAL/OGR libraries (Wamerdam, 2006) written by the author of this thesis. The calculation of the number of ASTER pixels (or more precisely pixel center points) that fall within each of the polygons representing the area that contributes radiance to each MODIS pixels was again performed by custom software. The ASTER fire pixels were considered to be completely filled by the fire. As this does probably does not hold true in reality, in which it is more likely that only a fraction of each ASTER fire pixel is affected by the fire at the time of the observation. Accordingly, it is not possible to give a good estimate of the burning fraction within each MODIS pixel based on the number of ASTER fire pixels within it. The count methodology does furthermore not compensate for possible errors in the geolocation precision of the instruments.

5.1.5 Comparison of ASTER and MODIS Fire Detections

As a result of the properties of the proposed fire detection algorithm and the characteristics of the fires present in the two available ASTER scenes, the performance of the algorithm based on the 2.1 μm channel differs greatly between the two scenes.

The 2.1 μm algorithm performed very well and as expected for scene one with its big and intense fire complex. It resulted in only two MODIS false positive detections that did not correspond to any ASTER fire pixel. However, one of these false alarms was outside the coverage of the ASTER scene and thus has to be ignored. The other false positive is not close

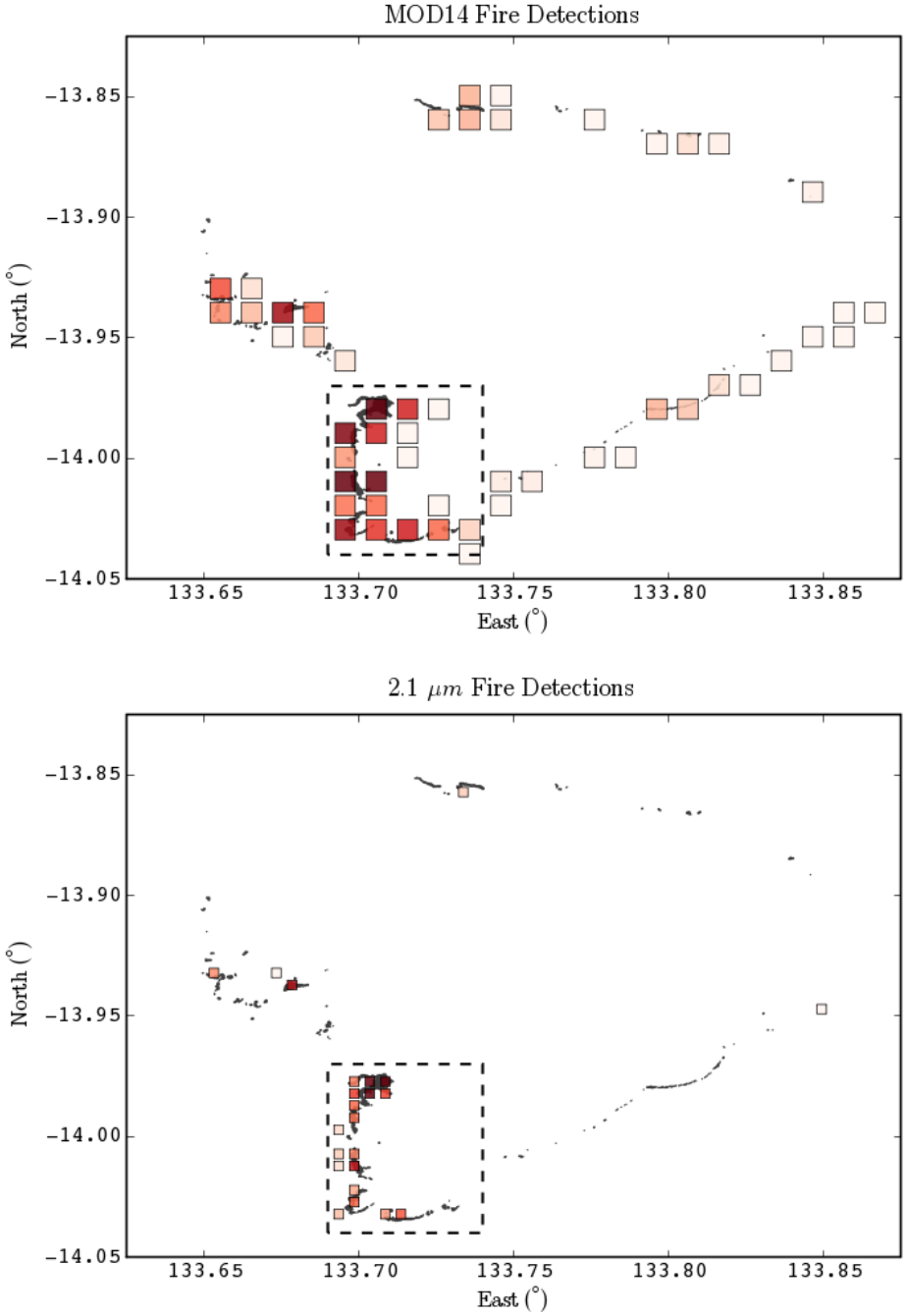

Figure 5.4: Comparison of the fire detections of MOD14 and the proposed MODIS algorithm for ASTER scene one. The ASTER fire pixels are shown in the background. Their number within each MODIS pixel is indicated by the intensity of its color (the squares do not represent the real pixel dimensions). The dashed boxes indicate the area shown in figure 5.5 (p 78).

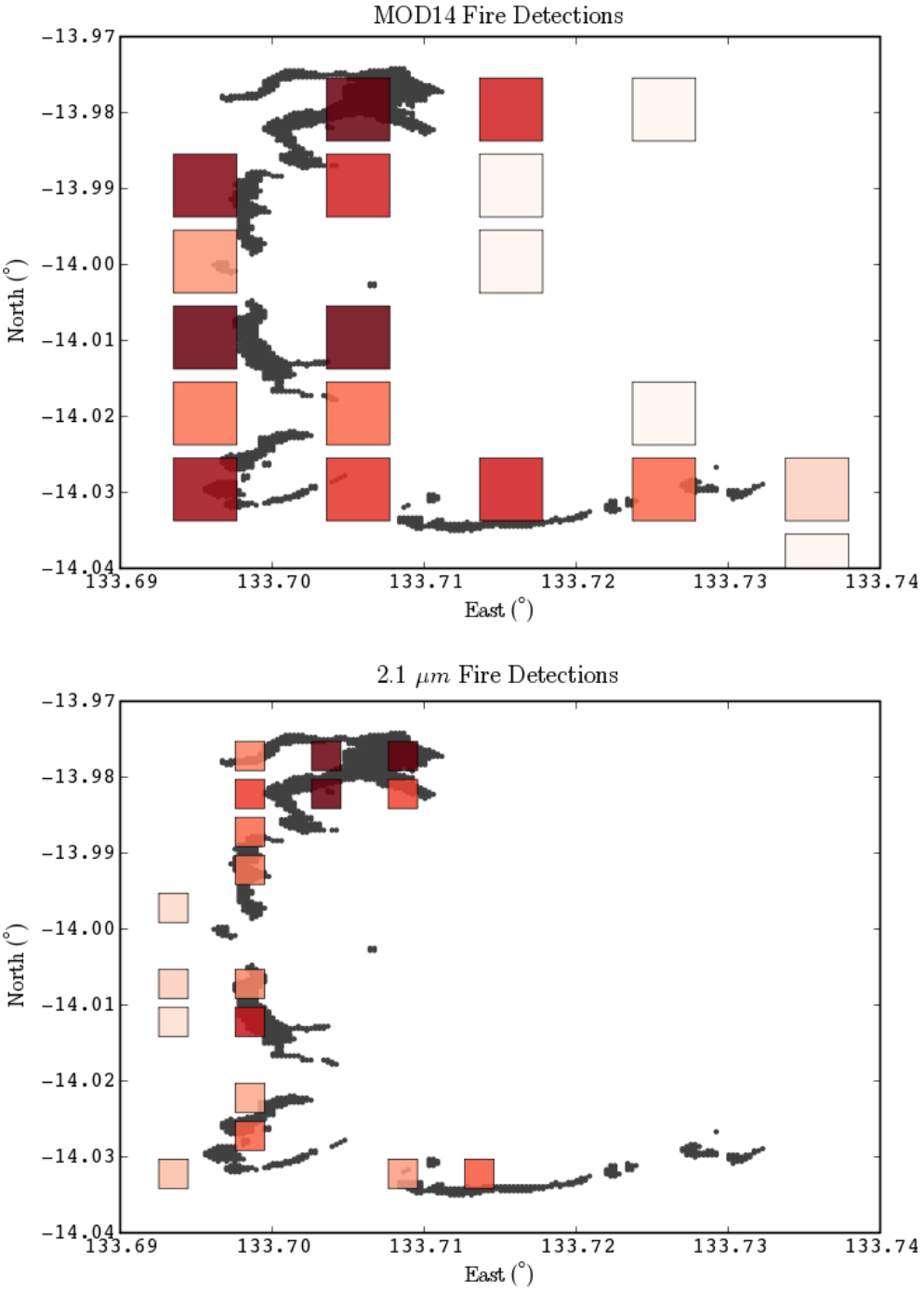

Figure 5.5: Detailed view of the area indicated in figure 5.4 (p 77).

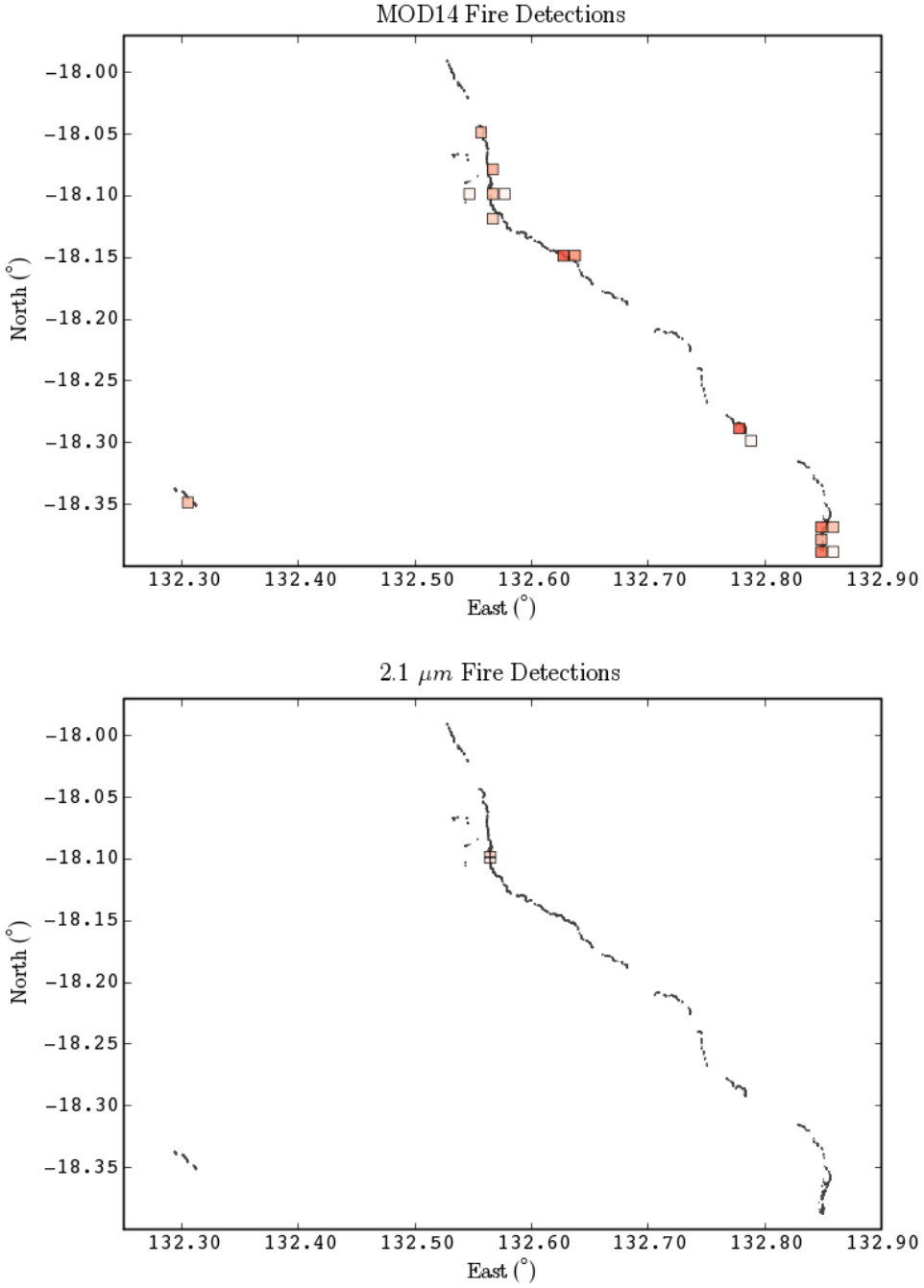

Figure 5.6: Comparison of the fire detections of MOD14 and the proposed algorithm for ASTER scene two. The ASTER fire pixels are shown in the background. Their number within each MODIS pixel is indicated by the intensity of its color. The squares do not represent the real pixel dimensions.

enough to any ASTER fire detection to be caused by geolocation discrepancies and has to be assumed a real false positive. MOD14 had 13 false positives. Both algorithms had a number of false negatives (a false negative is a pixel not classified as fire that in fact does contain an active fire). The MOD14 algorithm had less false negatives (40) than the algorithm based on the 2.1 μm channel (154). This is expected as MOD14 is much more sensitive to less intense fires. As shown in figure 5.7 (p 81) for the 2.1 μm channel algorithm and in figure 5.8 (p 82) for MOD14, the average number of ASTER pixels that fall within the false negative detections is very similar for both algorithms (18 for MOD14, 19 for the 2.1 μm channel algorithm). On average, the 2.1 μm channel algorithm was able to correctly detect fires if 113 ASTER (figure 5.7 ,p 81) fire pixels fell within the 500 m MODIS pixel. The number of ASTER fire pixel counts for correct detections has a high standard deviation of 84. This indicates that the characteristics of the fires that the algorithm is able to detect cover a wide range fire temperature and size combinations. According to the properties of the smallest detectable fire, this behavior is expected. MOD14 behaves in a similar manner (figure 5.8 ,p 82), showing an even greater variability and the expected higher sensitivity.

The 2.1 μm channel algorithm performs not nearly as well on the much less intense fire front in ASTER scene two. It does not suffer from any false positives but only has four correct detections and 206 false negatives. However, the average ASTER fire pixel count of 22 per MODIS pixel (figure 5.9 ,p 84) for those false negative detections indicates that the fires present in this scene simply were not intense enough to meet the requirements of the smallest detectable fire. This is supported by the fact that the average ASTER fire pixel count for all MODIS pixels together is only 22, which is almost the same as the average number of ASTER fire counts for the false negatives. In contrast, the total average number of ASTER fire counts of scene one is 30 compared to 19, the average number of ASTER fire counts of the false negatives in scene one. MOD14 performed better under the conditions of scene two. It showed three false

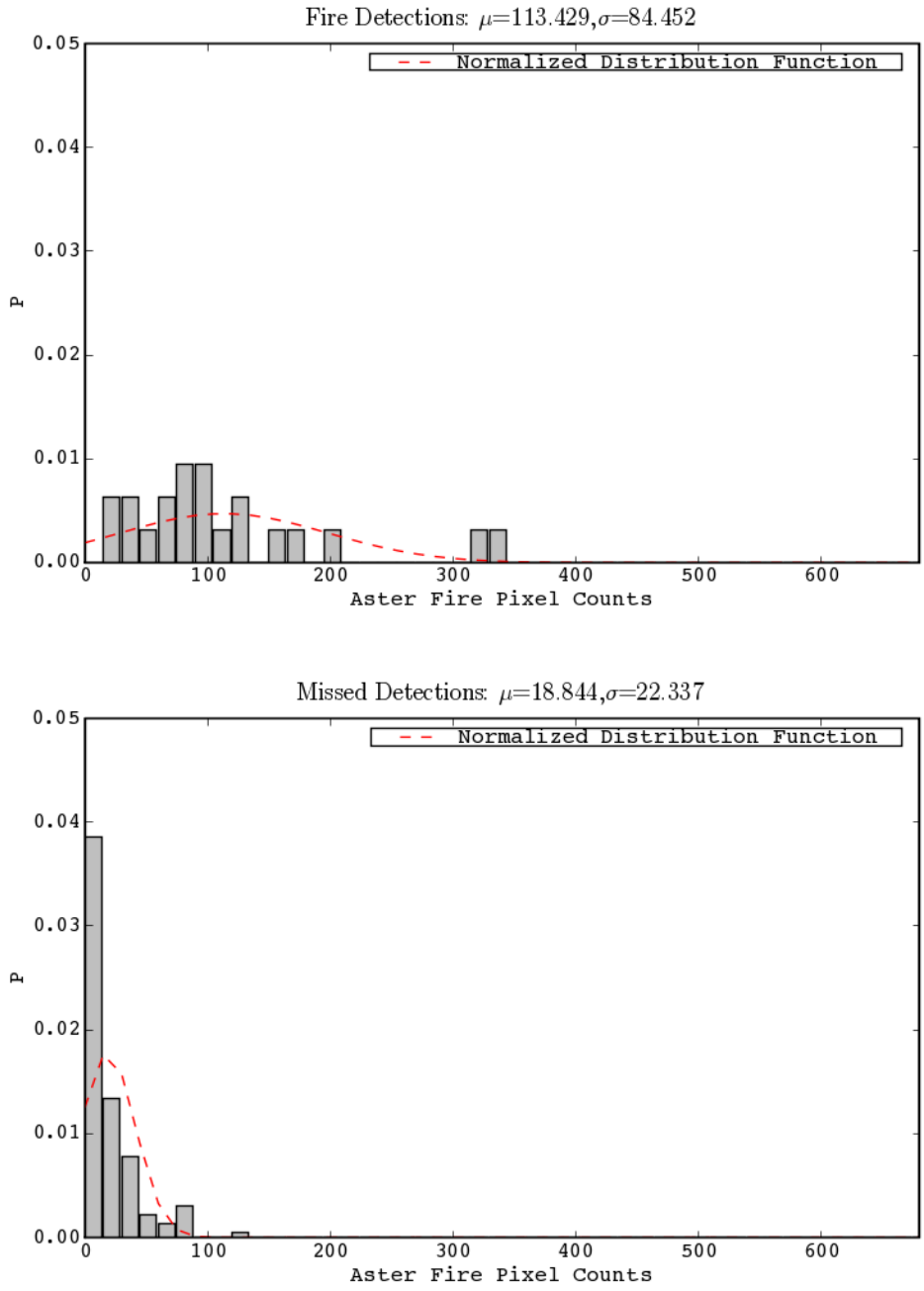

Figure 5.7: Histograms of ASTER fire pixel counts per MODIS pixel for the fire detection scheme based on the 2.1 μm channel for ASTER scene one. The top plot shows the histogram of the MODIS pixels that where flagged as fire pixels. The lower plot shows the histogram of the MODIS pixels for which no active fire was detected but in fact do contain ASTER fire pixels.

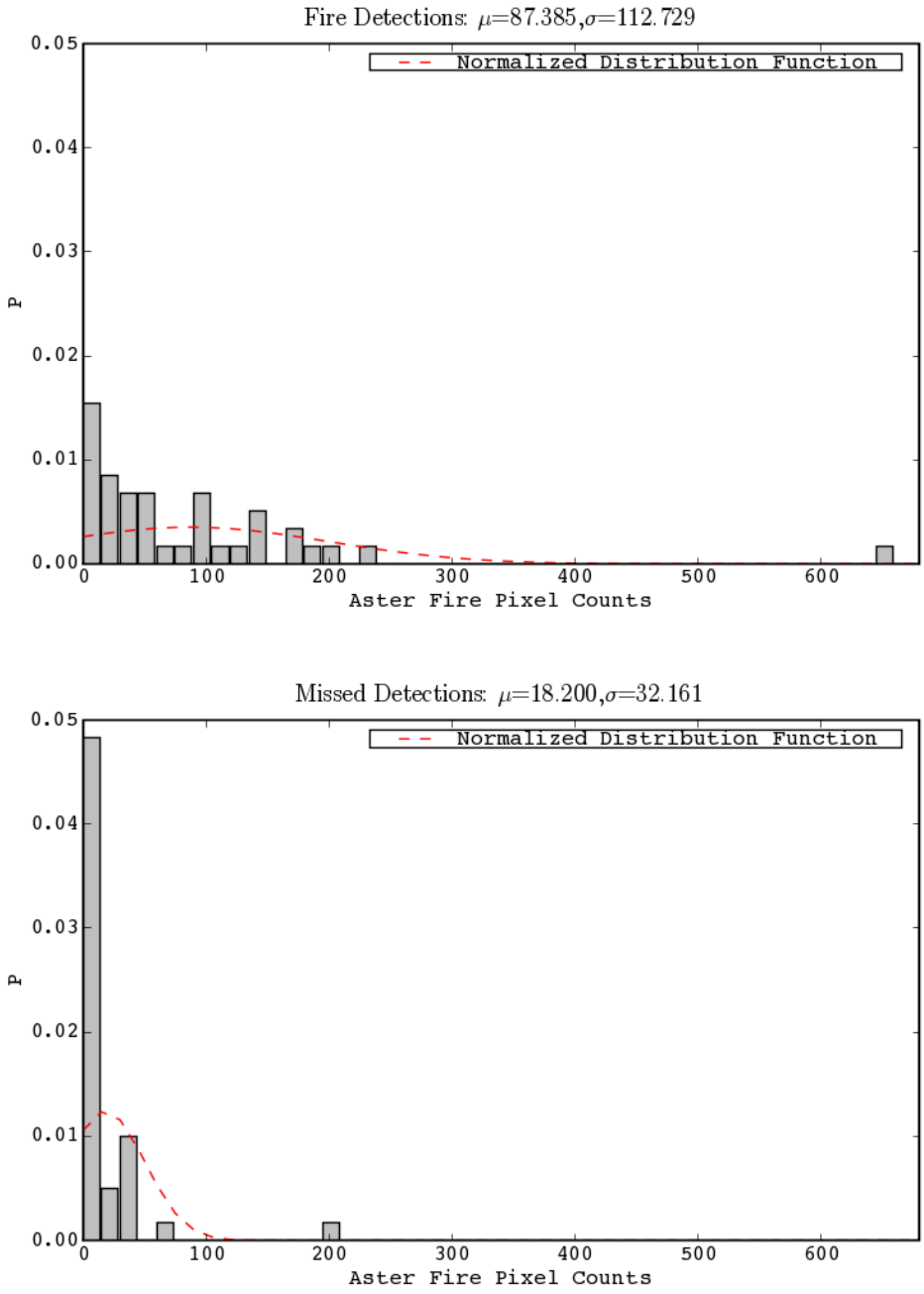

Figure 5.8: Histograms of ASTER fire pixel counts per MODIS pixel of fires detected by MOD14 for ASTER scene one. The top plot shows the histogram of the MODIS pixels that where flagged as fire pixels. The lower plot shows the histogram of the MODIS pixels for which no active fire was detected but in fact do contain ASTER fire pixels.

positives, 76 false negatives and detected 13 fires correctly. The increase in the average number of ASTER fire counts for the false negatives (34, figure 5.10 ,p 85) compared to scene one further indicates that the fire in scene two is of much less intensity.

The proposed algorithm and MOD14 have very different detection characteristics and the proposed algorithm is not meant as an replacement but an addition to MOD14 and other currently used fire detection algorithms for MODIS. Accordingly, it is important to also consider the spatial information given by the algorithms. Figures 5.4 to 5.6 show the spatial aspect of the performance of both algorithms. Figure 5.6 (p 79) is not of great importance as the proposed algorithm could only classify four fire pixels due to the lack of fire intensity. The fire complex of scene one shown in figures 5.4 and 5.5 (p 77, 78) illustrates how the proposed algorithm is capable of 'fine-tuning' the spatial information for large fire complexes by providing a more precise 'shape' of the complex compared with what MOD14 is able to do.

5.2 Comparison with MOD14 and Burnt Area Maps

5.2.1 Study Area

The area chosen for this case study is in the northern parts of Western Australia. It stretches along the Great Northern Highway between Broome and Derby. In August of 2006, this area was affected by a huge fire burning moving through a large area over the course of several days. A number of cloud free observations is available for this time period. In this study, observations from both, MODIS on Terra and Aqua from August 15 to August 31 are used for this comparison. The vegetation in this area is described as consisting of grasslands with low forests and tree

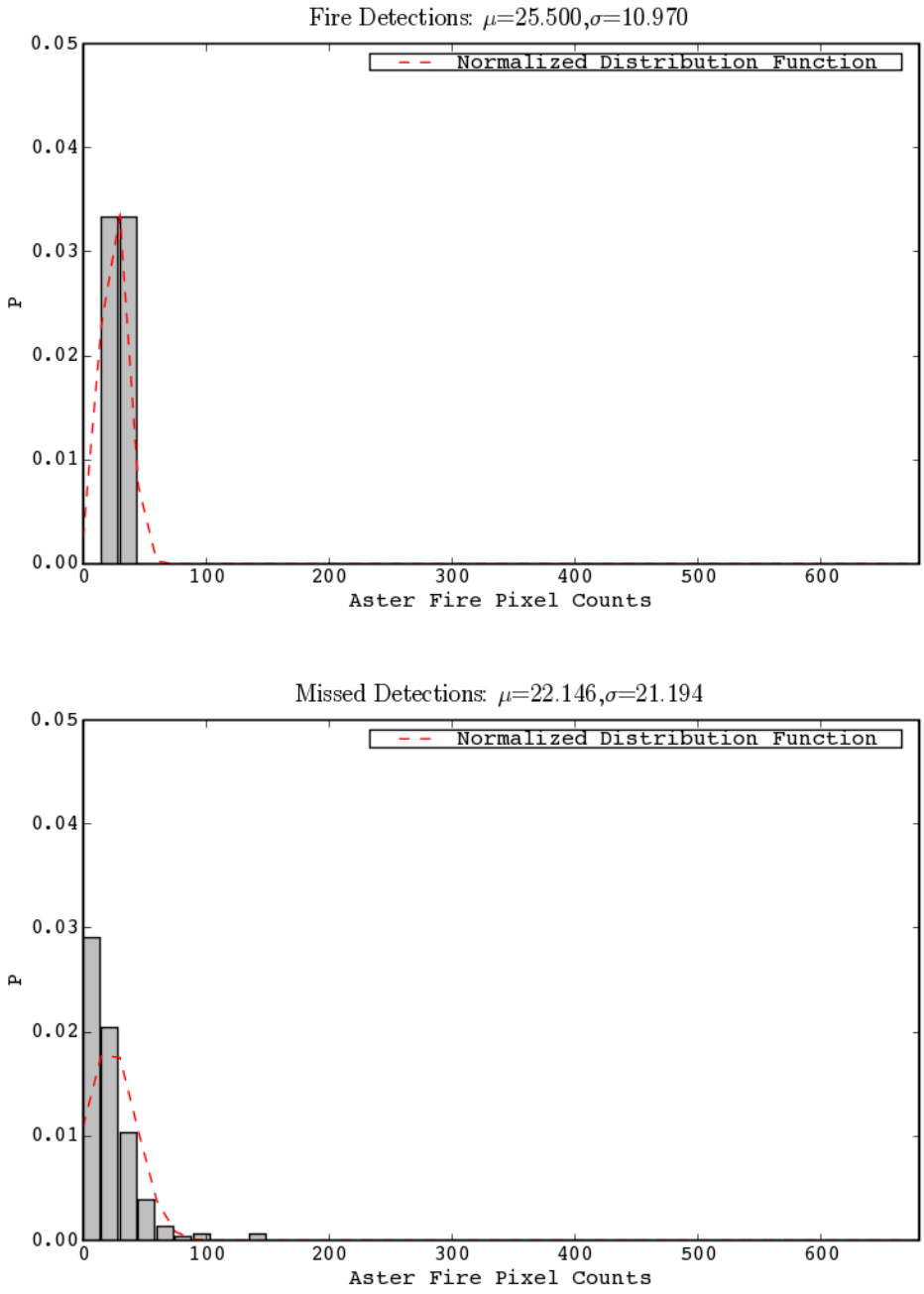

Figure 5.9: Histograms of ASTER fire pixel counts per MODIS pixel for the fire detection scheme based on the 2.1 μm channel for ASTER scene two. The top plot shows the histogram of the MODIS pixels that where flagged as fire pixels. The lower plot shows the histogram of the MODIS pixels for which no active fire was detected but in fact do contain ASTER fire pixels.

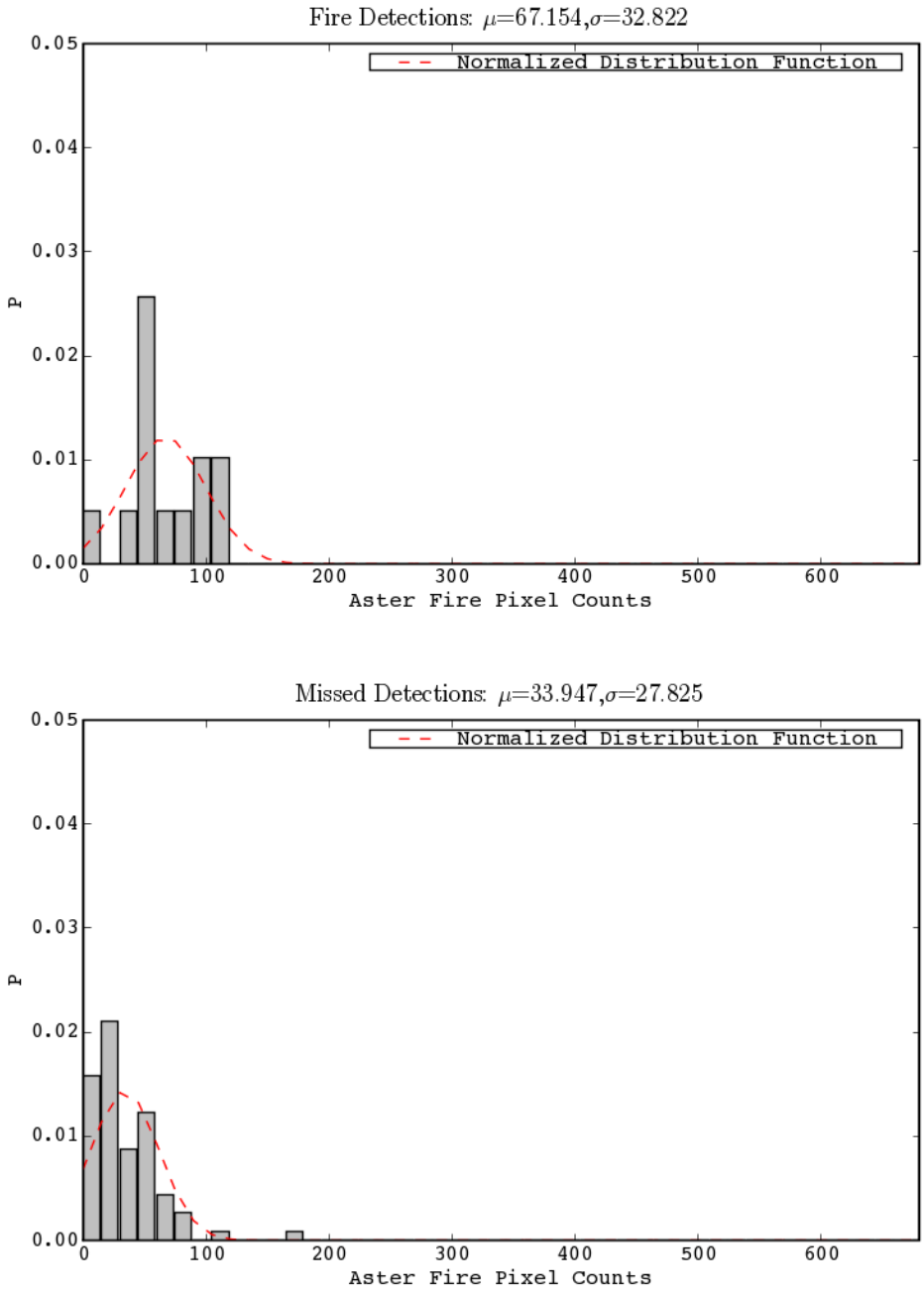

Figure 5.10: Histograms of ASTER fire pixel counts per MODIS pixel of fires detected by MOD14 for ASTER scene two. The top plot shows the histogram of the MODIS pixels that where flagged as fire pixels. The lower plot shows the histogram of the MODIS pixels for which no active fire was detected but in fact do contain ASTER fire pixels.

savannas (Thackway and Cresswell, 1995).

5.2.2 Datasets

Three datasets have been used in this study. The MODIS observations that the fire detection algorithm based on the 2.1 μm channel has been applied to are not single overpasses but daily composites for each of MODIS' platforms. This composites are produced by the Satellite Remote Sensing Services (SRSS) of the Department of Land Information (DLI) of Western Australia. As described by Maier (personal communication), these composites consist of all valid observations of each day and MODIS platform. If the same location had two or more observation in one day, the observation with the smallest off nadir view angle is used.

The MOD14 fire detections based on the 2.1 μm channel are being compared to are available for every overpass. In order to match the daily frequency of the MODIS observations used to generate the fire detection with the proposed algorithm, the MOD14 fire detections of each day and MODIS platform have been composited into one dataset.

The third dataset is a weekly burnt area product updated every overpass, aggregated to one month. The algorithm to detect burnt areas uses the same reflectance change dataset as the proposed fire detection algorithm. It exploits the fact that burnt areas show a strong negative reflectance change (observed reflectance much lower than expected reflectance) in the 0.85 μm channel of MODIS (Maier, 2006).

5.2.3 Determination of correlation between fire detections by the proposed algorithm and MOD14 and the Burnt Area product

In order to determine how the proposed algorithm performs in comparison with MOD14 and the burnt area product, it has to be identified how many of the fire detections by the algorithm based on the 2.1 μm channel correspond to either (i) a fire detection by MOD14, (ii) fall within an area that is classified as burnt or (iii) both.

The burnt area product was available from DLI as a shapefile containing polygons representing the burnt areas. As before, during the comparison with ASTER data, GRASS was used to create a shapefile containing points representing the center points of each pixel classified as fire by the 2.1 μm channel fire detection algorithm for each day and platform. The MOD14 fire detections are available as shapefiles containing points at the center coordinates of the pixels classified as fires. The shapefiles containing the daytime observations of one day and one platform were combined using custom software based on GDAL/OGR to obtain one file for each day and platform.

After the preliminary processing, a total number of five datasets were available for each day. The burnt areas, the MOD14 fire detections of Terra, those of Aqua, the fire detections of the proposed algorithm of both, Terra and Aqua. These five files were the input to the software determining the correlation between the detections. The software based on GDAL/OGR identifies if each fire detection by the proposed algorithm falls with in the burnt area or within the area defined by a rectangular buffer of 1600 m by 1100 in size around each MOD14 fire detection. The size of the buffer is determined by the size of the MODIS pixels used by MOD14 plus a 50 m buffer to account for possible geolocation discrepancies. The output of this software is two files for each day, one for each platform. These files contain five pieces of information on each fire de-

tection by 2.1 μm channel based algorithm. These are the detections latitude, longitude, detection confidence, if it corresponds with a MOD14 fire detection and if it falls within the burnt area.

5.2.4 Comparison of fire detections by the proposed algorithm with MOD14 and the Burnt Area product

As shown in figure 5.11 (p 89) , the fire detections by the proposed algorithm correspond well with the burnt area product and the fire detections by MOD14. The highest number of detections that do not correspond with either of the two chemes appears on August 31 for both, Aqua and Terra, observations with a number of detections of 118 and 42 respectively.

Although these are encouraging numbers, the 2.1 μm channel based algorithm, over all days and both platforms, consistently detects a high number of fires that do not correspond to MOD14 active fire detections (figure 5.12, p 90). For the Terra observations on August 16, 18, 28 and 29, the fire detections do not correspond to any MOD14 detection. However, only two on each of August 16 and 18 and four on each of August 28 and 29 do not fall within the burnt area (figure 5.13, 91). Figures 5.12 and 5.13 (p 90 and 91) show that the pattern of very high correlation between the fire detection of the proposed algorithm and the burnt area and a much lower correlation between the MOD14 fire detections and the proposed algorithm applies to both platforms and all days.

The question as to which detections of the proposed algorithm correspond well with the MOD14 detections and which do not, does not seem to be random but to follow a pattern. Figures 5.14 and 5.15 (p 93 and 94) show the average fire detection confidence of the fire detections that correspond with MOD14 detections and those that correspond with burnt areas for Aqua and Terra. These figures further show the number of de-

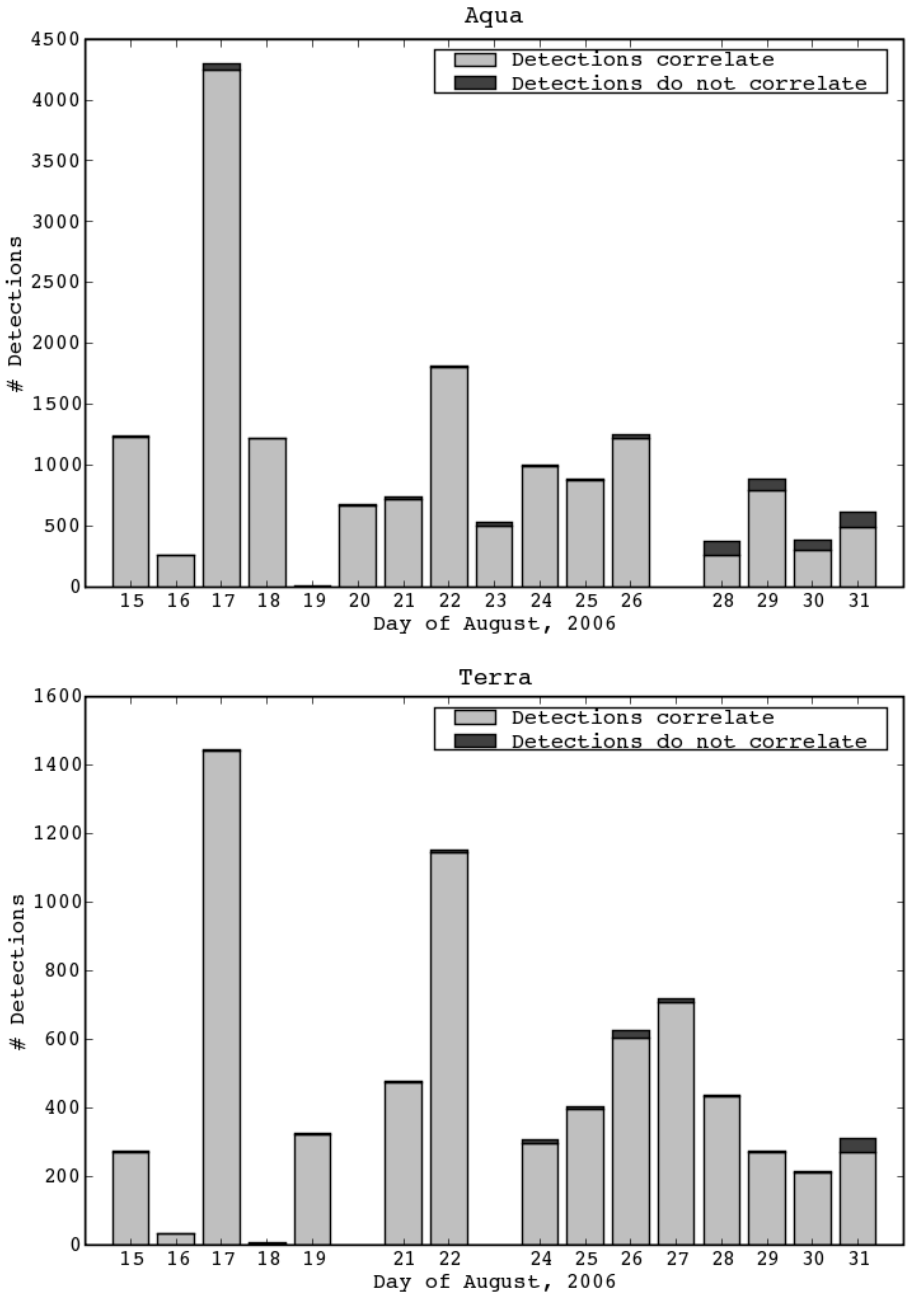

Figure 5.11: Number of fire detection by the 2.1 μm method that correlate with either the MOD14 active fire product or the burnt area mapping and number of those fire detections that correspond with neither of the two.

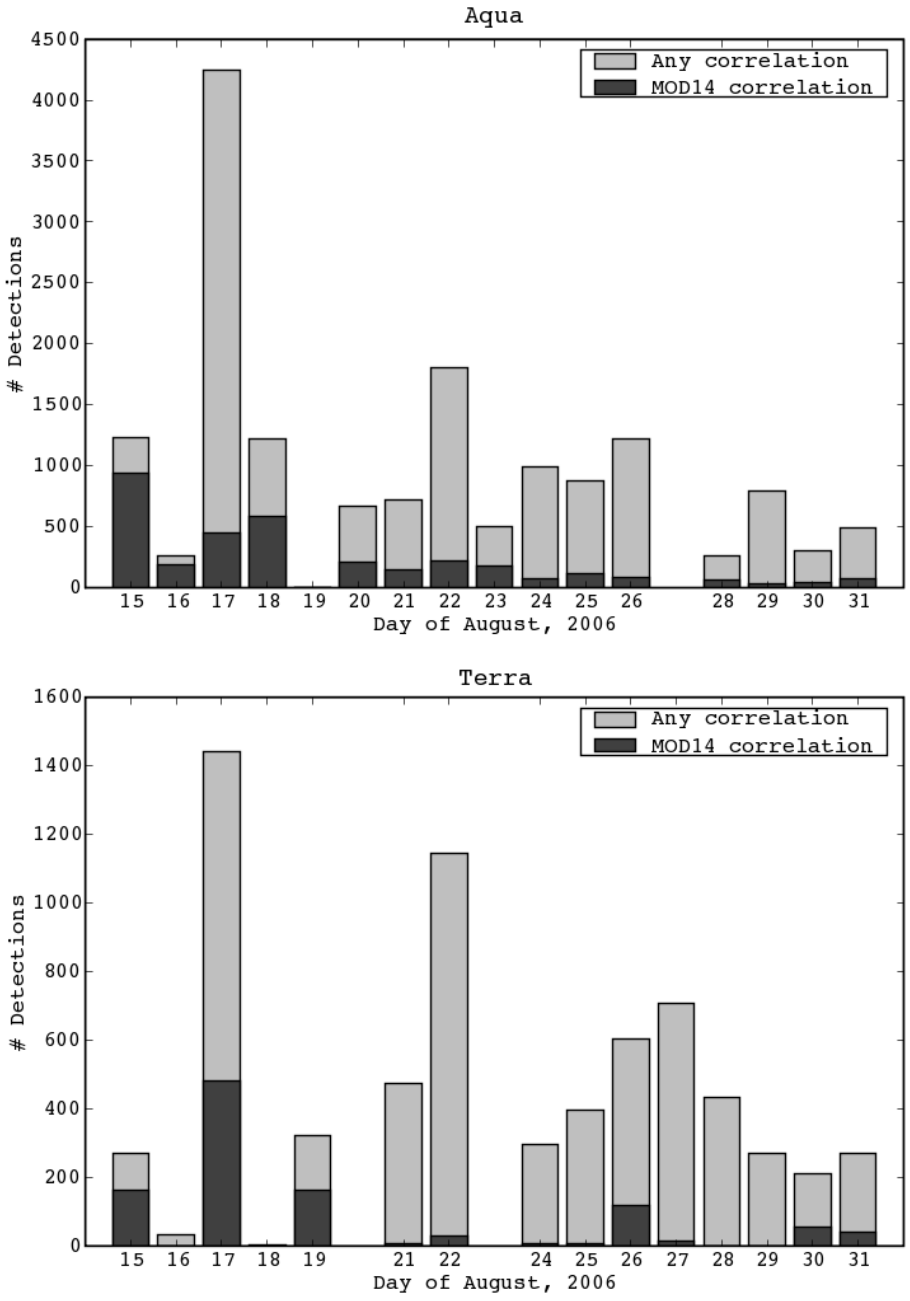

Figure 5.12: Number of fire detection by the 2.1 μm method that correlate with the MOD14 active fire product in comparison with the number of fire detections that correspond to either the MOD14 fire or the burnt area product.

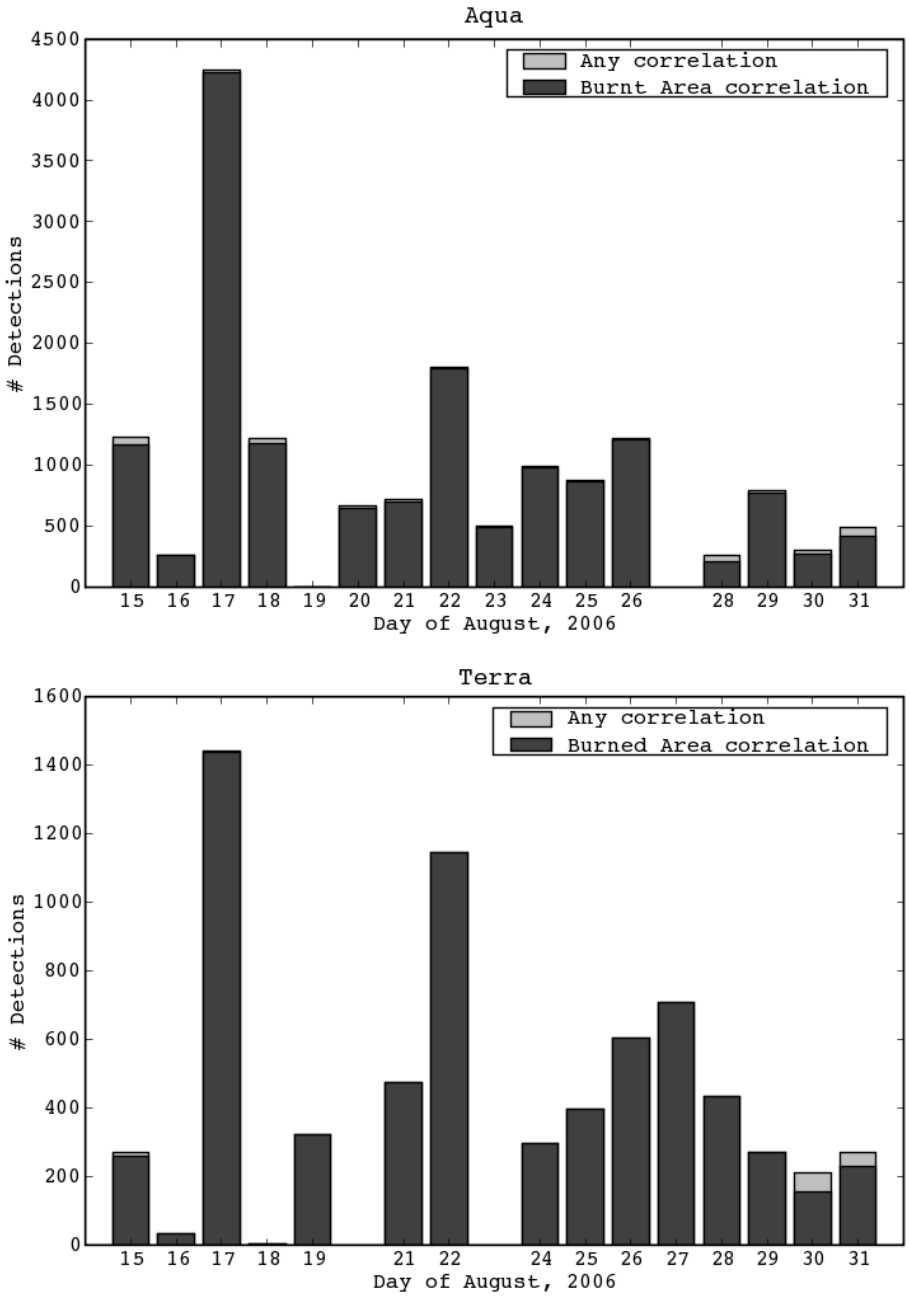

Figure 5.13: Number of fire detection by the 2.1 μm method that correlate with the burnt area product in comparison with the number of fire detections that correspond to either the MOD14 fire or the burnt area product.

tections that did correspond with the burnt areas but not with MOD14 fire detections. It shows that the average detection confidence of the fire detections by the algorithm based on the 2.1 μm channel of MODIS is consistently lower for those detections that onl correspond with the burnt area than the average confidence of those detections that also correspond with MOD14 fire detections. A large difference between the average confidences often coincides with a large number of detections that do not have a corresponding MOD14 detection. This suggest a connection between the detection confidence of a given detection by the proposed algorithm and its chance to correspond with a MOD14 fire detection.

Statistical analysis of all the fire detections (all days, both platforms) by the algorithm based on the 2.1 μm channel, shows that 75% of the detections that correspond with a MOD14 fire detection have a detection confidence higher than 57%. If only those detections with a confidence of 57% or higher are taken into account, the total number of detections (all days, both platforms) goes down by 79% from 22,470 (the total number with all detection confidences) to 4,729. The figures 5.16 to 5.20 show the same relations as the figures 5.11 to 5.15 but for the detections limited to those with a detection confidence of 57% and above.

As one would expect, this restricted dataset shows the same patterns as the total dataset. They are however less pronounced. It still shows a higher correlation between the burnt areas and the fire detections by the proposed algorithm than between the MOD14 fire detections and the fire detections by the proposed algorithm, but to a much lesser extend. The total number of fire detections of Aqua that did correspond with a burnt area but not with a MOD14 fire detection is 12,214 for the full dataset. In case of the limited dataset this number is only 1,182. The number for the Terra observations changes in a similar fashion, going down from 5,787 to 144. The average detection confidences of the correlation of the fire detections by the 2.1 μm channel based algorithm between the burnt areas and the MOD14 detections of the limited dataset are shown in figures 5.19 and 5.20 (p 99 and 100). In comparison to those for the full dataset,

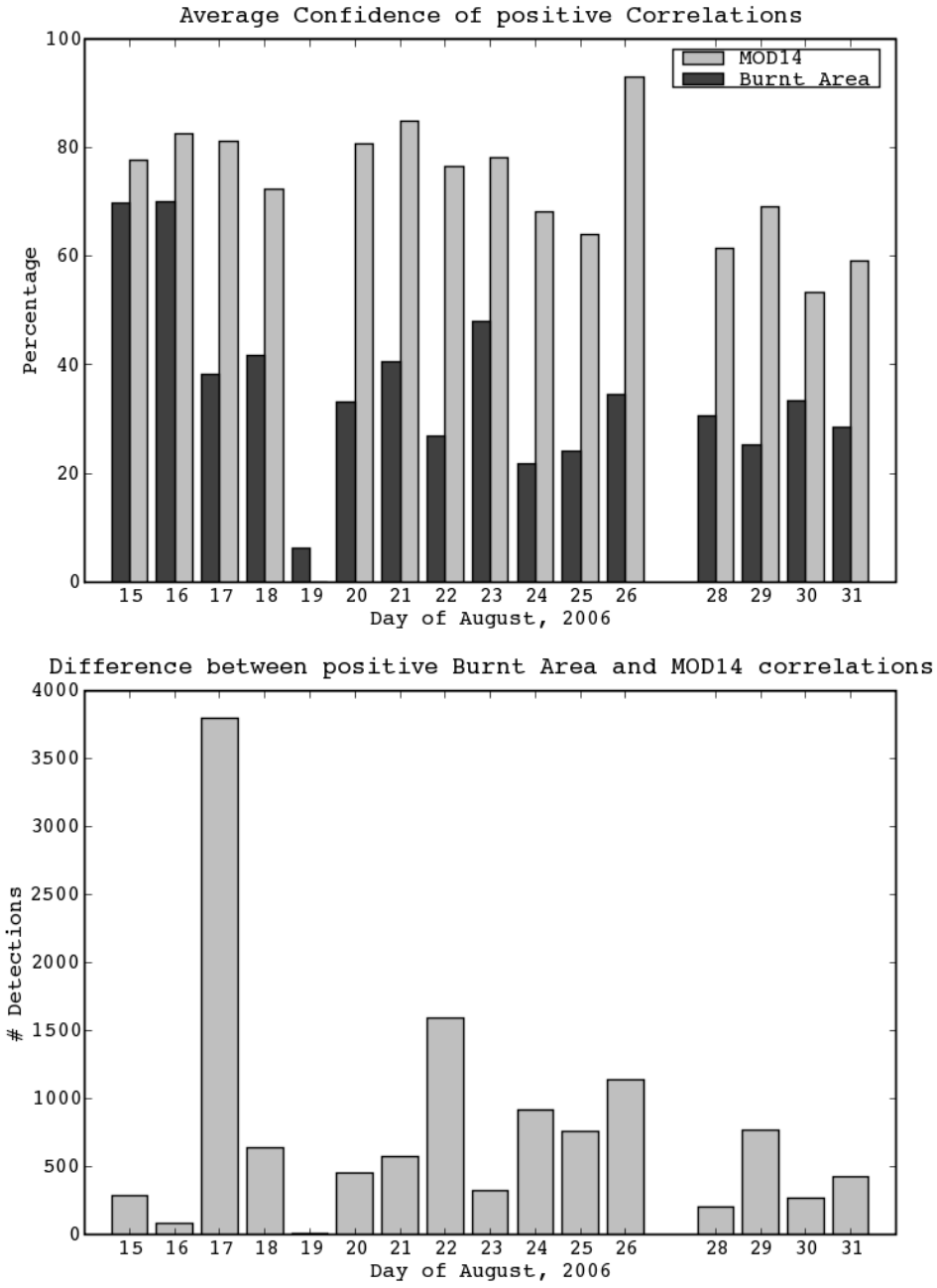

Figure 5.14: Average detection confidence for Aqua of the 2.1 μm method detections from Aqua observations correlating with MOD14 and the burnt area product (upper figure). The difference between the number of the detections correlating with the burnt area product and those correlating with MOD14 (lower figure).

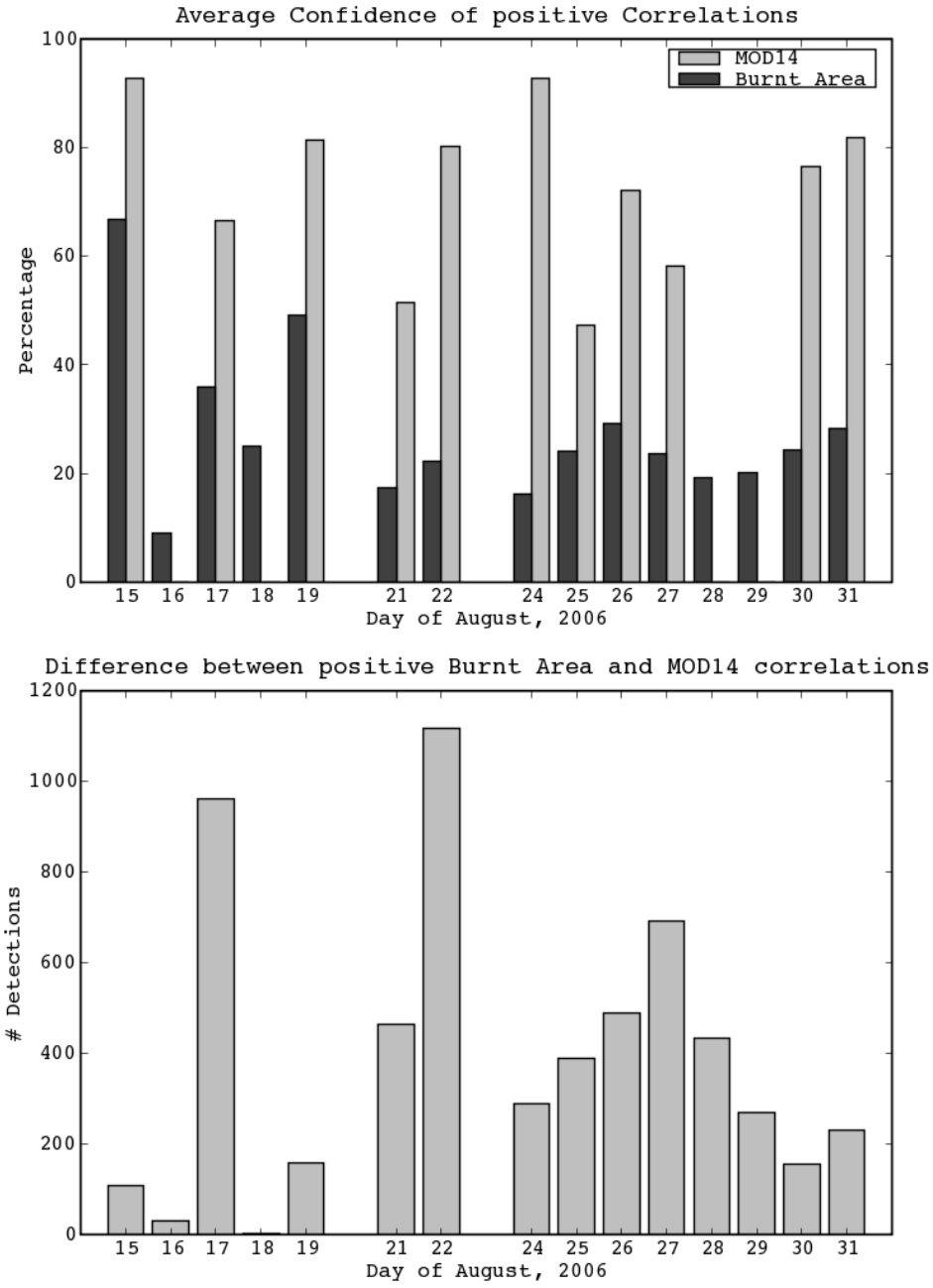

Figure 5.15: Average detection confidence for Terra of the 2.1 μm method detections from Terra observations correlating with MOD14 and the burnt area product (upper figure). The difference between the number of the detections correlating with the burnt area product and those correlating with MOD14 (lower figure).

they vary less and are at a higher level.

The figures 5.21 (p 102), 5.22 (p 103), 5.23 (p 104), 5.24 (p 105) show the fire detections of the 2.1 μm channel and there confidences for both, the full and reduces dataset for August 17 and 18. The figures show the good correlation between the 2.1 μm channel detections of high confidence and the MOD14 fire detections.

5.3 Performance Discussion

It is very unfortunate that only two high resolution ASTER scenes have been available to establish proper performance figures for the proposed algorithm. However, as the two ASTER scenes contain different kinds of fire complexes, they were useful to show the potential information gains as well as problems associated with fire detection based on the 2.1 μm channel method. The proposed algorithm showed that, in case of a big, intense fire, as the one in ASTER scene one, it is capable of providing more detailed spatial information than MOD14 with its more coarse resolution. It also showed that it cannot be a replacement for MOD14 and other similar algorithms. The proposed algorithm was almost of no use at all in the case of the second ASTER scene, which only contained a slim, much less intense fire front. The algorithm was only able to identify one fire cluster of four pixels along the whole front. The MOD14 algorithm, with its higher sensitivity to smaller and/or cooler fires proved itself to be not perfect but much better suited in such situations. With just one false positive detection by the proposed algorithm in ASTER scene one, this performance indicator is not yet a major concern as the algorithm is only meant to show the potential of the 2.1 μm channel for remote sensing of fires. False negatives, fires that were not classified as such, are expected to happen frequently. Due the the physical limits of the fire detections based on the 2.1 μm channel, smaller and cooler fires are not expected be detected.

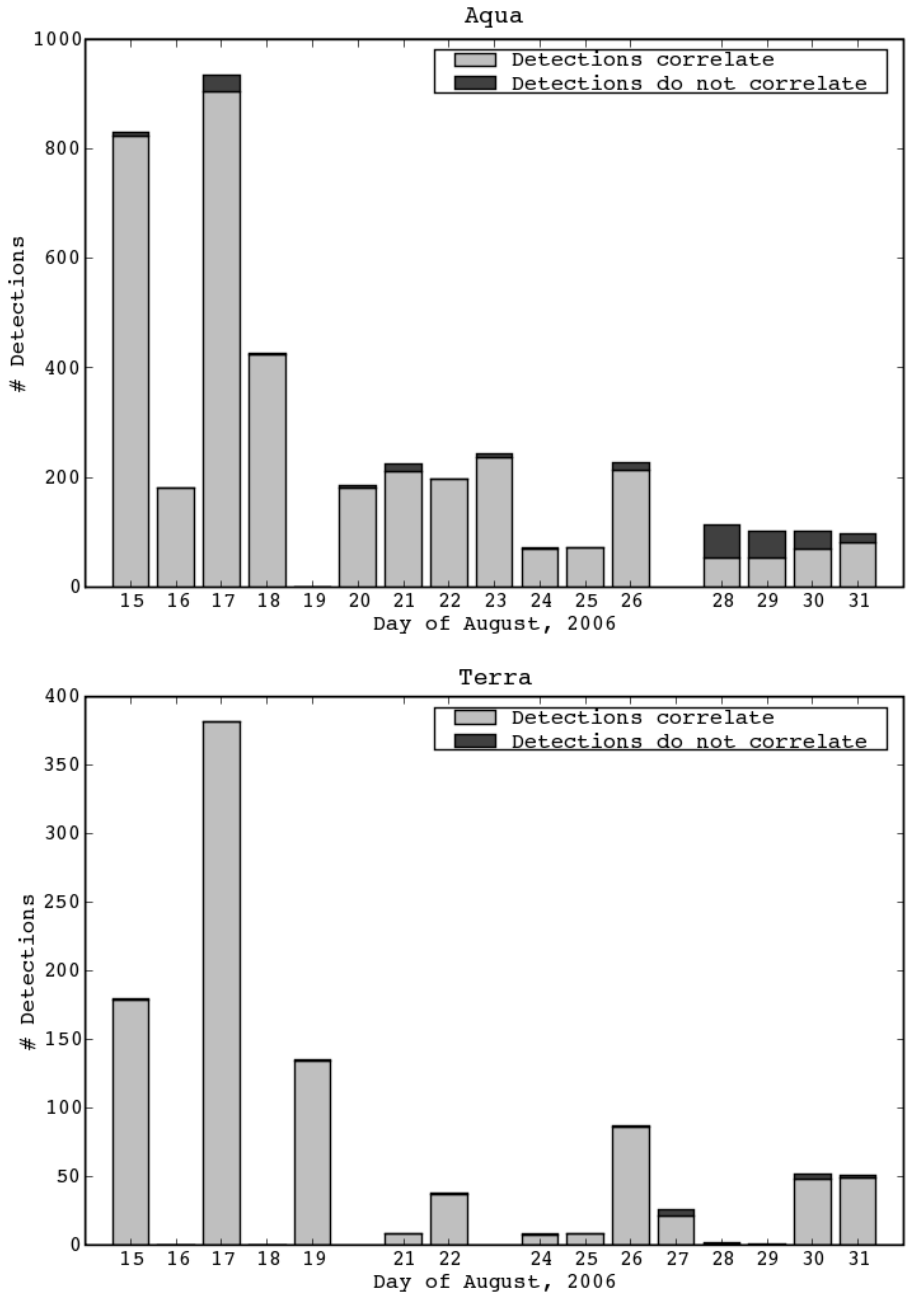

Figure 5.16: Number of fire detection by the 2.1 μm method that correlate with either the MOD14 active fire product or the burnt area mapping and number of those fire detections that correspond with neither of the two. The detections are limited to those with a detection confidence of at least 57%.

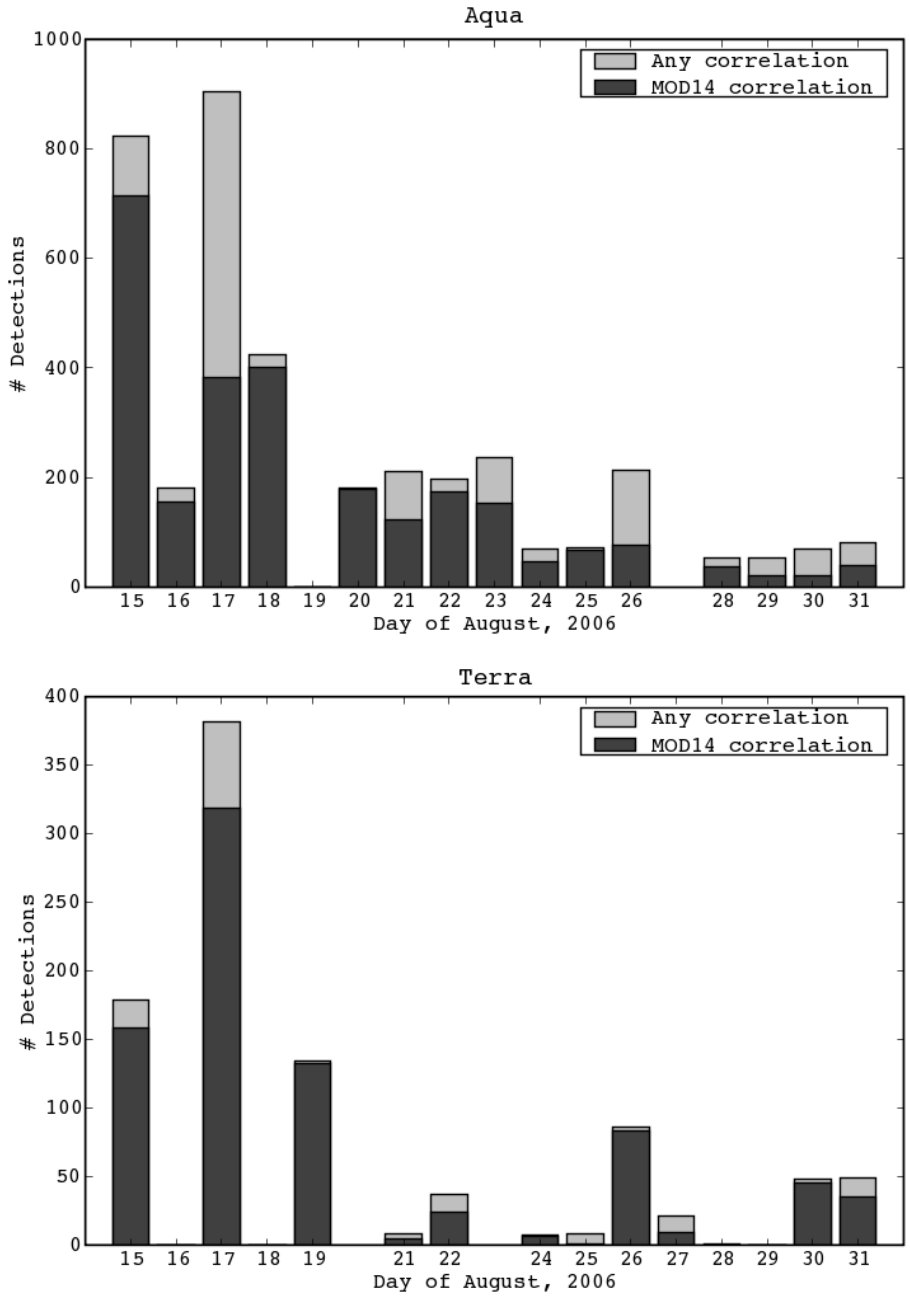

Figure 5.17: Number of fire detection by the 2.1 μm method that correlate with the MOD14 active fire product in comparison with the number of fire detections that correspond to either the MOD14 fire or the burnt area product. The detections are limited to those with a detection confidence of at least 57%.

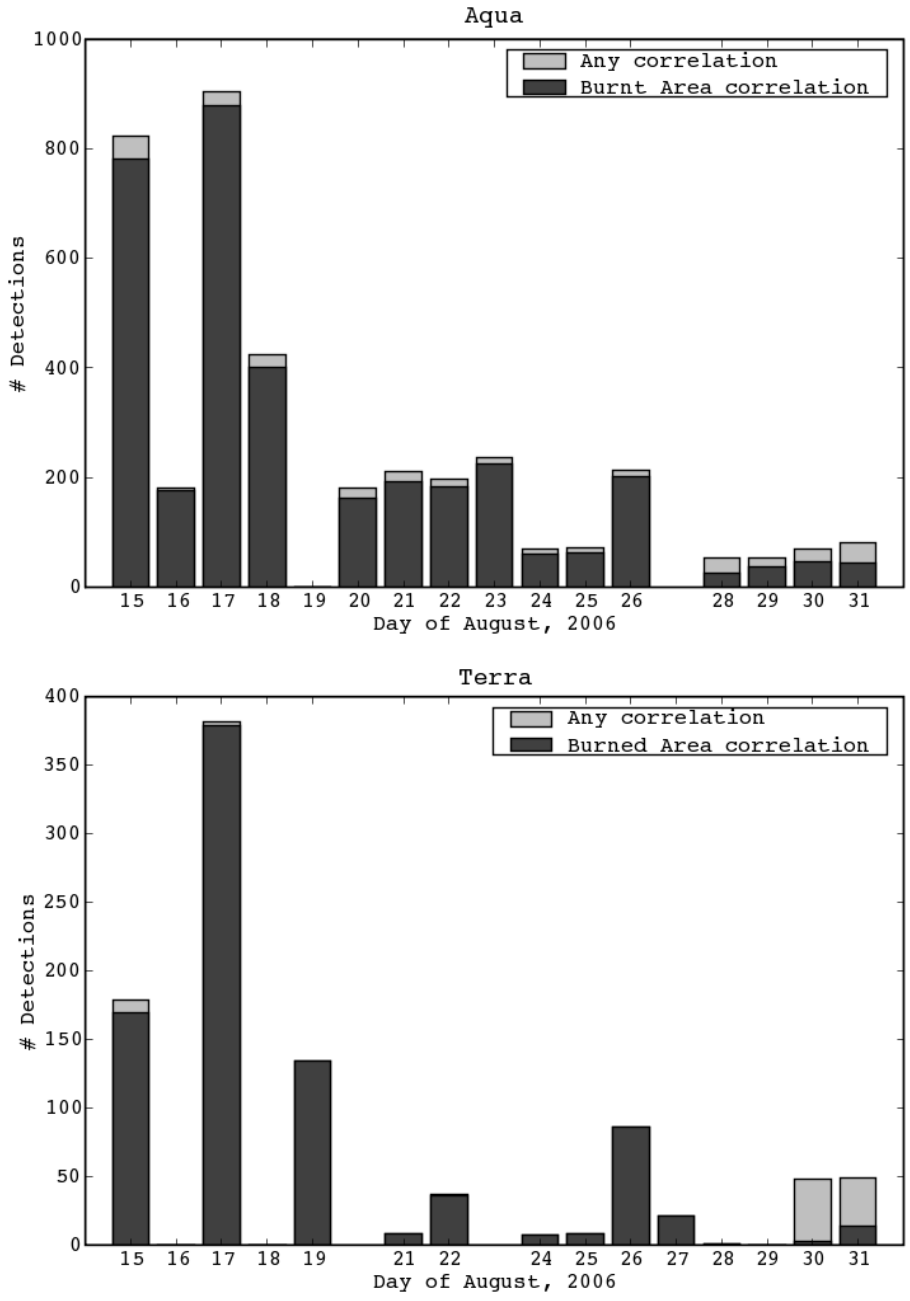

Figure 5.18: Number of Number of fire detection by the 2.1 μm method that correlate with the burnt area product in comparison with the number of fire detections that correspond to either the MOD14 fire or the burnt area product. The detections are limited to those with a detection confidence of at least 57%.

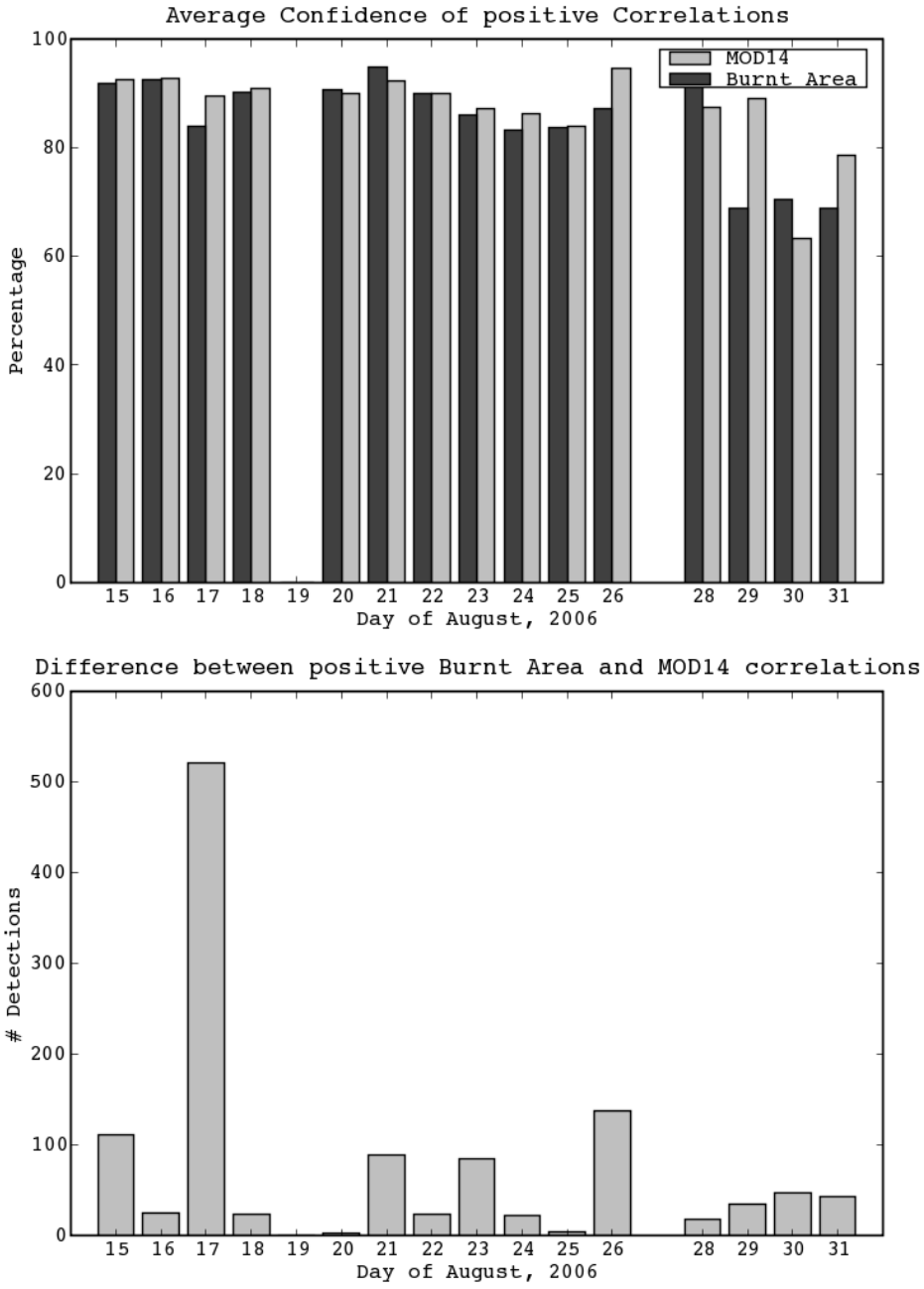

Figure 5.19: Average detection confidence of the 2.1 μm method detections from Aqua observations correlating with MOD14 and the burnt area product (upper figure). The difference between the number of the detections correlating with the burnt area product and those correlating with MOD14 (lower figure). The detections are limited to those with a detection confidence of at least 57%.

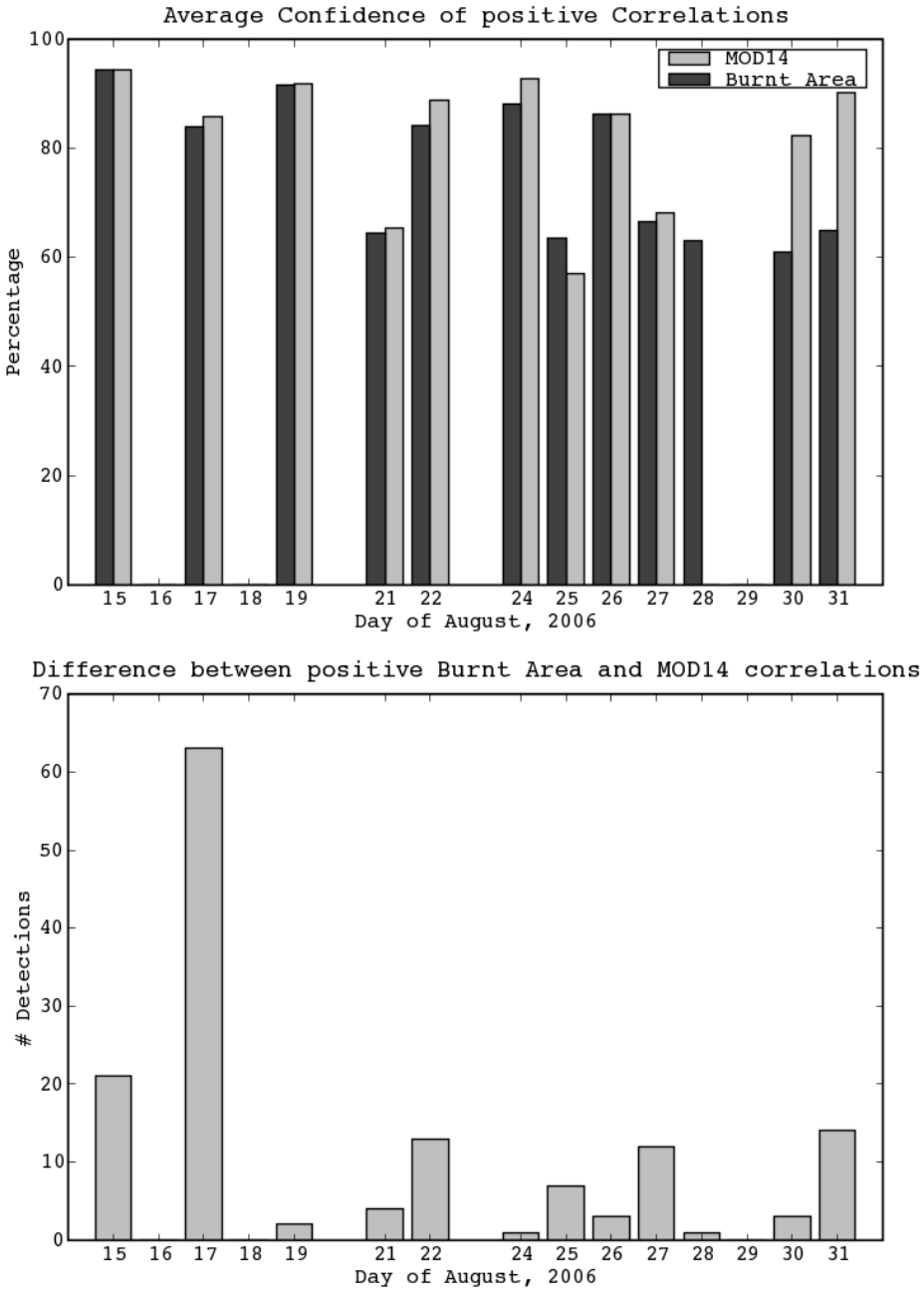

Figure 5.20: Average detection confidence of the 2.1 μm method detections from Terra observations correlating with MOD14 and the burnt area product (upper figure). The difference between the number of the detections correlating with the burnt area product and those correlating with MOD14 (lower figure). The detections are limited to those with a detection confidence of at least 57%.

Positive fire detections that do not match with MOD14 fire detections are of much more interest in the second performance test. When the fire detections of the proposed algorithm were compared to fire detections of MOD14 and monthly burnt area maps, they in generally showed a good correlation with both datasets. However, a large number of low confidence detections only matched with the burnt area maps but not with the active fire detections of MOD14. At this stage, the author is reluctant to filter those detections as false positives. It is possible to differentiate between the 'real' positive fire detections matching the detections by MOD14 and the large number of detections matching only the burnt area maps by their detection confidences. The fact that these 'false' positives are not random but correlate with the burnt areas and that visual inspection of the images showed no undetected clouds, suggest that they might not be triggered by active fires but by something related to them.

One possible explanation for this phenomena could be white ash that is left behind by the moving fire front if the vegetation is completely combusted. White ash has a significantly higher reflectance in the 2.1 μm channel than vegetation. If a pixel, from one day to the next, is not anymore covered by vegetation but by white ash, the observed reflectance would be higher than the expected reflectance. It is possible that this reflectance change is high enough to trigger a fire detection. It would also be possible that highly reflective soil that is exposed after the fire is responsible for these detections. This is however less likely as this phenomena would be expected to last for an extended period of time if it was caused by soil. Figure 5.21 (p 102) shows an extreme example of big areas of low confidence detections. Figures 5.23 (p 104) and 5.25 (p 106) show how this area of low detection confidence quickly vanishes over the course of three days.

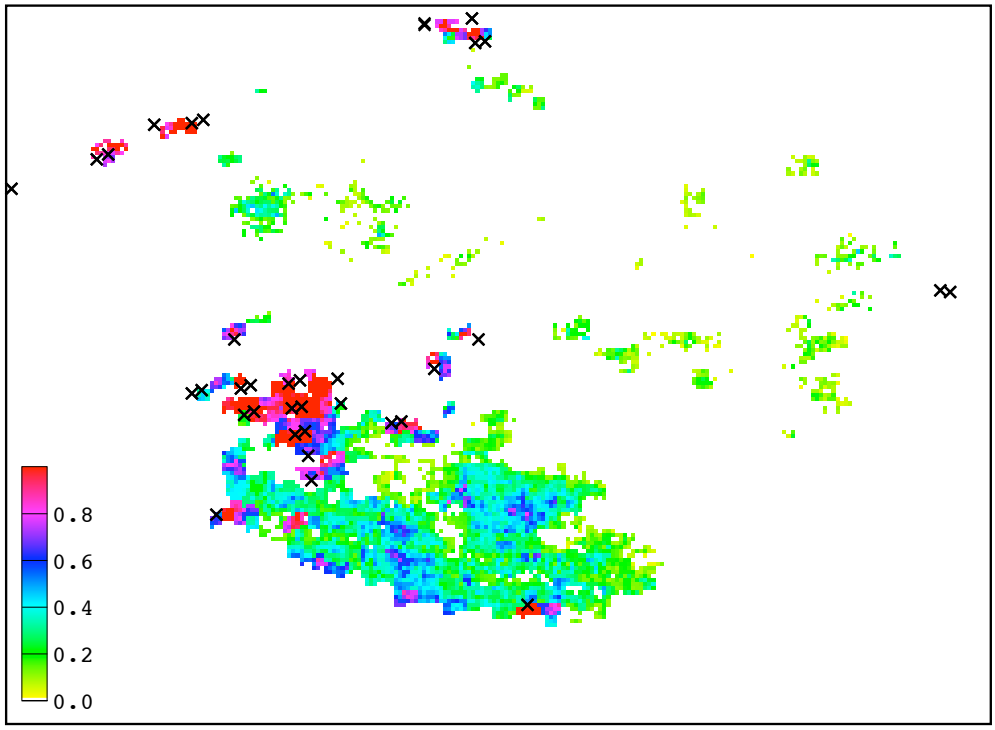

Figure 5.21: Fire detection confidence of the 2.1 μm channel and fires detected by MOD14 in a part of the case study area on the 17th of August 2006

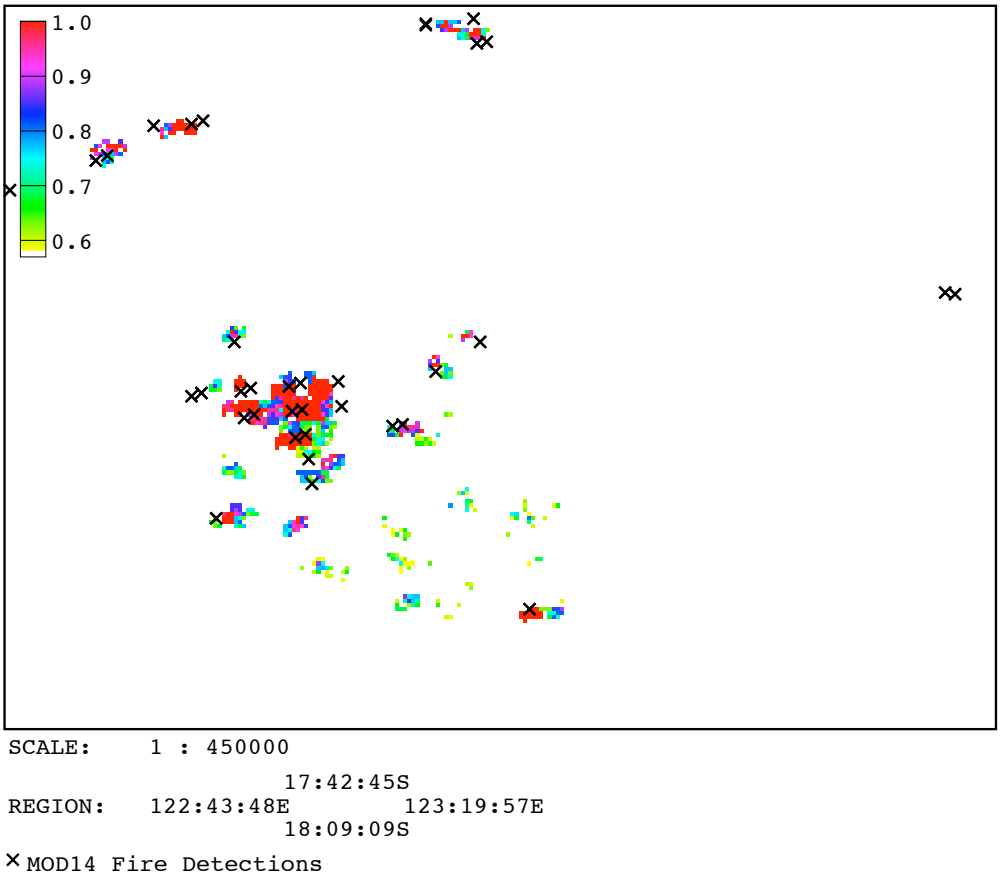

Figure 5.22: Fire detection confidence of the 2.1 μm channel for fires with a detection confidence above 0.57 and fires detected by MOD14 in a part of the case study area on the 17th of August 2006

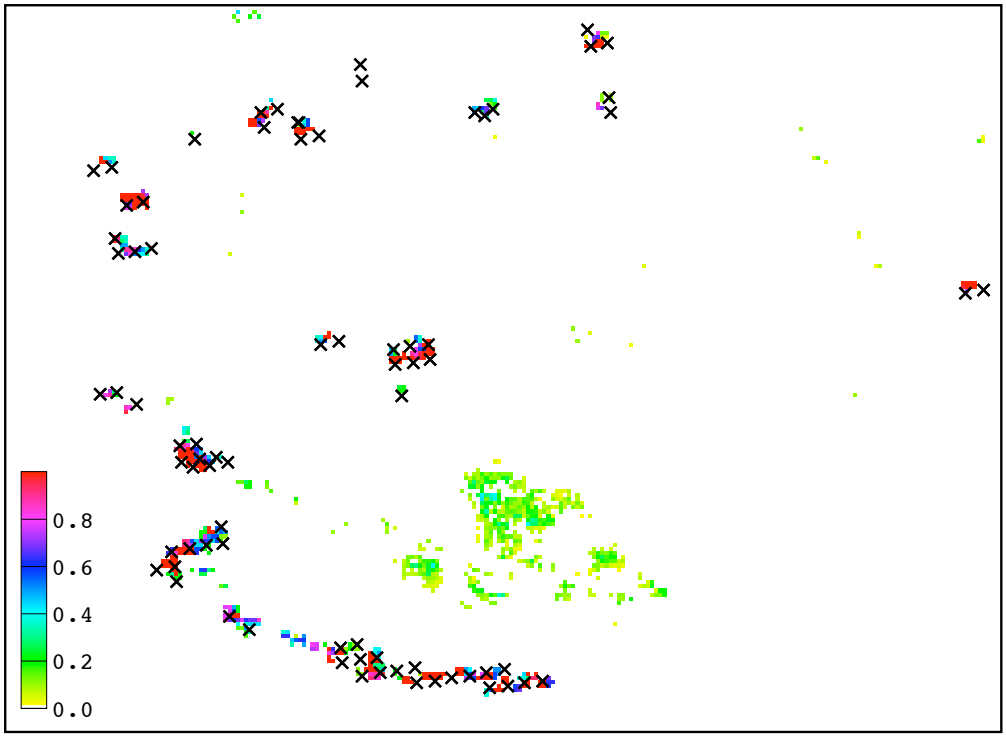

Figure 5.23: Fire detection confidence of the 2.1 μm channel and fires detected by MOD14 in a part of the case study area on the 18th of August 2006

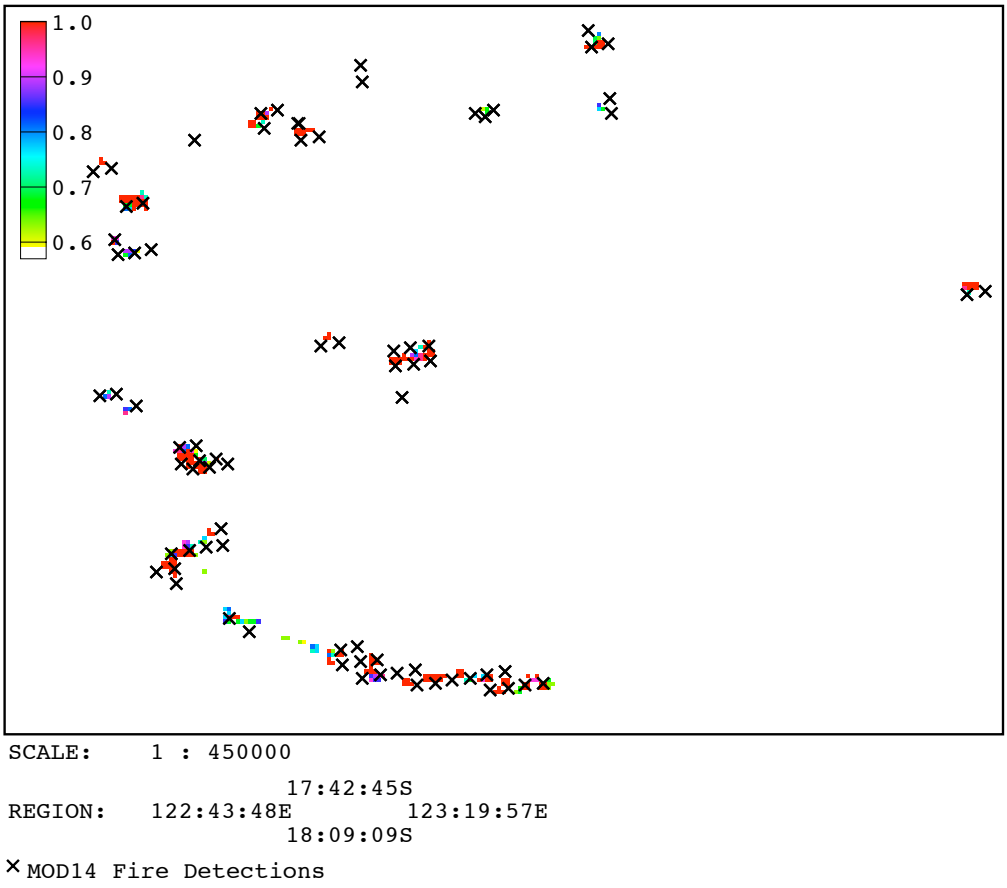

Figure 5.24: Fire detection confidence of the 2.1 μm channel for fires with a detection confidence above 0.57 and fires detected by MOD14 in a part of the case study area on the 18th of August 2006

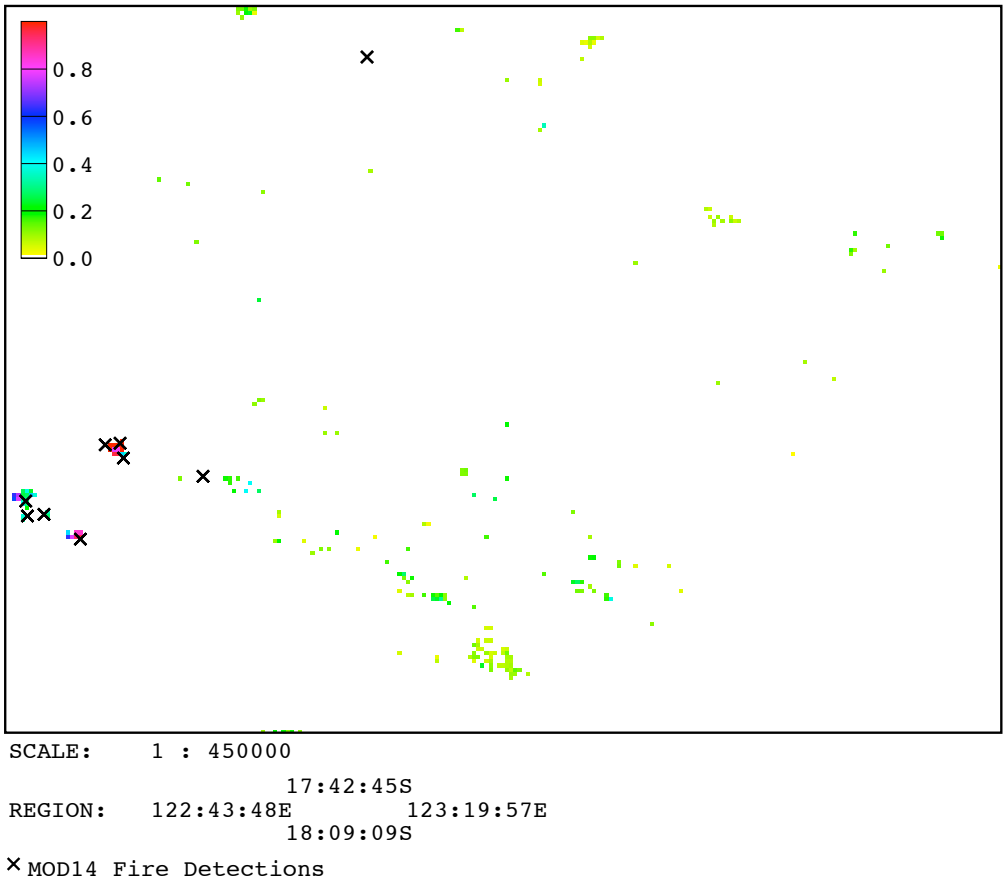

Figure 5.25: Fire detection confidence of the 2.1 μm channel and fires detected by MOD14 in a part of the case study area on the 20th of August 2006

Table 5.1: Summary of the performance of the proposed algorithm for Aqua (full dataset). It shows the total number of detections by the algorithm based on the 2.1 μm channel and how many of those correlated with MOD14 detections, the burnt area product and none of those two.

Day	**Detections**	**MOD14**	**%**	**Burnt Area**	**%**	**none**	**%**
15	1237	943	76.2	1173	94.8	9	0.7
16	265	183	69.1	257	97.0	4	1.5
17	4297	447	10.4	4222	98.3	47	1.1
18	1225	580	47.3	1181	96.4	9	0.7
19	8	0	0.0	4	50.0	4	50.0
20	674	212	31.5	643	95.4	9	1.3
21	736	145	19.7	701	95.2	16	2.2
22	1816	220	12.1	1793	98.7	7	0.4
23	531	181	34.1	494	93.0	25	4.7
24	1002	72	7.2	981	97.9	12	1.2
25	890	116	13.0	864	97.1	18	2.0
26	1247	79	6.3	1205	96.6	27	2.2
28	377	68	18.0	211	56.0	111	29.4
29	886	31	3.5	769	86.8	91	10.3
30	383	40	10.4	267	69.7	76	19.8
31	611	71	11.6	422	69.1	118	19.3

Table 5.2: Summary of the performance of the proposed algorithm for Terra (full dataset). It shows the total number of detections by the algorithm based on the 2.1 μm channel and how many of those correlated with MOD14 detections, the burnt area product and none of those two.

Day	**Detections**	**MOD14**	**%**	**Burnt Area**	**%**	**none**	**%**
15	274	163	59.5	260	94.9	3	1.1
16	33	0	0.0	31	93.9	2	6.1
17	1447	481	33.2	1439	99.4	5	0.3
18	5	0	0.0	3	60.0	2	40.0
19	325	162	49.8	320	98.5	5	1.5
21	476	8	1.7	472	99.2	4	0.8
22	1154	29	2.5	1145	99.2	8	0.7
24	306	6	2.0	294	96.1	12	3.9
25	403	8	2.0	397	98.5	6	1.5
26	625	117	18.7	605	96.8	20	3.2
27	717	13	1.8	706	98.5	11	1.5
28	437	0	0.0	433	99.1	4	0.9
29	273	0	0.0	269	98.5	4	1.5
30	214	54	25.2	155	72.4	5	2.3
31	312	40	12.8	230	73.7	42	13.5

Table 5.3: Summary of the performance of the proposed algorithm for Aqua (limited dataset). It shows the total number of detections by the algorithm based on the 2.1 μm channel and how many of those correlated with MOD14 detections, the burnt area product and none of those two.

Day	**Detections**	**MOD14**	**%**	**Burnt Area**	**%**	**none**	**%**
15	829	713	86.0	781	94.2	5	0.6
16	180	155	86.1	177	98.3	0	0.0
17	933	383	41.1	879	94.2	29	3.1
18	427	401	93.9	401	93.9	3	0.7
19	1	0	0.0	0	0.0	1	100.0
20	186	179	96.2	162	87.1	5	2.7
21	226	124	54.9	193	85.4	14	6.2
22	196	173	88.3	182	92.9	0	0.0
23	244	152	62.3	224	91.8	8	3.3
24	72	47	65.3	60	83.3	3	4.2
25	72	67	93.1	63	87.5	1	1.4
26	228	76	33.3	201	88.2	15	6.6
28	113	36	31.9	26	23.0	59	52.2
29	102	20	19.6	36	35.3	48	47.1
30	101	22	21.8	47	46.5	32	31.7
31	98	39	39.8	43	43.9	16	16.3

Table 5.4: Summary of the performance of the proposed algorithm for Terra (limited dataset). It shows the total number of detections by the algorithm based on the 2.1 μm channel and how many of those correlated with MOD14 detections, the burnt area product and none of those two.

Day	**Detections**	**MOD14**	**%**	**Burnt Area**	**%**	**none**	**%**
15	180	158	87.8	169	93.9	1	0.6
16	0	0	nan	0	nan	0	nan
17	382	319	83.5	379	99.2	0	0.0
18	0	0	nan	0	nan	0	nan
19	135	132	97.8	134	99.3	1	0.7
21	8	4	50.0	8	100.0	0	0.0
22	38	24	63.2	36	94.7	1	2.6
24	8	6	75.0	7	87.5	1	12.5
25	8	1	12.5	8	100.0	0	0.0
26	87	83	95.4	86	98.9	1	1.1
27	26	9	34.6	21	80.8	5	19.2
28	2	0	0.0	1	50.0	1	50.0
29	1	0	0.0	0	0.0	1	100.0
30	52	45	86.5	3	5.8	4	7.7
31	51	35	68.6	14	27.5	2	3.9

Chapter 6

Concluding Remarks and Recommendations

It was the intention of this work to research ways to improve the spatial resolution of fire detection with MODIS by utilizing the 2.1 μm channel. Furthermore it was intended to generally open the gates for new approaches to fire monitoring from satellites different from those directly based on the work by Dozier (1981).

The theoretical study of blackbodies of typical fire temperatures has shown that fire detection methods based on the 2.1 μm channel of MODIS are possible but limited to flaming fires of temperatures above 800 K. Smoldering fires of lower temperatures can generally not be expected to cover a big enough fraction of a pixel to generate enough radiation in the 2.1 μm channel in order to differentiate those fires from a reflective background.

During the development of the algorithm, it became clear that good cloud masking is crucial for fire detection algorithms of operational performance. Clouds are expected to be the most common cause for false positive detections due to their high reflectance values across a wide range of the electromagnetic spectrum and their high reflectance change when

compared to the expected, cloud free reflectance values of a given pixel. With improvements in cloud masking, the algorithm has not only the potential to improve with regards to the number of false positives but there is also the chance of decreasing the number of false negatives. Due to its physical limitations, the algorithm will always suffer from false negatives as it will not be able to detect small and/or cool fires. However, the algorithm could possibly be adjusted to be more sensitive to smaller/cooler fires by reducing the currently required minimal reflectance change value of 0.25 without increasing the number of cloud caused false positives if a better cloud mask can be applied.

The comparison of fire detections by the method developed in this work with high resolution ASTER fire maps and MOD14 fire detections has shown that the algorithm can achieve its goal. In the case of large intense fire complexes, it can provide a more detailed spatial distribution information of the fire front than the MOD14 fire detection is able to achieve. It also showed that the proposed algorithm, as expected, will not be able to replace those algorithms that use the brightness temperatures of the MIR and TIR region. Due to their higher sensitivity to smaller and/or cooler fires, they have an advantage the proposed algorithm will not be able to match. Due to the very small number of available ASTER scenes that contain fires over Australia, it was unfortunately not possible to get a better impression of the algorithm's performance when compared to high resolution datasets. This could possibly be improved by developing reflectance prediction models for other regions of the Earth for which more ASTER datasets are available or by fieldwork campaigns that manually map the extends of fires.

The more interesting possibilities for future research, however, were opened up by the comparison of the fire detections by the 2.1 μm channel method with MOD14 fire detections and burnt area maps over the course of two weeks. The proposed algorithm identified pixels as containing a fire that seem to be areas that have been recently affected by a fire but are unlikely to be actively burning. This phenomena could be caused by white ash,

a results of total combustion of vegetation, which has a much higher reflectance in the 2.1 μm channel than vegetation. If this is the case, these data could be used to gain information on fire temperature, biomass loss and the amount of released carbon-dioxide. It is recommended to put future research efforts towards this subject to investigate these issues.

Furthermore, the ability to separate the reflectance caused by a fire from the reflectance of its non-burning background has the possibility to provide additional data as input into algorithms that determine the flaming-smoldering ratio of fires. These algorithms exploit the different response of different channels to fires of different temperatures. They currently make use of the 3 μm and 11 μm channels. With the addition of the 2.1 μm channel, three channels are available with very different responses to different temperatures. The 2.1 μm channel almost exclusively responds to fires of flaming temperatures, the 3 μm channel is sensitive to both (flaming and smoldering fires) and the 11 μm channel is mostly sensitive to large fires of smoldering temperatures. This combination of channels has the potential to provide a product superior to today's.

This work showed that the claim made by Li et al. (2000b), that fire detection and monitoring methods with currently available satellite based sensors have not yet been fully exploited, is true. Combining proven methods with new approaches can provide more information on fires than currently available. This work however is not close to exploiting all possibilities. It can much more be a starting point for future research, raising more issue and provoking more questions that it can solve. It is expected that many of these questions will be answered only in combined efforts from scientist in a variety of disciplines.

Bibliography

Abrams, M., Hook, S., 2002. ASTER User Handbook. Jet Propulsion Laboratory.

Ackerman, S., Strabala, K., Menzel, P., Frey, R., Moeller, C., Gumley, L., Baum, B., Schaaf, C., Riggs, G., 1997. Discriminating Clear-Sky from Cloud with MODIS - Algorithm Theoretical Basis Document (MOD35).

American Meteorological Society, 2000. Glossary of Meteorology. URL: http://amsglossary.allenpress.com/glossary, 07/08/2006.

Arino, O., Melinotte, J.-M., Calabresi, G., 1993. Fire, cloud, land, water: the 'Ionia' AVHRR CD-Browser of ESRIN. Earth Observation Quaterly 41.

Arino, O., Rosaz, J.-M., 1999. 1997 and 1998 World ATSR Fire Atlas using ERS-2 ATSR-2 Data. In: Proceedings of the Joint Fire Science Conference, Boise, 15-17, June 1999.

ASTER Science Team, 2005. Geolocation Discrepancies with ASTER Level-1 Data.

Bachelet, D., Neilson, R. P., Lenihan, J. M., Drapek, R. J., 2001. Climate Change Effects on Vegetation Distribution and Carbon Budget in the United States. Ecosystems 4, 164–185.
URL `http://www.springerlink.com/content/95teky5h1r6hx85q`

Barducci, A., Guzzi, D., Marcoionni, P., Pippi, I., 2003. Infrared detection of active fires and burnt areas: theory and observations. Infrared Physics & Technology 43, 119 – 125.

Chuvieco, E. (Ed.), 1999. Remote Sensing of Large Wildfires. Springer, Berlin.

Crutzen, P. J., Andreae, M. O., 1990. Biomass burning in the tropics: impact on atmospheric chemistry and biogeochemical cycles. Science 250 (4988), 1669 – 1678.

Dozier, J., 1981. A method for satellite identification of surface temperature fields of subpixel resolution. Remote Sensing of Environment 11, 221 – 229.

ESRI, 1998. ESRI Shapefile Technical Description.

Flannigan, M., 1985. Forest Fire Monitoring Using the NOAA Satellite Series. M.s. thesis, Department of Atmospheric Sciences, Colorado State University, Fort Collins, Colorado.

Flannigan, M., Von der Haar, T., 1986. Forest fire monitoring using NOAA satellite AVHRR. Canadian Journal of Forest Research 16 (975-982).

Flasse, S., Ceccato, P., 1996. A contextual algorithm for AVHRR fire detection. International Journal of Remote Sensing 17, 419–424.

Giglio, L., Descloitresa, J., Justicec, C. O., Kaufman, Y. J., 2003a. An Enhanced Contextual Fire Detection Algorithm for MODIS. Remote Sensing of Environment 87, 273–282.

Giglio, L., Kendall, J. D., Justice, C. O., 1999. Evaluation of global fire detection algorithms using simulated AVHRR infrared data. International Journal of Remote Sensing 20, 1947–1985.

Giglio, L., Kendall, J. D., Mack, R., 2003b. A multi-year active fire dataset for the tropics derived from the TRMM VIRS. International Journal of Remote Sensing 24 (22), 4505 – 4525.

Giglio, L., Kendall, J. D., Tucker, C. J., 2000. Remote sensing of fires with the TRMM VIRS. International Journal of Remote Sensing 21, 203 – 207.

GRASS Development Team, 2005. GRASS 6.0 Users Manual. URL: http://grass.itc.it/grass60/manuals/html_grass60/, 01/11/2005.

GRASS Development Team, 2006. GRASS Authors. URL: http://freegis.org/cgi-bin/viewcvs.cgi/ checkout /grass6/AUTHORS, 01/11/2005.

Gregoire, J. M., Tansey, K., Silva, J. M. N., 2003. The GBA2000 initiative: developing a global burnt area database from SPOT-vegetation imagery. International Journal of Remote Sensing 24, 1369–1376. URL http://dx.doi.org/10.1080/0143116021000044850

Houghton, J., Filhno, L. M., Lee, J. H., Callander, B., Haites, E., Harris, N., Maskell, K. (Eds.), 1995. IPCC Climate Change. Cambridge University Press, Cambridge.

Jacob, F., Petitcolin, F., Schmugge, T., Vermote, E., French, A., Ogawa, K., 2004. Comparison of land surface emissivity and radiometric temperature derived from MODIS and ASTER sensors. Remote Sensing of Environment 90, 137–152.

Ji, Y., Stocker, E., 2002. An overview of the TRMM/TSDIS fire algorithm and product. International Journal of Remote Sensing 23, 3285 – 3303.

Justice, C. O., Giglio, L., Korontzi, S., Owensa, J., Morisettec, J., Roya, D., Descloitres, J., Alleaumed, S., Petitcoline, F., Kaufman, Y., 2002. The MODIS fire products. Remote Sensing of Environment 83, 244–262.

Justice, C. O., Kendall, J. D., Dowty, P. R., Scholes, R. J., 1996. Satellite remote sensing of fires during the SAFARI campaign using NOAA-AVHRR data. Journal OF Geophysical Research, 23851–23863.

Justice, C. O., Malingreau, J.-P., Setzer, A. W., 1993. Satellite remote sensing of fires; potential and limitations. In: Crutzen, P. J., Goldammer, J. (Eds.), Fire in the Environment. John Wiley and Sons Ltd, pp. 77–88.

Kaufman, Y., Justice, C., November 1998. Algorithm Technical Background Document - MODIS Fire Products. URL: http://modis.gsfc.nasa.gov/data/atbd/atbd_mod14.pdf, 19/05/2004.

Kaufman, Y. J., Fraser, R. S., 1997. The effect of smoke particles on clouds and climate forcing. Science 277 (5332), 1636 – 1639.

Kaufman, Y. J., Justice, C., Flynn, L., Kendall, J., Prins, E., Giglio, L., Ward, D. E., Menzel, P., Setzer, A., 1998. Potential Global Fire Monitoring from EOS-MODIS. Journal of Geophysical Research 103, 32215– 32238.

Langaas, S., Muirhead, K., 1989. Monitoring bushfires in west africa by weather satellites. In: Proceedings of the 22nd International Symposium on Remote Sensing of Environment, October 20-26, Abidjan, Cote d'Ivoire. pp. 253–268.

Langenfelds, R. L., Francey, R. J., Pak, B. C., Steele, L. P., Lloyd, J., Trudinger, C. M., Allison, C. E., 2002. Interannual growth rate variations of atmospheric CO2 and its 13C, H2, CH4, and CO between 1992 and 1999 linked to biomass burning. Global Biogeochemical Cycles 16 (3).

Lee, T., Tag, P., 1990. Improved detection of hotspots using the AVHRR 3.7 μm channel. Bulletin of The American Meterological Society 71, 1722–2730.

Li, Z., Kaufman, Y. J., Ichoku, C., Fraser, R., Trishchenko, A., Giglio, L., Jin, J., Yu, X., September 2000a. A Review of AVHRR-based Active Fire Detection Algorithms: Principles, Limitations, and Recommendations.

Li, Z., Nadon, S., Cihlar, J., 2000b. Satellite-based detection of Canadian boreal forest fires: development and application of the algorithm. International Journal of Remote Sensing 21, 3057–3069.

Lillesand, T. M., Kiefer, R. W., Chipman, J. W., 2004. Remote Sensing and Image Interpretation, 5th Edition. John Wiley and Sons.

Maier, S. W., August 2002. MODIS Black Body Temperature (BBT) Processor.

Maier, S. W., 2006. Using the predictive power of a kernel driven BRDF model to map clouds and burnt areas. In: 4th International Workshop on Multiangular Measurements and Models, 20-14 March, Sydney, Australia.

Malingreau, J.P. and Justice, C.O., (editors), 1997. The IGBP-DIS Satellite Fire Detection Algorithm Workshop Technical Report. IGBP-DIS Working Paper 17,NASA/GSFC, Greenbelt, Maryland, USA.

Matson, M., G. S., Robinson, J., 1987. Fire detection using data from the NOAA-N satellites. International Journal of Remote Sensing 8 (7), 961–970.

Matson, M., Dozier, J., 1981. Identification of subresolution high temperature sources using a thermal IR sensor. Photogrammetric Engineering and Remote Sensing 47 (9), 1311–1318.

Matson, M., Holben, B., 1987. Satellite detection of tropical burning in Brazil. International Journal of Remote Sensing 8 (3), 509–516.

Matson, M., Schneider, S., Aldridge, B., Satchwell, B., 1984. Fire Detection Using the NOAA-Series Satellites. NOAA Technical Report NESDIS 7.

Morisette, J. T., Giglio, L., Csiszar, I., Justice, C. O., 2005. Validation of the MODIS active fire product over Southern Africa with ASTER data. International Journal of Remote Sensing 26 (19), 4239–4264.

Mota, B. W., Pereira, J. M. C., Oom, D., Vasconcelos, M. J. P., Schultz, M., 2005. Screening the ESA ATSR-2 World Fire Atlas (1997–2002). Atmospheric Chemistry and Physics Discussions, 4641–4677.

Muirhead, K., Cracknell, A., 1984. Identification of gas flares in the North Sea using satellite data. International Journal of Remote Sensing 5 (1), 199–212.

NASA, 2005. MODIS Web - Technical Specifications. URL: http://modis.gsfc.nasa.gov/about/, 01/11/2005.

Pereira, A. J., Setzer, A., dos Santos, J., 1991. Fire Estimates in Savannas of Central Brazil with Thermal AVHRR/NOAA Calibrated by TM/Landsat. In: Proceedings of the 24th International Symposium on Remote Sensing of Environment, Rio de Janeiro, Brazil, 27-31 May 1991.

Petitcolin, F. R., Vermote, E. F., 2001. Applications of middle infrared surface reflectance from MODIS data. In: Geoscience and Remote Sensing Symposium, 2001. IGARSS '01. IEEE 2001. Vol. 1. pp. 381 – 383.

Potter, C., Tan, P.-N., Steinbach, M., Klooster, S., Kumar, V., Myneni, R., Genovese, V., 2003. Major disturbance events in terrestrial ecosystems detected using global satellite data sets. Global Change Biology 9 (7).

Prins, E. M., Menzel, W., 1992. Geostationary satellite detection of biomass burning in South America. International Journal of Remote Sensing 13, 2783–2799.

Rees, W. G., 2001. Physical Principles of Remote Sensing. Cambridge University Press, Cambridge.

Roujean, J.-L., Leroy, M., Deschamps, P.-Y., 1992. A Bidirectional Reflectance Model of the Earth's Surface for the Correction of Remote Sensing Data. Journal OF Geophysical Research 97, 20455–20468.

Salisbury, J. W., D'Aria, D. M., 1992. Emissivity of Terrestrial Materials in the 8-14 μm Atmospheric Window. Remote Sensing of Environment 42, 83–106.

Salisbury, J. W., D'Aria, D. M., 1994. Emissivity of Terrestrial Materials in the 3-5 μm Atmospheric Window. Remote Sensing of Environment 47, 345–361.

Setzer, A. W., Pereira, M. C., 1991. Amazonia Biomass Burning in 1987 and an Estimate of Their Tropospheric Emissions. Ambio 20 (1), 19–22.

Stephens, G., Matson, M., 1989. Fire detection using the noaa-n satellites. In: 10th Conference on Fire and Forest Meteorology, April 17-21, Ottawa, Canada.

Stroppiana, D., Pinnock, S., Gregoire, J.-M., 2000. The Global Fire Product: daily fire occurrence from April 1992 to December 1993 derived from NOAA AVHRR data. International Journal of Remote Sensing 21, 1279 – 1288.

Tansey, K., Grégoire, J-M., Binaghi, E., Boschetti, L., Brivio, P.A., Ershov, D., Flasse, S., Fraser, R., Graetz, D., Maggi, M., Peduzzi, P., Pereira, J., Silva, J., Sousa, A., Stroppiana, D., 2004. A Global Inventory of Burned Areas at 1 Km Resolution for the Year 2000 Derived from Spot Vegetation Data. Climate Change 67, 345–377.

Thackway, R., Cresswell, I. D., 1995. An Interim Biogeographic Regionalisation for Australia: A Framework for Setting Priorities in the National Reserves System Cooperative Program. Webpage: http://www.deh.gov.au/parks/nrs/ibra/version4-0/framework/index.html, 04/04/2005.

U.S. Government, 1976. U.S. Standard Atmosphere. U.S. Government Printing Office, Washington, D.C.

Wamerdam, F., 2006. GDAL/OGR. URL: www.gdal.org, 01/11/2005.

Weisstein, E. W., 2006. "z-score". From MathWorld–A Wolfram Web Resource. URL: http://mathworld.wolfram.com/z-Score.html, 08/06/2006.

Wolfe, R. E., Nishihama, M., Fleig, A. J., Kuyper, J. A., Roy, D. P., Storey, J. C., Patt, F. S., 2002. Achieving sub-pixel geolocation accuracy in support of MODIS land science. Remote Sensing of Environment 83 (31 - 49).

Wooster, M., Zhukovb, B., Oertel, D., 2003. Fire radiative energy for quantitative study of biomass burning: derivation from the BIRD experimental satellite and comparison to MODIS fire products. Remote Sensing of Environment 83, 83–107.

Yamaguchi, U., Kahle, A. B., Tsu, H., Kawakami, T., Pniel, M., 1998. Overview of Advanded Spaceborne Thermal Emission and Reflection Radiometer (ASTER). IEEE Transactions on Geoscience and Remote Sensing 36, 1062– 1071.